DEVELOPMENT AND CHARACTERIZATION OF AN AEROELASTIC INSTABILITY ENERGY HARVESTER

by

Timothy James Bagatti

B.S. in Mechanical Engineering, University of Pittsburgh, 2008

Submitted to the Graduate Faculty of

the Swanson School of Engineering in partial fulfillment

of the requirements for the degree of

Master of Science

University of Pittsburgh

2010

UNIVERSITY OF PITTSBURGH

SWANSON SCHOOL OF ENGINEERING

This thesis was presented

by

Timothy James Bagatti

It was defended on

June 14, 2010

and approved by

Lisa Mauck Weiland, Ph. D., Assistant Professor of Mechanical Engineering Department

Daniel G. Cole, Ph. D, Assistant Professor of Mechanical Engineering Department

Mark Lee Kimber, Ph. D., Assistant Professor of Mechanical Engineering Department

Thesis Advisors: Lisa Mauck Weiland, Ph. D., Assistant Professor of Mechanical Engineering Department,

Daniel G. Cole, Ph. D, Assistant Professor of Mechanical Engineering Department

DEVELOPMENT AND CHARACTERIZATION OF AN AEROELASTIC INSTABILITY ENERGY HARVESTER

Timothy James Bagatti, M.S.

University of Pittsburgh, 2010

Development of new renewable energy sources has become paramount in the battle against rising energy consumption and prices, environmental destruction, and global climate change. However, prior research efforts have indicated an aeroelastic instability energy harvester (AIEH) is capable of generating more than 70 mW of power at ≈4 mph wind (below the cut-in speed of any wind turbine). The AIEH has shown an enhancement in performance in the presence of a bluff body (contrary to turbines) and a non-linear increase in power production with an increase in wind speed. It also allows the consumer to choose the extent of investment cost (less than $50 for parts), with minimal maintenance cost. The intent of this thesis work is to gain a better understanding of AIEHs in a number of different ways: characterizing the limit-cycle oscillation (LCO) experienced by an AIEH; validating the belief that an active ("smart") material may enhance the power density of an AIEH; validating and characterizing the enhanced performance exhibited by AIEHs in the presence of a bluff body. In the short term AIEHs are expected to be of particular utility for powering remote civil infrastructure sensor systems. In the long term they may have the potential to become a viable, new, renewable energy technology with power generation levels appropriate to societal energy needs. Also, its relatively low investment and maintenance cost has the potential to make this technology ideal for third world applications.

TABLE OF CONTENTS

LIST OF TABLES

LIST OF FIGURES

LIST OF ACRONYMS

CO carbon monoxide

CO_2 carbon dioxide

NO_x nitrogen oxides

CFC chlorofluorocarbon

EU European Union

AIEH aeroelastic instability energy harvester

LCO limit-cycle oscillation

FSI fluid-structure interaction

WPD wind power density

HAWT horizontal axis wind turbine

VAWT vertical axis wind turbine

EMI electromagnetic induction

LID linear induction device

RID rotary induction device

PVDF polyvinylidene fluoride

SLA stereolithography

FRF frequency response function

PSD power spectral density

FFT fast Fourier transform

LDV laser Doppler vibrometer

PVC polyvinyl chloride

ESI electrostatic induction

1.0 INTRODUCTION

Rising concerns for pressing environmental issues such as global warming, water shortages, and global population inflation have caused a push for the global community to rethink their energy production strategy. As quoted by renown Welsh scientist Sir John T. Houghton, "As a climate scientist who has worked on this issue for several decades, first as head of the Met Office, and then as co-chair of scientific assessment for the UN intergovernmental panel on climate change, the impacts of global warming are such that I have no hesitation in describing it as a *weapon of mass destruction*" [40]. It is no secret there is a correlation between gas emissions such as carbon dioxide (CO_2), carbon monoxide (CO), nitrogen oxides (NO_x), and chlorofluorocarbons (CFCs) and global warming [41]. Nor, that much of the global warming potential gases come mainly from fossil fuel energy generation. Power generation is the largest contributor of CO_2 emissions in the United States, accounting for close to 40% of the total CO_2 emissions globally each year [16]. Yet the burning of fossil fuels remains, and is projected to remain, the majority contibutor to our energy needs; coal is projected as the largest share of total generation through 2030, ranging from 44% to 47% in 2030 across four case studies, and the world energy consumption is only projected to double within 50 years[10]. Additionally, with a 0.5% annual increase in energy consumption projection [10] and being the world juggernaut of power consumption, 4.11 trillion kWh in 2008 [12], it is the U.S.'s responsibility to become the leader in production of new alternative energy sources.

1.1 PUSH TOWARD RENEWABLE ENERGY HARVESTING

An initial push toward renewable energy has been made, as seen in Figure 1. Moreover, President Obama, attempting to continue the trend, is calling for the initiative to generate at least 25% of the nation's electricity from renewable sources by 2025, and a near-term target of 10% by 2012 [16]. Not only does this assist in reducing the global climate change but it helps to reverse our country's current economic downturn. In 2008 the wind industry was responsible for the creation of 35,000 jobs [16]. Similar benefits of renewable energy generation speak for themselves: saving consumers and businesses money on energy bills, reducing vulnerability to energy price spikes, reducing peak demand and risk of power shortages, stimulating economic development, reducing water consumption necessary for power plant cooling purposes (nearly 50% of all water withdrawals in the U.S. [7]), reducing pollutant emissions, etc [24]. These benefits could help to reverse the current adverse economic effects of fossil fuel consumption. A 2009 Union of Concerned Scientists study estimates that under a 25% national renewable electricity standard, all other things being equal, average consumer elecricity prices would be 7.6% lower, with an average annual reduction of 4.3% through 2030 [16].

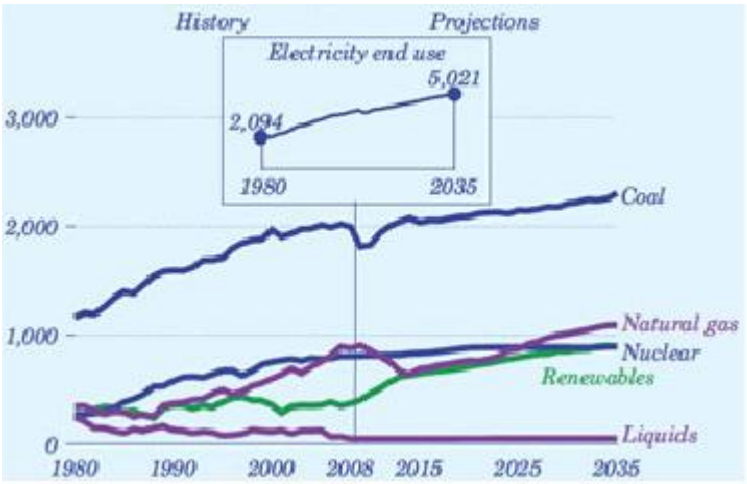

Figure 1: U.S. energy consumption, 2008; with projection to 2035 [11]

Not only is there a vast amount of wind energy waiting to be harvested (which will be shown in Figure 5 in chapter 2) but currently in many countries there are government incentives to invest in the wind energy infrastructure. In 2001, the European Union (EU) passed its Directive on the promotion of electricity produced from renewable energy sources in the international electricity market. This directive is a direct influence of EU's doubling of wind energy capacity from 2003 to 2007 and their 19% annual increase in wind installments [15]. Since the European Commission has changed its orginal 1996 target baseline five times and increased their targets for wind energy nearly tenfold, this trend in motivation is far from dissipating. Not only in Europe but, the U.S. has passed a provision to extend their production tax credit for wind energy and other renewable energy harvesting methods. Wind facilities that entered service before January 1, 2010, were eligible for a tax credit of 2 cents per kWh [10].

Being the fastest growing form of electricity generation in the EU, wind power has been adopted as their fossil fuel consumption savior; accounting for 43% of the global total wind generation in 2007. By the end of 2003 EU had installed 28,000 MW, which was doubled by 2007, avoiding 91 million ton of carbon dioxide emissions and supplying power equivalent to the needs of 30 million average European homes, which is expected to increase to 107 million average European households by 2020. The EU Heads of State have also set a binding target of 20% of its energy supply to come from wind and other renewable resources by 2020 [15]. They have taken notice and began to act on the large power capacity harnessable from onshore and offshore wind sources as well as the benefits gainable and the energy independence achievable from harvesting it. This is a trend that should be followed.

1.2 THESIS PROBLEM

The goal of this thesis is to develop, characterize, and analyze for proof of concept an aeroelastic instability energy harvester (AIEH), which is basically an airfoil/lifting surface that is induced into a stable limit-cycle oscillation (LCO) when exposed to fluid flow. AIEHs have shown to be a compact, modular, cost-effective wind energy harvesting technology

operable in a broader range of wind speeds and flow conditions than typical wind turbines and, unlike wind turbines, exhibit an enhancement in performance due to turbulent flow conditions created by bluff bodies/boundary layers inherent on and around buildings and other civil structures.

Previous research efforts, conducted by a senior design team in the Swanson School of Engineering at the University of Pittsburgh, have indicated that an AIEH is capable of generating ≈70 mW of power at ≈4 mph wind (below the cut-in speed of any wind turbine) due to excitation in the principle of a stable LCO in a fluid-structure interaction (FSI), and may exhibit an enhancement in performance due to irregularities in wind patterns, which develop naturally around civil structures. It has the potential to allow the consumer to choose the extent of investment cost (less than $50 for parts), with minimal maintenance cost, while being inherently insensitive to placement constraints due to its modular and compact nature.

This thesis offers characterization, as it relates to power generation, of some of the dynamics of an AIEH configuration. Proof of the AIEH's potential ability to harness "meaningful" power in flow speeds below that of any wind turbine are to be ascertained. It is hypothesized that an AIEH may exhibit an enhancement in performance due to irregular wind patterns; an investigation to provide proof of concept is conducted.

1.3 AIEH PROPOSED APPLICATIONS

In the short term AIEHs are expected to be of particular utility for powering remote civil infrastructure sensor systems. In the long term they may represent a viable, new, renewable energy technology with power generation levels appropriate to societal energy needs. Also, its relatively low investment and maintenance cost has the potential to make this technology ideal for third world applications.

2.0 WIND ENERGY HARVESTING

Though the use of wind energy can be seen earlier than 5,500 years ago for natural ventilation and boat propulsion, the first wind machine was found in Persia as early as 200 BC, belonging to Heron of Alexandria [35]. However, up until 1887, when the first known electricity generating windmill was installed by James Blyth in Scotland [52], wind machines were used solely to generate mechanical energy to grind grain and pump water. Electricity generation by windmills continued to grow until the predecessor of the modern wind-turbine took service at Yalta, USSR in 1931 [60].

2.1 WIND ENERGY RESOURCE OVERVIEW

Analysis has shown that onshore wind resources alone could supply approximately 6-7 times as much electricity as is currently consumed worldwide [49]. With the addition of offshore wind resources, this is a gargantuan amount of untapped energy. This is energy that can be harnessed without any of the additional costs of fuel associated with other forms of energy generation. This allows the total cost of producing wind energy throughout the 20 to 25 year lifetime of a wind turbine to be predicted with great accuracy [15]. However, currently on a global scale wind only accounts for approximately 1% of the total electricity generation [13].

The amount of energy available for harnessing is characterized as wind power density (WPD). WPD is determined at a particular location at either 10 m or 50 m above the ground and is measured in units of watts per square meter (W/m^2). Betz' law, which was developed by German physicist Albert Betz in 1919, relates the wind velocity (U) and density (ρ) to

the inlet area (A) being harvested by a wind turbine in order to calculate the maximum harvestable power:

$$P = \frac{16}{27}\frac{1}{2}\rho A U^3 \tag{2.1}$$

Notable from the above equation is that Betz proved only approximately 59% or $\frac{16}{27}$ of the total kinetic energy available in the wind can be converted into mechanical energy via a turbine, if one wanted to optimize power as opposed to work. This has become known as the Betz limit [49].

The assumptions for this derivation are as follows:

1. The rotor does not possess a hub, this is an ideal rotor, with an infinite number of blades that have no drag.
2. This is a 1-D control volume analysis, containing all flow into and out of the rotor so as to not violate the conservation equations.
3. The flow is considered incompressible and no heat is transfered from the rotor to the flow or vice versa.
4. The flow is only axial, not containing circulation (i.e. erratic/turbulent flow)

In order to derive this relation one must first understand a wind turbine rotor slows down the wind as it captures its kinetic energy and converts it into rotational energy. This means that the wind will be moving more slowly after the rotor than before the rotor. Since the amount of air entering through the swept rotor area must be the same as the amount of air leaving the rotor area, the air will have to occupy a larger cross section behind the rotor plane. Figure 2 illustrates this by showing an imaginary tube, or a so called stream tube, around the wind turbine rotor [49].

Now, let us make the assumption that the average wind velocity through the rotor area is the average of the undisturbed wind before the turbine, U_1, and after the passage through the rotor plane, U_2. The mass of the air streaming through the rotor per second is $m = \rho A(U_1 + U_2)/2$, where ρ is the density of air, A is the swept rotor area (as before), and $(U_1 + U_2)/2$ is the average wind velocity through the rotor area. The power extracted from the wind by the rotor is equal to the mass times the drop in the wind speed squared,

Figure 2: Betz law control volume; an imaginary stream tube, which shows how the slow moving wind behind a turbine must occupy a larger volume than the faster moving wind before the turbine [3]

according to Newton's second law:

$$P = \frac{1}{2}m(U_1^2 - U_2^2) \tag{2.2}$$

Substituting m from the first equation into this expression we get the following expression for the power extracted from the wind:

$$P = \frac{\rho A}{4}(U_1^2 - U_2^2)(U_1 + U_2) \tag{2.3}$$

Now, compare the result with the total power in the undisturbed wind streaming through exactly the same area, A, with no rotor blocking the wind. We call this power P_o:

$$P_o = \frac{\rho A}{2}U_1^3 \tag{2.4}$$

The ratio between the power extracted from the wind and the power in the undisturbed wind is then:

$$\frac{P}{P_o} = \frac{1}{2}\left(1 - (\frac{U_2}{U_1})^2\right)\left(1 + \frac{U_2}{U_1}\right) \tag{2.5}$$

We may plot P/P_o, which is known as the coefficient of performance, as a function of U_2/U_1:

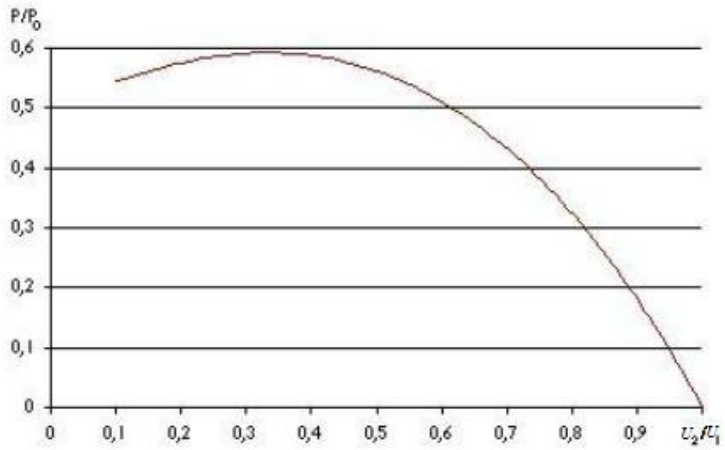

Figure 3: Power coefficient curve; relating the total power in fluid flow through a circular inlet area to the power harvestable by a turbine whose blades form the radius of the circular inlet area [3]

One can then see that the function reaches its maximum for $U_2/U_1 = 1/3$, and that the maximum value for the power extracted from the wind is 0.59 or 16/27 of the total power in the wind [49].

Another notable realization of Equation 2.1 is how the available power will increase by a factor of 8 for a doubling of the inlet wind velocity, due to the U^3 term. WPD however, is evaluated without the 16/27 factor in order to calculate the total amount of wind power passing through a given inlet area. WPD is used to categorize land areas for their resource potential by placing them into wind power classifications. The wind power classifications are broken into 7 classes ranging from Poor or Class 1 to Superb or Class 7, which can be seen below in Figure 4.

Maps are produced for a given area, breaking the area down by its wind power classification. An example, showing the United States, can be found below in Figure 5. As can be seen, the Midwestern region and especially the coasts are rich in wind energy resources, however, most of the US consists of wind energy below Class 3. Since most modern large scale wind farms are installed in areas with a classification of 4 or higher there is still a vast amount of energy not being harvested.

Classes of Wind Power Density at 10 m and 50 m[(a)]				
	10 m (33 ft)		50 m (164 ft)	
Wind Power Class	Wind Power Density (W/m^2)	Speed[(b)] m/s (mph)	Wind Power Density (W/m^2)	Speed[(b)] m/s (mph)
1	<100	<4.4 (9.8)	<200	<5.6 (12.5)
2	100 - 150	4.4 (9.8)/5.1 (11.5)	200 - 300	5.6 (12.5)/6.4 (14.3)
3	150 - 200	5.1 (11.5)/5.6 (12.5)	300 - 400	6.4 (14.3)/7.0 (15.7)
4	200 - 250	5.6 (12.5)/6.0 (13.4)	400 - 500	7.0 (15.7)/7.5 (16.8)
5	250 - 300	6.0 (13.4)/6.4 (14.3)	500 - 600	7.5 (16.8)/8.0 (17.9)
6	300 - 400	6.4 (14.3)/7.0 (15.7)	600 - 800	8.0 (17.9)/8.8 (19.7)
7	>400	>7.0 (15.7)	>800	>8.8 (19.7)

Figure 4: Wind power classification [16]

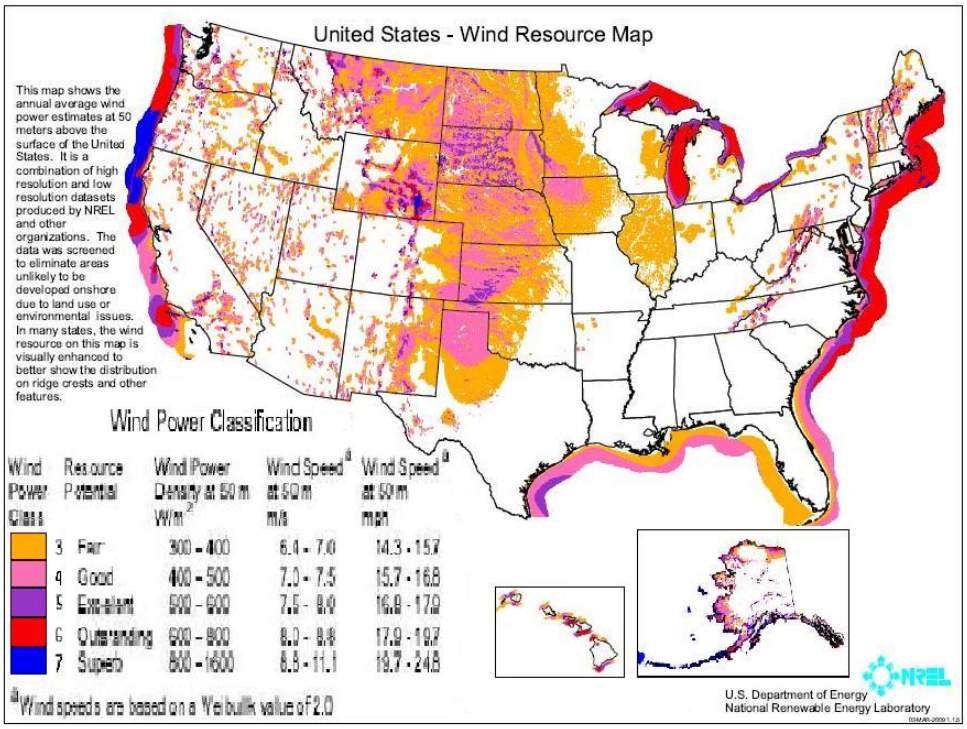

Figure 5: U.S. wind power classification and resource map [7]

2.2 MACRO & MICRO DEVICES

There are currently two primary configurations of harvesting wind energy, both on a macro- and micro-scale, horizontal axis wind turbines (HAWTs) and vertical axis wind turbines (VAWTs). However, the majority of the global capacity comes from macro-scale HAWTs; macro-scale or "utility-scale" being anything greater than 100 kW capacity. Figure 6 gives a visual representation of the two turbines.

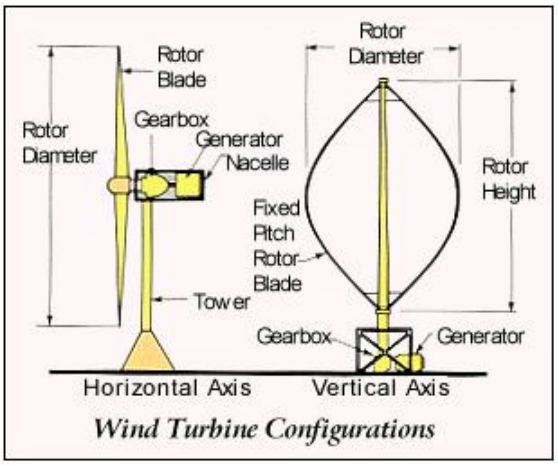

Figure 6: Wind turbines [16]

HAWTs are the most common form of wind generation. They typically consist of 3 turbine blades which use lift to cause the turbine to spin. Since this requires the turbines to be facing into the wind a yaw mechanism is required. On a micro-scale the blades are turned into the wind via a simple wind vane whereas on the macro-scale turbines generally use a wind sensor coupled with a servo motor. This requirement to adjust for varying wind causes a decrease in the turbine's power output. To avoid further output power leeching, most turbines are built with the blades placed upwind to the turbine support structure; turbulence or "mast-wake" is produced behind the support structure, which hinders the turbine's ability to easily produce lift and subsequently rotation and power production.

The main advantage of VAWTs to their horizontal counterparts is they are less sensitive to changes in wind direction because their blade orientation allows for the production of drag/lift from wind coming from any direction, nevertheless, axial flow is still preferred.

This advantage allows them to be installed closer to the ground which makes them cheaper to build and maintain [49], however, one should remember WPD increases with increased height off the ground. There are two types of VAWTs, Darrieus and Savonius. The Darrieus turbines, an example of which can be seen in Figure 7(a), utilize lift to produce rotation. They are high speed, low torque machines, which make them suitable for generating alternating current electricity. Yet, they are incapable of self starting and require some means, either manual or mechanical, to begin rotation. Savonius wind turbine, seen in Figure 7(b), use drag instead of lift to produce rotation, which allows it to be self-starting. On the other hand, they are slow high torque machines, which may be ideal for driving pumps but requires gearing to produce AC frequencies, thus increasing cost and reducing overall efficiency. All VAWTs share the same major disadvantage, they are inherently less efficient than HAWT because each blade of a VAWT must drag back against the wind for every half rotation about its vertical axis [49]. Even though one blade may be capturing the oncoming wind, at the same time the turbine's rotation is forcing another blade to fight back against the same oncoming wind until it rotates enough to become the capturing blade, where at that point the original capturing blade will now be the blade fighting back against the oncoming flow.

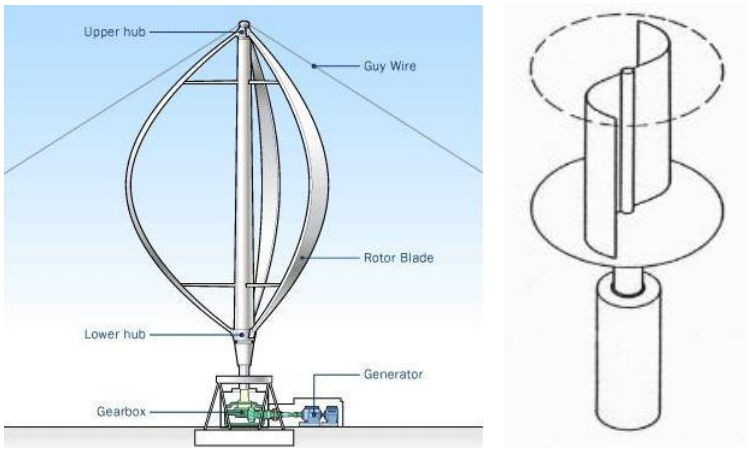

(a) Darrieus (b) Savonius

Figure 7: Vertical axis wind turbines [6, 14]

To counteract some of the disadvantages inherent in both types of VAWTs many of the designs today combine both types and often have helical versus straight shaped blades. A helical shape to the blades can help to minimize the pulsating torque associated with rotating straight blades which can cause the main bearing to fail [49], at the same time, helical blades are typically more complex and expensive to produce. Combining a Darrieus turbine with a Savonius turbine creates a turbine that is capable of self-starting that can reach higher rotation speeds than simply a Darrieus turbine. Still, even though all turbines have their own advantages and disadvantages that make them suitable for their particular environment, all turbines are susceptible to stresses that fatigue the turbine's parts simply due to the cyclic nature of a turbine.

2.2.1 MACRO DEVICES

As discussed prior, macro-devices mostly consist of HAWTs, with a power capacity larger than 100 kW. In order to have the best opportunity to harvest energy most of the turbines are placed on top of tall towers, typically 50 m to 100 m for land based installations. At those locations for every 10 m up the wind speed can increase by 20%, increasing the potential power output by 34%. The potential power output increase attainable with larger turbine blades, coupled with taller support structures, has been the driving reason wind turbines have been steadily increasing in size and power capacity for the past 30 years. Figure 8 shows the growth of HAWTs since 1980. A 50 kW machine, considered large in 1980, is now dwarfed by the 1.5 MW to 2.5 MW machines being installed today [7]. The growth of onshore turbines has seemed to plateau, however. Land transportation constraints and crane requirements for installation makes building larger land based turbines more costly and difficult to install [7]. On the contrary, offshore wind turbines are projected to continue to grow [15].

The wind speed at which turbine blades begin spinning is called a turbine's cut-in speed. Typically modern HAWTs have a cut-in speed of about 5 m/s but they do not reach their rated power until about 12 m/s to 14 m/s, which corresponds to Class 3 wind. At this point the pitch control system begins to limit power output and prevent generator and drive train

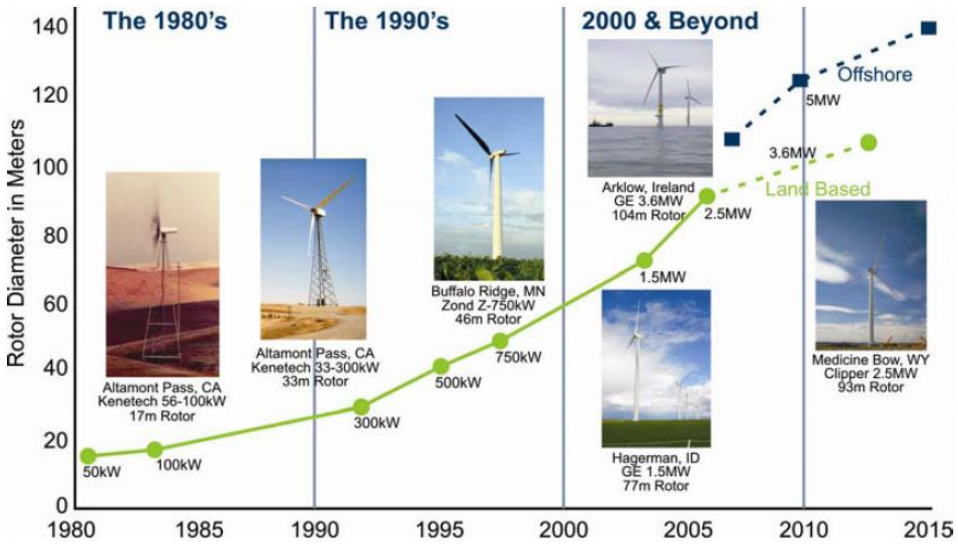

Figure 8: Development path & growth of HAWTs [7]

overload. At around 22 m/s to 25 m/s, the control system pitches the blades to stop rotation, feathering the blades to prevent overloads and damage the turbines components [49]. A plot of this trend can be viewed in Figure 9. As can be seen, the turbines do not produce much power until their rated speed is reached, especially particularly at their cut-in speed. The required wind classification to meet the rated speed coupled with the size and general public aesthetic disapproval keeps onshore wind farm installations to a typically rural environment.

2.2.2 MICRO DEVICES

In general micro-scale devices are much more diverse in design, variety, and application than macro-scale devices. Typically, all macro-scale turbines are HAWTs with three blades but the micro-scale turbines vary in blade numbers. HAWTs most commonly have between two to five blades, whereas VAWTs have at least two but possibly any number of blades, helical or straight in shape. The large variety of target locations require they have very specific characteristics which must meet the demands and expectations of the consumers, planners, and distribution network operators; mainly reliable operation, value for money, minimized

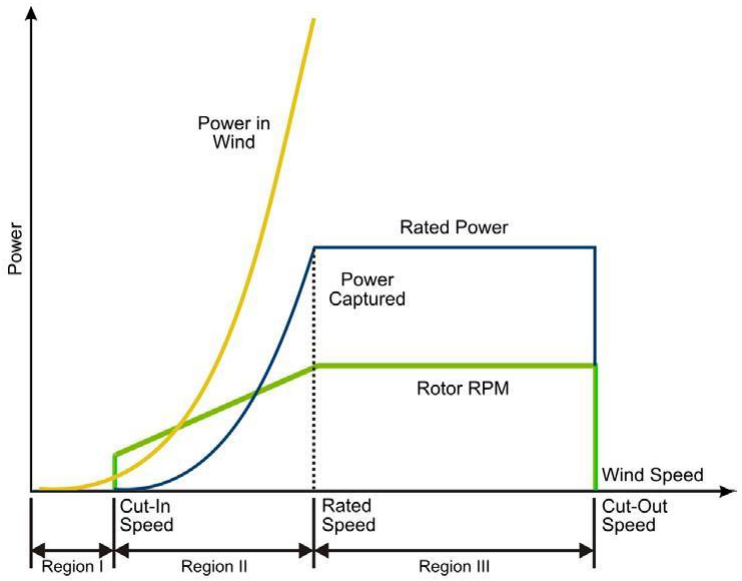

Figure 9: Turbine typical power output; versus wind speed [7]

visual intrusion, low noise levels, and compliance with all structural and electrical safety requirements [32]. Figure 10 provides a table of the top five most cost-effective micro-wind turbines chosen by CleanTechnica, an organization that prides themselves on educating their readers on clean renewable technology. Notable, and being similar to most micro-turbines, the typical cut-in speeds are around 8 mph or approximately 3.6 m/s, which is less than the 5 m/s seen with macro-turbines. Again though, at their cut-in speeds all turbines are not producing much energy; not until their rated capacity speeds have been met.

Similar to their macro-counter parts, small wind turbines work best in open locations, without turbulence caused by obstacles such as buildings, trees, hills, or a home. Perhaps their most abundant application consists of small roof-mounted turbines designed for large-scale deployment in rural, urban, and brownfield areas (brownfield being abandoned areas previously used for industrial or commercial facilities [32]). Siting becomes especially important for turbines in urban settings; wind patterns behave very differently around buildings and in densely-built areas so a turbine must be sited very precisely in order to gain access to axial wind of a sufficient velocity [16].

	Name	Rated Capacity	Cut-in Speed	Energy Production
	Southwest Windpower Skystream 3.7	1.9 kW continuous, 2.6 kW peak	8 mph	400 kW @ 12 mph
	Southwest Windpower Air X	400 W	8 mph	38 kW @ 12 mph
	AreoVironment Architectural Wind	N/A	N/A	N/A
	Southwest Windpower Whisper 500	3 kW	7.5 mph	1500 kWh @ 12.5 mph
	Bergey Excel	10 kW	7.5 mph	1500 kWh @ 12.5 mph

Figure 10: CleanTechnica top 5 roof-mounted micro-wind turbines [8]

Interestingly the cost per kilowatt hour of small turbines is inversely proportional to turbine size. Small-scale micro-scale turbine installation costs are always higher than macro-scale installations because the construction effort cannot be distributed over a large number of turbines [7]. With any wind turbine application only a finite amount of energy can be produced, therefore to become a more viable technology for the future, installation cost will have to fall.

2.2.3 NON-ROTARY DEVICE DEVELOPMENT

Recently, a non-turbine or non-rotary wind energy harvesting device has been developed, known as an aeroelastic instability energy harvester (AIEH). It uses the instability of aeroelastic flutter, which will be explained fully in the succeeding chapter. A classic example of

the aeroelastic phenomenon being the collapse of the Tacoma Narrows bridge in November 7, 1940. In the AIEH's case however, aeroelastic flutter, which is usually attempted to be suppressed due to its potentially destructive nature, is harnessed to induce a beam or belt made from mylar-coated taffeta into resonance. This motion is then used to drive an electric generator. In this case, magnets, which are attached to both ends of the fixed-fixed taffeta beam, travel in and out of wire solenoids due to the induced instability of the belt, producing electricity via the phenomenon of electromagnetic induction (EMI). Up until this development, wind power consisted strictly of rotary devices, which contain moving parts that have a higher potential to fatigue and fail.

The new device was developed by Shawn Frayne of Humdinger Wind Energy, LLC and is called the Windbelt. The company has developed three different variations, examples of which can be seen in Figure 11, of this device for varying application scales, micro, medium, and large:

1. **Micro:** Having a cut-in speed of 6 mph and stated to generate 100 Wh to 200 Wh over a 20 year life in 10 mph average wind speeds, this device has the potential to be used to power wireless sensors, opening up the industries of transportation, green buildings HVAC systems, urban air quality reporting, and infrastructure monitoring to truly wireless and battery-free information gathering [17].
2. **Medium:** This device, which is claimed capable of producing 3 W to 5 W, can be implemented according to the application. For instance, a single Medium Windbelt device is sized to power meshed WiFi repeaters, whereas a few units linked together can provide power to ocean navigation buoys or isolated lighting applications. The systems, like all of Humdinger's main products, are modular, in that individual units can be combined together as building blocks for larger installations [17].
3. **Large:** The device is a panel 1 m by 1 m in width and is comprised of 20 Medium Windbelts arranged in parallel. One panel is projected to generate 100 W and has numerous potential applications. As can be seen in Figure 11, these panels could be placed in series on roof tops to provide safety and energy concurrently. These panels could also be placed in series under bridges, walkways, or any overhanging structure.

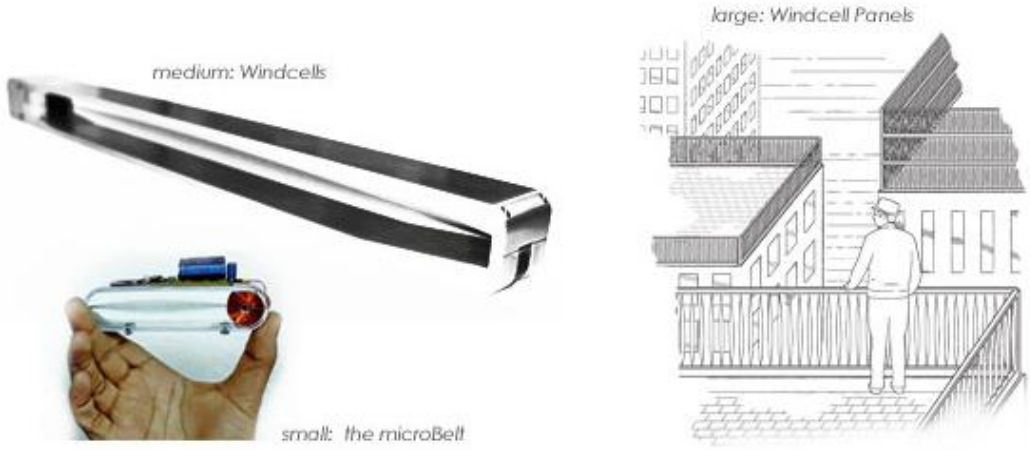

Figure 11: The Windbelt product family [17]

More recently, Bryant and Garcia [28] as well as Li and Lipson [48], all from Cornell University, have been developing their own variations of an AIEH. Brant's and Ephrahim's prototype uses multimode flutter as its means of excitation, similar to the Windbelt, however Li's and Lipson's prototype utilizes the forced excitation of an aeroelastic instability as its means of excitation. Multimode flutter and the forced excitation of an aeroelastic instability will be explained in depth in Chapter 3 and each of the Cornell prototypes are examined in Chapter 4.

3.0 MECHANICAL ENERGY HARVESTING VIA AEROELASTIC INSTABILITIES & FORCED EXCITATION

The Tacoma Narrows bridge collapse (Figure 12) is a testament to the energy converting destructive capabilities of fluid flow induced aeroelastic instabilities. The energy converting possibilities of these phenomena are not to go unnoticed. In each of the three phenomena, multimode aeroelastic flutter, galloping, and forced excitation, the energy present in the fluid flow is converted into mechanical energy. The energy conversion for the two aeroelastic instabilities, multimode flutter and galloping, is driven by a "self-excited" limit-cycle oscillation (LCO) of an aeroelastic system. The forced excitation of an aeroelastic instability is driven by a bluff body upstream in the flow which sheds vortices that in turn provide a periodic aerodynamic forcing on the device. With all three phenomena, the prospect of harvesting the induced mechanical energy for electrical energy, as with all power generation, will have a stabilizing (damping) effect on the system, potentially resulting in no power generation at all [33]. Therefore, an optimization effort to determine the best relation of power generation/system damping, which will allow for the most power to be harvested, is required. Having a small generator will allow the system to have high excitation while producing very little power. Whereas having a large generator may be capable of generating a large amount of power, however, it will have a large damping effect on the system, which in turn will greatly decrease the system's excitation, lowering the available energy to be harvested.

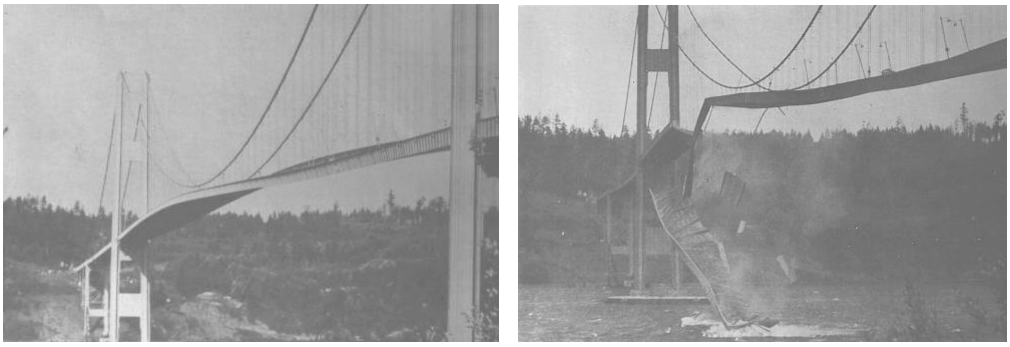

(a) induced aeroelastic flutter (b) structural failure

Figure 12: Tacoma Narrows bridge disaster [21, 22]; On November 7, 1940 the bridge was induced into aeroelastic flutter which eventually caused structural failure and collapse

3.1 AEROELASTIC INSTABILITIES

Aeroelastic instabilities of a structure in a fluid stream arise due to significant interaction among the three sides of the "aeroelasticity triangle"; inertial (dynamic), aerodynamic (fluid), and elastic (solid mechanics) forces [34]. This interaction causes a "self-excited" motion of the structure which can grow until a LCO is achieved without the assistance of an external driving force. In many cases this oscillation may grow until structural failure occurs. For this reason most research, particularly with flight vehicles, encompasses the prospect of damping this phenomena. However, a LCO is wished to be maintained for an aeroelastic instability energy harvester (AIEH), so as to harvest the most energy without structurally damaging the harvesting device. The dynamics of this system are non-linear, resulting from the non-linear relationship between coefficient of lift and angle of attack [33].

3.1.1 GALLOPING

The galloping discussed here, more specifically "across-wind galloping", is a large-amplitude oscillation (1–10 or more across-wind diameters of the body) of a slender structure, examples of which seen in Figure 13. The galloping of power transmission lines with accumulations

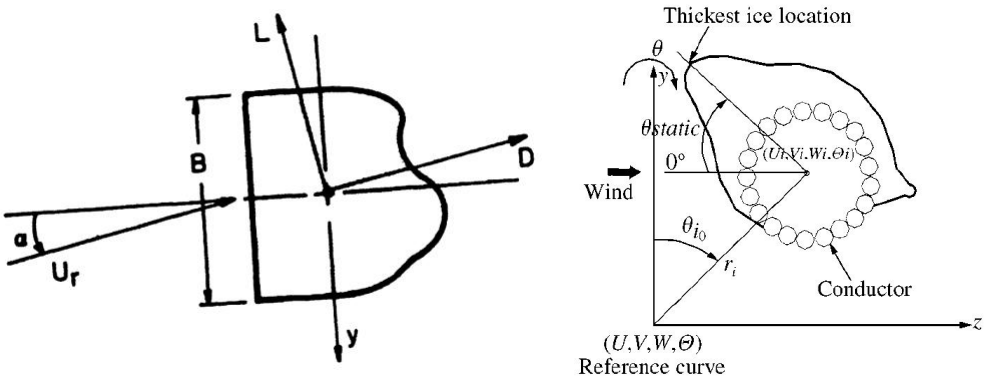

(a) bluff object (b) power transmission line

Figure 13: Galloping bluff body cross-sections [34, 61]; each of the cross-sections are asymmetric, contrarily circular cylinders cannot experience uniform flow across-wind galloping [34]

of ice and/or water is a prominent example of this phenomenon. "Wake galloping" is the other form of galloping, which refers to oscillations of a downstream cylinder induced by the wake flow of an upstream cylinder [34]. This, however, is a form of a forced excitation, called vortex induced vibration, and though a similar phenomenon will be discussed further later, this specific example will not be further discussed. For brevity across-wind galloping will simply be referred to as galloping.

For this discussion, only the oscillation of a device experiencing galloping in a single-mode vibration, as seen in Figure 14, will be considered. The aerodynamic interaction with the device occurs through the lift, $L(\alpha) = qSC_L(\alpha)$, where $q = \frac{1}{2}\rho U^2$ (U is flow velocity) is the dynamic pressure, S is the planform area, and C_L is the coefficient of lift [33].

The coefficient of lift may be a non-linear function of the angle of attack, $\alpha = \dot{y}/U$. The structural transfer function relating force f and velocity $\dot{y}$ is as in equation 3.1, where m is the mass, c_m is the structural damping, and k is the stiffness inherent to the structure [33].

$$\frac{\dot{y}}{f} = G(s) = \frac{s}{ms^2 + c_m s + k} \tag{3.1}$$

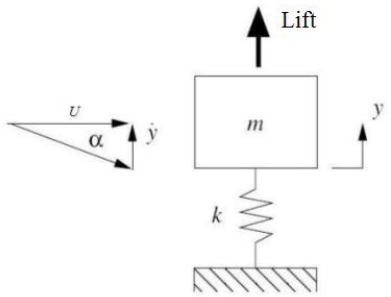

Figure 14: Square prism spring-mass system schematic; used for a micro AIEH [33]

The force f is the cumulative resultant force of the induced lift due to airflow across the device (f_a) and the resulting damping force due to energy conversion (f_e), which opposes the motion: $f = f_a - f_e = qSC_L(\alpha) - c\dot{y}$ [33].

Figure 15 shows the feedback interaction of the structure and the external forces. The non-linear effects of lift make analyzing the motion of the device difficult. Typically numerical simulations, such as the technique of describing functions (also called harmonic balance), is required to determine the characteristics of the oscillation [33]. For a more in-depth explanation see [33].

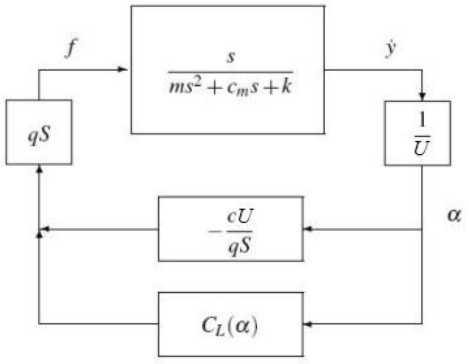

Figure 15: Galloping feedback loop; relationship of aerodynamic and electrical generation forces with the structural response [33]

3.1.2 MULTIMODE FLUTTER

Similar to galloping, multimode flutter is a self-excited oscillation capable of growing into a stable LCO. Galloping however is described as a single-mode oscillation, whereas the dynamics of multimode flutter can most simply be described by a two-mode typical section airfoil model with plunge and twist modes; plunge being motion in the y direction and twist in the θ, as in Figure 16. Though, the mechanics of any device or lifting surface experiencing flutter will inherently include multiple plunge and twisting modes [33]. Flutter is possible due to interaction among the sides of the aeroelastic triangle, seen in Figure 17. The onset of flutter, or cut-in, occurs when the plunge and twist modal frequencies coalesce [39]. If the energy induced due to the interaction between the plunge and twist modes of vibration is greater than the natural damping of the system the vibration will grow resulting in a feedback loop and the particular phasing between the two modes can result in a stable LCO. With increasing flow velocity there is an increase in the possible energy able to be introduced to the system, therefore, the flutter cut-in speed occurs at the flow velocity where the energy induced into the system is greater than the system's natural damping. The characteristics of the oscillatory instability depend upon the mass distribution of the lifting surface, its aerodynamic characteristics, structural stiffness and damping, and the speed of the fluid [33].

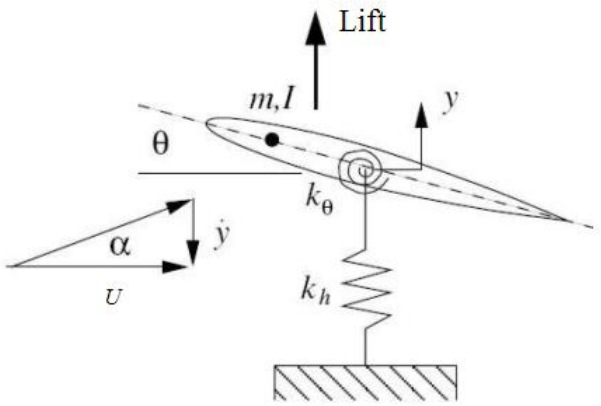

Figure 16: Typical section airfoil schematic[33]

Figure 17: Aeroelastic Triangle; significant interaction among the triangle's forces results in multimode flutter

The twisting motion of the lifting surface results in a lifting force due to the change in the angle of attack (α), and this force results in deflection (plunge). These two effects are further coupled because the motion of the lifting surface across the flow results in an induced angle of attack. Therefore, with a change in the angle of attack the system's deflection will grow due to lift, however, it does not grow without bound since the lift falls off at high angles of attack; the lifting surface stalls. This motion may reach a steady LCO [33].

When an object is statically stable below its flutter speed or boundary (flow speed at which flutter is induced) is disturbed the oscillatory motion caused by that disturbance will die out in time with exponentially decreasing amplitudes. In other words, the air is providing damping and the plunge and twist modes of flutter are not capable of coupling. Above the flutter speed however, the air can be said to provide negative damping, allowing the oscillations to grow with exponentially increasing amplitudes [39]. Depictions can be seen in Figure 18. When idealized for linear analysis, the nature of flutter is such that the flow over the lifting surface not only creates steady components of plunge and twisting

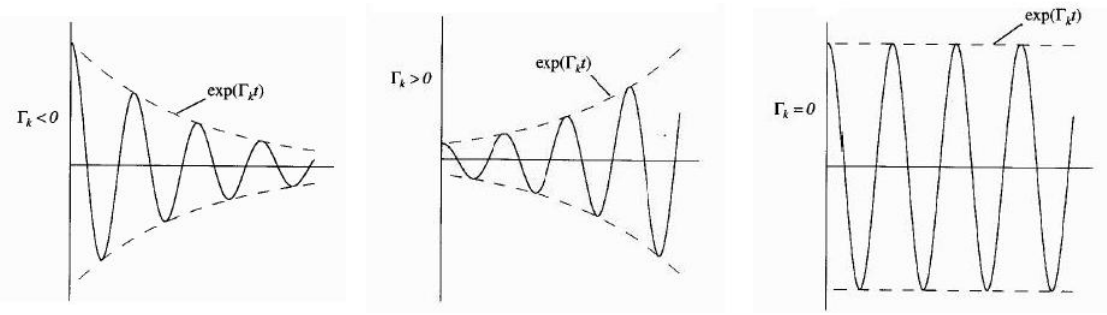

(a) below flutter speed (b) above flutter speed (c) stable limit cycle

Figure 18: Typical mode amplitude behavior; Γ_k is called the modal damping of the k_{th} mode [39]

moment but also creates dynamic forces in response to small perturbations of the lifting surface motion [39].

Since the motion of the lifting surface is influenced by the lift and the lift is in return influenced by the motion of the lifting surface, creating the feedback loop, the aeroelastic equations are derived in two parts: the structural equations (Equation 3.2) [33], which describe the plunge and twist motions under the influence of the lift and the aerodynamic equation (Equation 3.3) [33], describing the lift as function of twist and plunge velocity.

$$\begin{bmatrix} m & mx_{cg} \\ mx_{cg} & I_e \end{bmatrix} \begin{bmatrix} \ddot{y} \\ \ddot{\theta} \end{bmatrix} + \begin{bmatrix} c_y & 0 \\ 0 & c_\theta \end{bmatrix} \begin{bmatrix} \dot{y} \\ \dot{\theta} \end{bmatrix} + \begin{bmatrix} k_y & 0 \\ 0 & k_\theta \end{bmatrix} \begin{bmatrix} y \\ \theta \end{bmatrix} = \begin{bmatrix} qS \\ qSx_{cp} \end{bmatrix} C_L + \begin{bmatrix} -1 \\ 0 \end{bmatrix} f_e \quad (3.2)$$

$$C_L(\alpha) = C_{L\alpha}(\theta - \frac{\dot{y}}{U}) = qSC_{L\alpha} \left(\begin{bmatrix} -1/U & 0 \end{bmatrix} \begin{bmatrix} \dot{y} \\ \dot{\theta} \end{bmatrix} + \begin{bmatrix} 0 & 1 \end{bmatrix} \begin{bmatrix} y \\ \theta \end{bmatrix} \right) \quad (3.3)$$

In Equation 3.2 I_e is the polar moment of inertia about the elastic axis of the airfoil, $C_{L\alpha} = \partial C_L / \partial \alpha$ is the stability derivative, and x_{cg} and x_{cp} locate the center of gravity and center

of pressure, respectively, with respect to the elastic axis and are positive toward the leading edge of the airfoil. The plunge and twist stiffnesses and damper coefficients are k_h and k_θ and c_h and c_θ, respectively. The coefficient of lift is a function of the angle of attack, which depends upon the twist and the plunge velocity; $\alpha = \theta - (\dot{y}/U)$, thus becoming a linear function of the state of motion of the airfoil for small deflections about equilibrium. In Equation 3.3 it should be remember that q is the dynamic pressure and S is the planform area, as well as pointed out that the first term acts as an aeroelastic damper while the second term acts as a negative spring. The difficulty with analyzing flutter instabilities is that the state equation depends non-linearly upon the free stream velocity, U; in particular the lift which is a function of the state.

3.2 FORCED EXCITATION

As briefly introduced, a forced excitation of a body can occur in the wake of an upstream bluff body. As discussed above, with wake galloping a single-mode oscillation of a lifting surface is excited in the wake of an upstream circular cylinder. In our case however, the forced excitation of an aeroelastic instability (multi-mode) is induced in a lifting surface due to the wake of an upstream circular cylinder. As with all bluff bodies, alternating periodic vortices with opposite rotational directions are shed off the trailing edge of the bluff body and travel along with the mean flow, thus providing periodically changing flow components perpendicular to the mean flow direction [54]. This periodic vortex shedding forms what is known as a von Kármán vortex street (Figure 19), which is a hydrodynamic instability that arises at relatively low Reynolds numbers (between 47–10,000 for cylindrical cross sections [54]) and can be more thoroughly explained with the Helmholtz theorem: The total vorticity will always vanish within any closed curve surrounding a particular set of fluid particles. Thus, if some clockwise vorticity develops about the airfoil, a counterclockwise vortex of the same strength has to be shed into the flow. As they move along downstream the shed vortices change the flow field by inducing an unsteady flow back onto the airfoil. This behavior is a function of the strength of the shed vortices and their distance away from the airfoil [39].

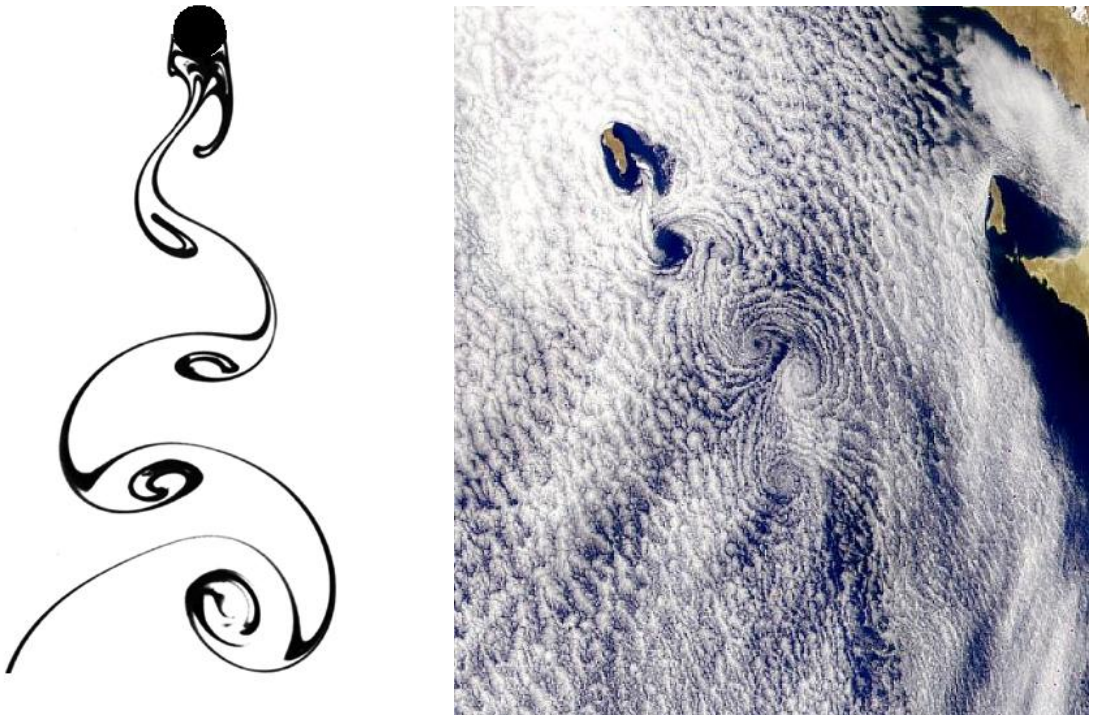

(a) due to a circular cylinder [4]

(b) due to an island [5]

Figure 19: Von Kármán vortex street

Fung(1995) suggested a simple experiment to demonstrate this phenomenon: Attempt to rapidly move a stick in a straight line through water and notice the results. In the wake of the stick there is a vortex pattern, with vortices being shed alternately from each side of the stick. This shedding of vortices induces a periodic force perpendicular to the stick's line of motion, causing the stick to tend to wobble back and forth in your hand. A similar phenomenon happens with the motion of a lifting surface through a fluid and must be accounted for in unsteady aerodynamic theories [39]. As it pertains to this thesis however, the upstream vortex inducing bluff body (circular cylinder) remains stationary, whereas the downstream airfoil is excited via the periodically alternating vortices.

For long rigid cylindrical bodies in uniform flow, the frequency at which vortices are shed satisfies the relation,

$$\mathrm{St} = \frac{F_s D}{U} \tag{3.4}$$

where D is the across-flow dimension of the cylinder, U is the mean speed of the oncoming flow, F_s is the vortex shedding frequency, and St is called the Strouhal number, named after Czech physicist Vincent Strouhal who studied vortex shedding and the associated forces in 1878. For smooth circular cylinders St changes drastically at certain critical Reynolds numbers. However, with rough circular cylinders no such critical phenomena appears to have been observed [34]. Recalling that the Reynolds number is a non-dimensional number that relates the inertial forces ($\rho U^2 \delta^2$) to the viscous forces ($\mu U \delta$) in fluid flow, where ρ is the fluid density, δ is the characteristic linear dimension (for example hydraulic diameter) of the flow, and μ is the dynamic viscosity of the fluid. So the Reynolds number is given as:

$$\mathrm{Re} = \frac{\rho U \delta}{\mu} \tag{3.5}$$

It can also be expressed in terms of the kinematic viscosity (υ) as:

$$\mathrm{Re} = \frac{U \delta}{\upsilon} \tag{3.6}$$

In terms of the Reynolds number (for $40 \leq \mathrm{Re} \leq 200,000$), the Strouhal number (for circular cylinders) becomes [36]:

$$\mathrm{St} = 0.2684 - \frac{1.0356}{\sqrt{\mathrm{Re}}} \simeq 0.2684 \tag{3.7}$$

Understanding these relations leads to the possibility of, when knowing the flow velocity, matching the vortex shedding frequency of a bluff body, whose across-flow dimension can be controlled, to the LCO frequency of the lifting surface. The amplitude of the response may increase and, in situations where the excitation is sufficient, may drive the system to a basin of attraction for a larger LCO (if such exists). In this case the response will include harmonics at the LCO frequencies and its multiples. With proper design, this may be a strategy to ensure that, in cases where there are multiple LCOs at a particular operating point, a harvesting device's response and power generation may be maximized [33].

An analysis of the sinusoidal excitation of the energy harvesting device is complicated by the fact that the energy harvester is operating in a LCO. A natural place to start for such an analysis is with the dynamics of the system linearized about the LCO, but those dynamics are time periodic, characterized by the fundamental frequency of the LCO [33].

3.3 ENERGY CONVERSION

The goal of the device development is to use the energy converting capabilities of these phenomena; however, inherent in power generation is a stabilizing or damping effect to the instabilities that could result in no power generation at all. An understanding of the relationships between these instabilities and the means of electrical energy conversion is therefore essential to the optimization of any harvesting device. In this case the conversion of mechanical energy to electrical energy is made utilizing electromagnetic induction (EMI) generators where the transformation of force/velocity, f and $\dot{x}$, to voltage/current, V and i, can be described via $f = \kappa i$ and $V = \kappa \dot{x}$. κ is the torque and back emf constant. EMI will be more fully explained in the proceeding chapter. The electrical energy storage or distribution can most simply be modeled as a resistive load; $V = Ri$. When combined with the above EMI generator equations the force/velocity relationship on the mechanical side is $f_e = (\theta^2/R)\dot{x}$, which is a damper with a coefficient of c [33].

The average power dissipated by this damper is equal to the average power generated per cycle of the lifting surface's oscillation, assuming the oscillation is of a sinusoidal motion at a frequency, ω, $x(t) = X \sin \omega t$:

$$P_{gen} = \frac{1}{2} c \omega^2 X^2 \tag{3.8}$$

The non-dimensional coefficient of performance (C_P) is:

$$C_P = \frac{P_{gen}}{qSU} = \frac{\frac{1}{2} c \omega^2 X^2}{qSU} \tag{3.9}$$

From this it appears that the equivalent damper should be made as large as possible, however it should be realized that the amplitude of vibration, X, depends upon the damper's coefficient and the frequency of excitation [33]. Therefore, the larger the damper the smaller the excitation and an optimization is required.

4.0 MECHANICAL TO ELECTRICAL ENERGY CONVERSION

In order to take advantage of the mechanical energy induced via the aeroelastic instabilities, it must be converted into electrical energy. There are a number of methods to accomplish this energy conversion. The most often seen method of energy conversion in macro-scale power plants are electromagnetic induction (EMI) generators. These generators are typically used in juncture with turbines that are spun by fluid movement, whether that fluid is wind, water, or steam. In addition, the development of electroactive materials has spawned a new wave of electric generation ideas and possibilities.

4.1 ELECTROMAGNETIC INDUCTION

Courtesy of English physicist Michael Faraday, who discovered the phenomenon of electromagnetic induction in the autumn of 1831, the creation of the first dynamo, an electric generator, by Hippolyte Pixii in 1832 became a reality [50].

Faraday's law of induction relates the magnitude of the electromotive force (ε) with the change in magnetic flux (Φ_B) in the circuit with respect to time and can be seen directly below in equation 4.1, as related to a solenoid with N number of turns.

$$|\varepsilon| = N \left| \frac{\partial \Phi_B}{\partial t} \right| \tag{4.1}$$

Therefore, electrical energy may be produced by either moving a wire coil (solenoid) relative to a stationary constant magnetic field or vice versa. In the aforementioned configuration, in which the mechanical parts move relative to each other due to an outside energy source, the device is considered a generator because it is capable of taking the mechanical energy

introduced by the system and converting it to electrical energy. This process can be performed in reverse by applying a current to the solenoid which induces a movement between the solenoid and the source of the constant magnetic field. In this configuration the device would be considered a motor. EMI generators and motors can be broken down into two basic categories, linear induction devices (LIDs) and rotary induction devices (RIDs).

4.1.1 ROTARY INDUCTION DEVICES

Application of RIDs is commonplace in modern technology. Applications include but are not limited to: an alternator that charges a car battery, a ceiling fan that cools a room, a blender in a kitchen, a power drill, etc.. Though the applications of RIDs are numerous, among the most important and exploited applications is power generation. Nearly all known forms of power production utilize EMI as the final step in converting some form of fuel into electricity; whether nuclear, hydro, coal, natural gas, geothermal, or wind. The only potentially significant source of power production not utilizing RIDs is solar energy. A diagram of a typical simple fossil fuel burning power plant can be seen in Figure 20.

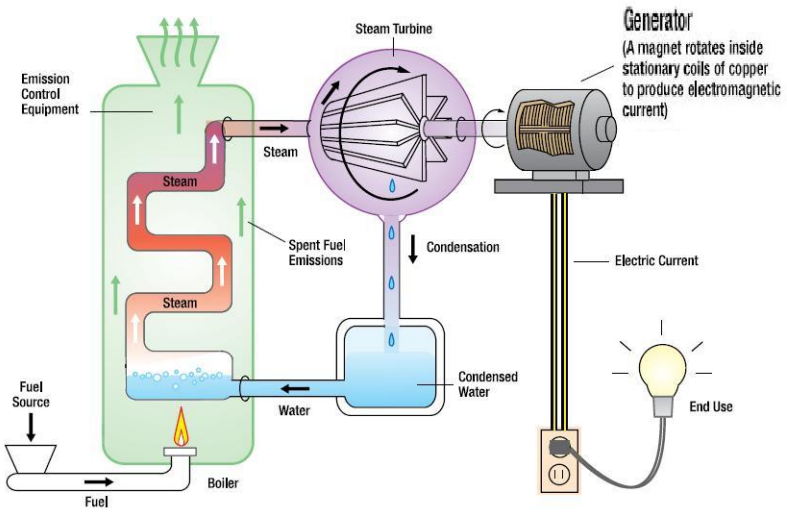

Figure 20: Simple fossil fuel power plant [45]

The basic mechanical parts of a RID are the rotor and the stator. Figure 21 shows a diagram of a basic EMI rotary generator/motor. The rotor rotates inside the stator which surrounds the rotor and remains stationary. The power production elements, the armature and the field, are separated and can each be located on either the rotor or the stator. The field, or magnetic field, can be produced by either a permanent magnet or an electromagnet, which is basically a solenoid driven by a current which produces a magnetic field. The armature is fundamentally the opposite of an electromagnet; as the armature moves relative to the field the magnetic flux through the armature is changing so a current is induced in the armature. The armature, field, and their motions relative to each other are positioned to follow John Ambrose Fleming's right hand rule.

In Figure 21 the basic rotary generator exhibited is designed so the armature spins on the rotor inside the stator, which produces the magnetic field via a permanent magnet. Again, this can be switched to have the magnetic field spinning on the rotor inside the stator, which would then have to contain the armature. Another RID is seen in Figure 22.

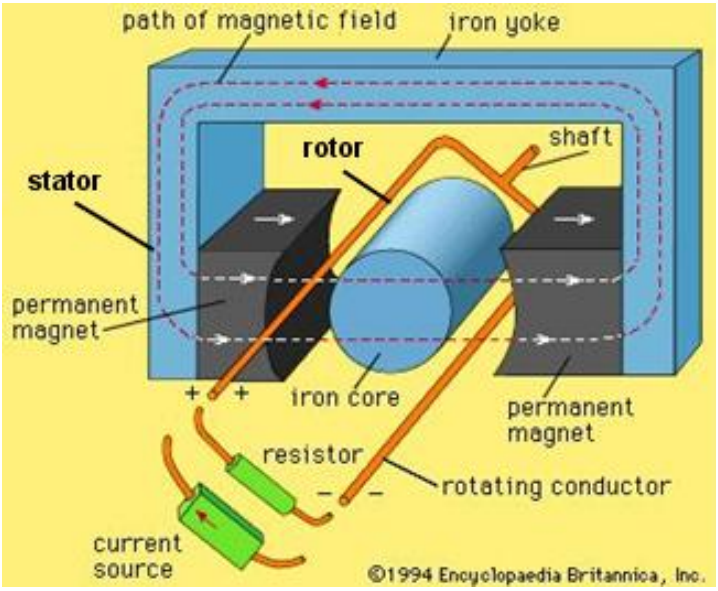

Figure 21: Basic EMI rotary generator/motor [43]; the armature is located on the rotor and the stator produces the field via a permanent magnet

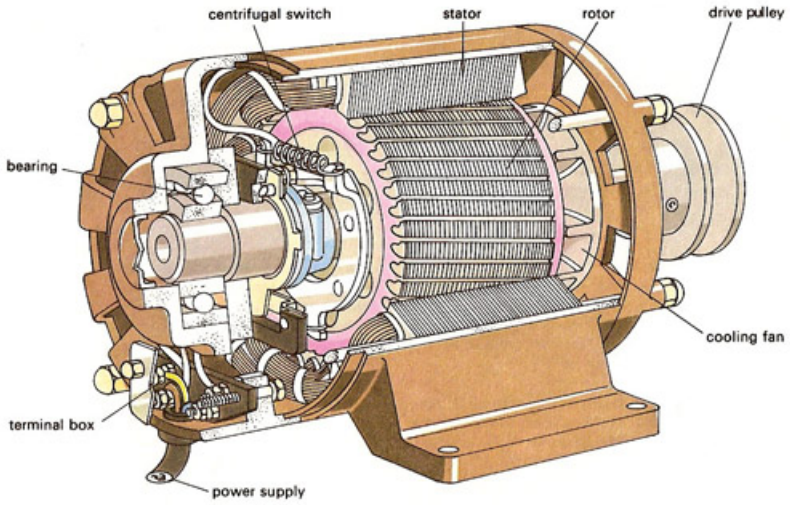

Figure 22: Rotary electric motor [19]; the field is produced via an electromagnet

4.1.2 LINEAR INDUCTION DEVICES

LIDs are composed of the same basic components as RIDs, however they are constructed as if the stator is cut and rolled flat to allow for the production of a linear force about its length instead of rotating the rotor and producing a torque. Therefore in a LID the rotor is replaced by a translator [59]. A depiction of this configuration can be seen in Figure 23.

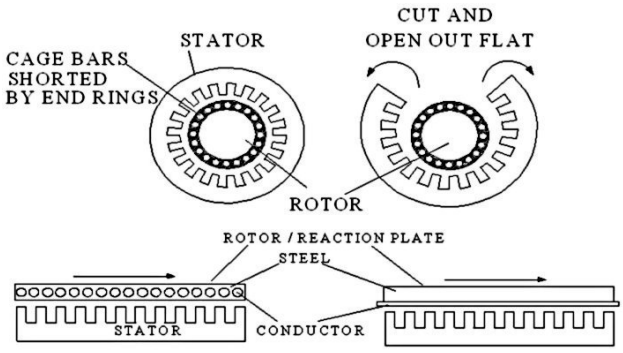

Figure 23: Link between RIDs and LIDs [20]

Similar to RIDs, LIDs have numerous applications. As a motor, perhaps the most known application would be in Maglev trains since the 1970s and also more recently in roller coasters [26]. They have also been proposed for use in rope-less elevators and aircraft carrier aircraft catapults. In recent times, as a generator, the Faraday Flashlight has become a popular substitution for the tradition battery powered flashlight. With the Faraday Flashlight, one simply needs to shake the flashlight in an axis along its length for a few seconds in order to have the linear induction generator inside the flashlight charge a capacitor that provides the power to produce light. Seen in Figure 24, Oregon State University proposes the use of linear EMI generators to harvest the power of ocean waves. Also, a linear EMI generator designed to harness the movement of a human body has already been presented and an optimization effort taken [59].

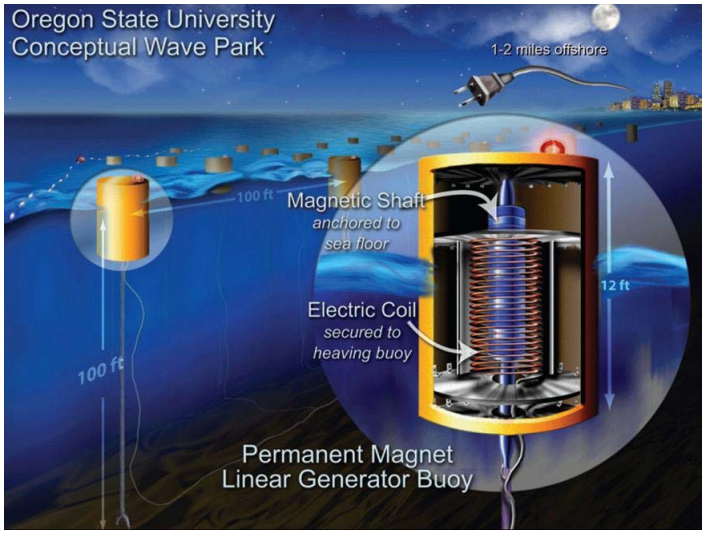

Figure 24: Oregon State University proposed ocean wave energy harvesting park [18]

4.2 PIEZOELECTRIC POSSIBILITIES & CURRENT IDEAS

Piezoelectric materials produce an electric current or electric potential when deformed or stressed. Thus, the piezoelectric material could be considered a generator because it produces

electrical energy when deformed by a mechanical energy input. The material is also capable of working as a motor, producing a deformation, or mechanical stress, with an electrical energy input [31]. Figure 25 gives depictions of a piezoelectric material in motor and generator configurations. In both representations the material is stressed along one axis. While not illustrated, piezoelectric materials also work in other deformation modes (i.e. bending).

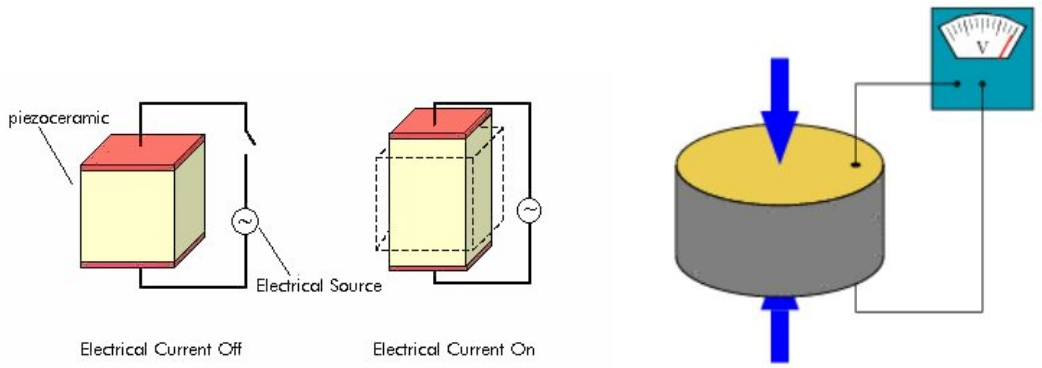

(a) piezoelectric motor (b) piezoelectric generator

Figure 25: Piezoelectric effect [1, 2]

Use of piezoelectric materials is common place in modern society. For instance any lighter in which one simply needs to press the button takes advantage of the piezoelectric effect. The pressing of the button causes a stress in a piezoelectric crystal producing a voltage difference and allowing a spark to light the flame. Also, many modern ink jet printers utilize piezoelectric crystals and polymers in the production of ink cartridges. The fast response time and deformation control of the piezoelectric materials allow for precise ejection of ink and production of higher resolution images [27].

In recent years piezoelectric materials have been viewed as potential electric generators for numerous applications. In most of these applications the mechanical energy harvested is of a cyclic nature. Typically the piezoelectric material is attached to a structure that is either vibrating or periodically stressed as in *in vivo* applications, [31, 56], or provides the base structure to shed vortices in order for a flag of the piezoelectric material to harvest the energy available in the von Kármán vortex street. Examples of these applications are given

below with an explanation of the reasoning why the need for mechanical periodic stressing of the material associated with these applications is paramount.

4.2.1 VIBRATION MATCHING SCAVENGING DEVICES

When the mechanical stress applied to a piezoelectric generator is static, the electrical energy produced is a small percentage of the total mechanical work done on the system by the source. Most of the remaining work is stored in the form of strain energy in the elastic piezoelectric element, and is therefore available for future extraction. By oscillating the material dynamically, one can make use of the stored potential energy to increase the conversion efficiency [31]. It is easy then to understand how vibrating and oscillating structures provide sources for piezoelectric energy harvesting.

There are several different proposed configurations to harvest energy from vibrating sources; the differences mostly pertaining to shape and geometric configurations of the piezoelectric generator. Four distinctly different configurations of vibration harvesters are given below in Figure 26. Please note that these and nearly all piezoelectric vibrational harvesters are designed for micro-scale applications.

Presented in [42], and depicted in Figure 26(a), a corrugation-shaped fixed-fixed bimorph beam made of the piezoelectric polymer polyvinylidene fluoride (PVDF) is examined as a resonant frequency vibrational energy harvester. The goal for all vibration matching piezoelectric generators is to be capable of matching its natural frequency to the range of frequencies experienced by its support structure. Typically for most mechanical and electrical systems resonant excitation is avoided since the large amplitude of excitation associated tends to be disastrous (e.g. Tacoma Narrows Bridge disaster). Though wear and potential failure associated with resonance is an important aspect of the design and construction of a piezoelectric vibrational harvester, the large amplitude and frequency of excitation associated with resonance allows for a dramatic increase in power production. Thus, resonance is desirable for piezoelectric energy harvesters.

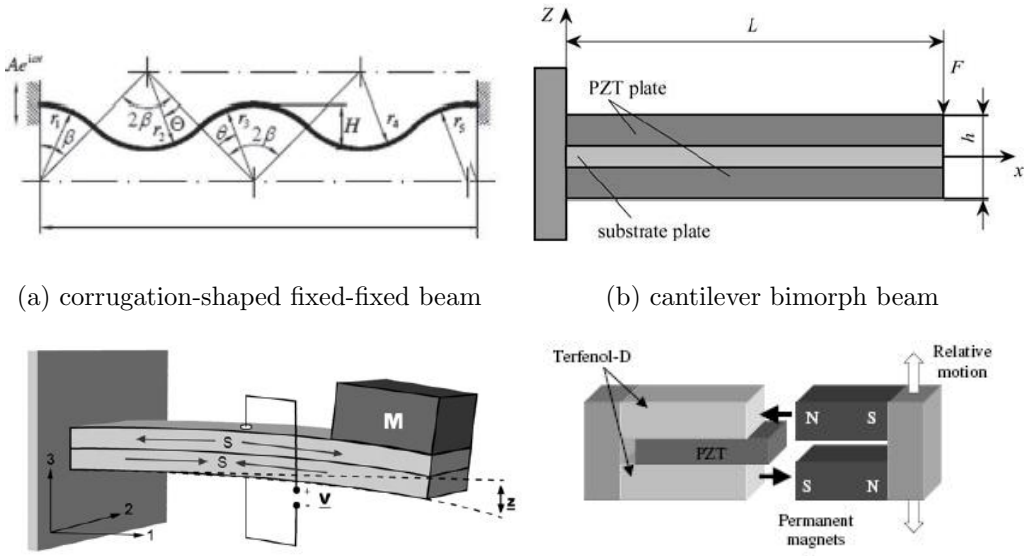

(a) corrugation-shaped fixed-fixed beam

(b) cantilever bimorph beam

(c) mass loaded cantilever bimorph beam

(d) linear magnetostrictive-piezoelectric generator

Figure 26: Piezoelectric vibration energy harvesters [42, 47, 55, 25]

The formula for natural frequency can be seen in Equation 4.2; ω_n being the natural frequency, m the mass of the vibrating structure, and k the spring constant associated with that structure.

$$\omega_n = \sqrt{\frac{k}{m}} \tag{4.2}$$

Some methods for adjusting the natural frequency of the vibration matching piezoelectric generators can be expressed with the examples given in Figure 26. The natural frequency of the generator in Figure 26(a) can be increased by increasing the number of arcs per length and decreased by increasing the span length [42]. In Figure 26(b) altering the thickness ratio, altering the spring constant, of the bimorph can adjust its natural frequency [47]. The bimorph in Figure 26(c) can alter natural frequency by altering the mass, which alters the natural frequency [55, 46]. Typically the natural frequency is altered by altering the material dynamics or device geometry and physical characteristics, yet some piezoelectric vibrational generators actively alter their natural frequency by making use of EMI [25, 29].

4.2.2 TRANSVERSE PRESSURE & AEROELASTIC FLUTTER HARVESTING DEVICES

Piezoelectric generators which use multimode flutter or forced excitation of an aeroelastic instability as their source of mechanical energy are being developed. In particular, multiple researchers at Cornell University are currently experimenting with and developing two different piezoelectric generators; one which utilizes the creation and presence of transverse pressures, as in the von Kármán vortex street, and one that makes use of aeroelastic flutter as the mechanical energy source to be harvested.

Similar to the Windbelt the Cornell prototype developed by Bryant and Garcia, is excited via aeroelastic multimode flutter. As seen in Figure 27, in this case the belt on the Windbelt is replaced with a metallic airfoil and the airfoil is then dynamically allowed to move only in a structured plunge and twist motion. Though these are the two motions comprising multimode flutter it does not allow for erratic behavior sometimes noticed with flutter. Instead of utilizing EMI as the means of converting the mechanical energy present as the airfoil moves through its plunge and twist motions, it utilizes two platforms of piezoelectric patches, one for the twist motion and one for the plunge motion [28].

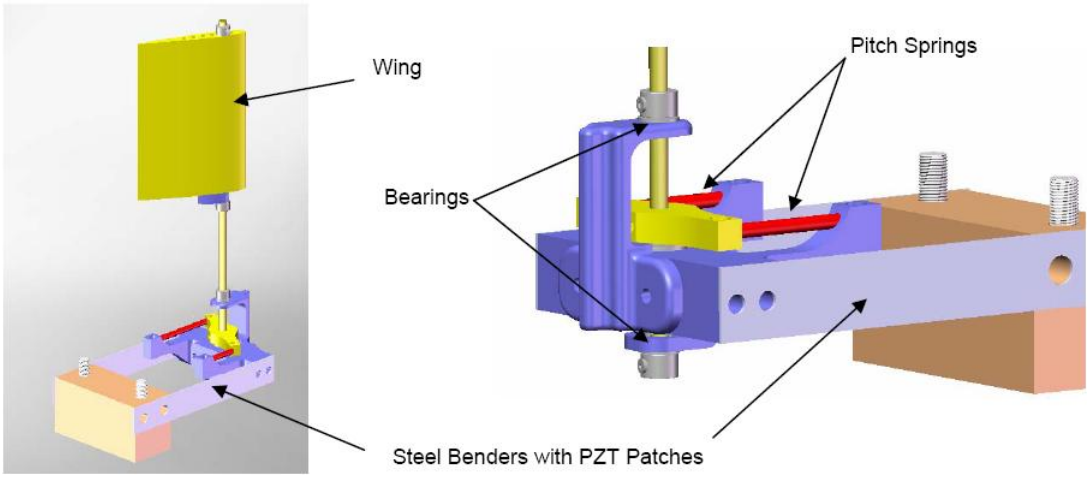

Figure 27: Bryant and Garcia multimode flutter prototype [28]

The second Cornell prototype, developed by Li and Lipson, still uses a piezoelectric material, PVDF, as its mechanical to electrical energy converter. However, this prototype

makes use of forced excitation of an aeroelastic instability as its excitation source. Seen in Figure 28, they have produced horizontally and vertically oriented prototypes. In the horizontal prototype a stalk made of PVDF is attached to an isosceles shaped triangle "leaf" made of PVDF via a hinge. The harvester structure is then attached vertically to a 2 cm circular cylinder oriented in the same manner so the cylinder provides a vortex inducing bluff body. With this setup there are two potential excitations that may be responsible for the unstable periodic motion of the flexible body: first is the external harmonic forcing field caused by vortex shedding from a circular cylinder (bluff body); second is the unsteady forces and moments induced by the vortices shed from the trailing edge of the flexible plate or film, which is called a self-induced effect. Li and Lipson still believe it to be an open question for more examination [48]. Their vertically oriented prototype makes use of the second excitation, producing a self-inducing flutter from vortex shedding of the trailing edge of the piezo-leaf. Similar piezoelectric energy harvesters to Li and Lipson's horizontally oriented prototype have been developed for hydropower harvesting, [54] and [57]; again, a bluff body induces excitation in a "flag" of piezoelectric material due to vortex shedding of the flowing water.

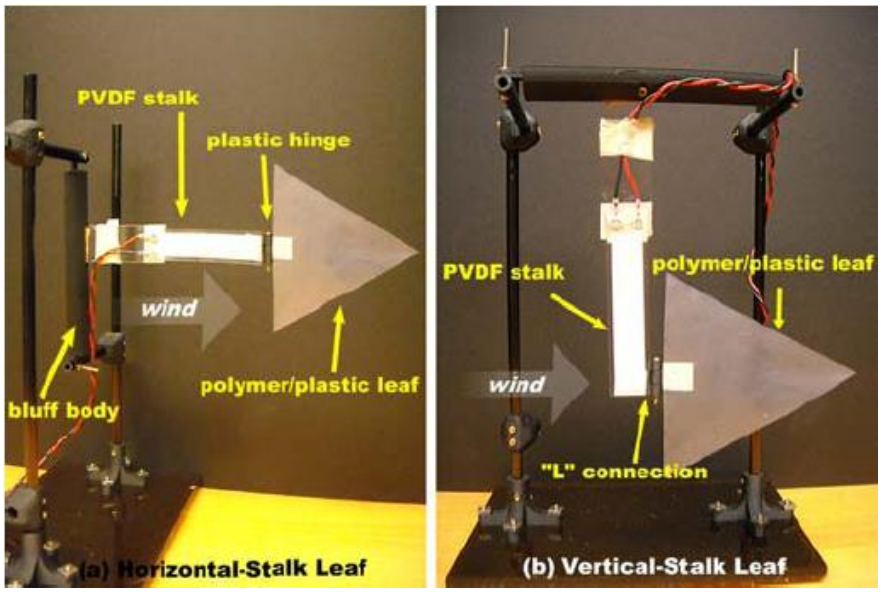

Figure 28: Li and Lipson's forced excitation of an aeroelastic instability prototype [48]

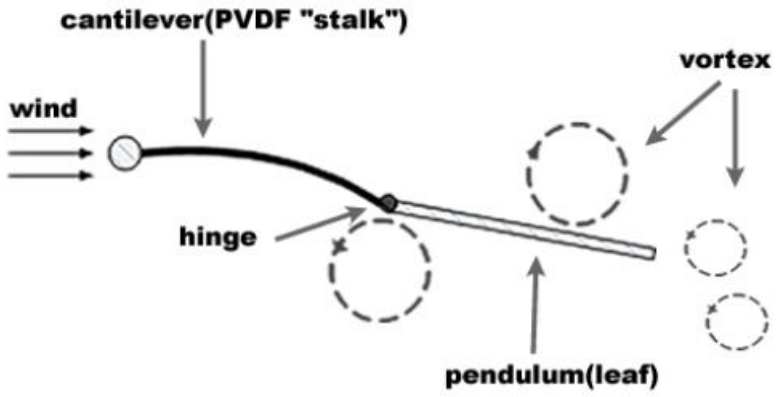

Figure 29: Bluff body/hinge configuration of Li and Lipson's horizontally oriented piezoleaf [48]; vortices are induced via a bluff body and trailing edge of the piezo-leaf

5.0 LARGER DEVICE DESIGN & EXPERIMENTS

Wind turbine installation locations are greatly limited the turbine's effectiveness in only Class 3 wind resource regions of higher. Yet, Class 1 and Class 2 ratings still potentially corresponds to ≈100 W/m^2 and ≈150 W/m^2 of land which we must be compelled to harvest, especially considering they correspond to the majority of land mass in the U.S. However, for traditional turbine configurations a number of significant issues still preclude widespread use.

Wind speed continues to be a challenge; optimum performance occurs in a narrow range around ≈12 mph, while most systems do not operate at all under ≈8 mph. Placement, for reliable performance turbines require steady flow conditions, in open locations, without turbulence caused by obstacles such as buildings, trees, hills, or homes. Thus, precise siting is required to access non-erratic wind flow of sufficient velocity. Installation costs are also expensive; micro-scale installation costs are always higher than macro-scale installations because the construction effort can not be distributed over a large number of turbines [7].

A design similar to the Humdinger Wind Energy, LLC medium size Windbelt is pursued: an aeroelastic instability energy harvester (AIEH) whose "lifting surface" is made of a 1" (2.54 cm) wide (dimension from the leading edge of the lifting surface to the trailing edge) fixed/fixed mylar-coated taffeta (kite material) belt/beam, which utilizes electromagnetic induction (EMI) as the mechanical to electrical energy conversion medium. In the Humdinger design disc magnets are attached to the top and bottom of the belt near *one* of the fixed ends. When the mylar coated belt is excited these magnets plunge in and out of two fixed solenoids wound by copper magnet wire, which are fixed to the metal support structure that boxes in the belt (again see Figure 11 in 2.2.3). Much of Humdinger Wind Energy, LLC research efforts pertain to developing the design for macro-scale and third world applications

in operating wind classes similar to that of wind turbines. However, very little research has been conducted that correlates to wind classes below Class 3 or the characterization of the device's stable limit-cycle oscillation (LCO). Capable of excitation and power production in sub-Class 1 (<9.8 mph) wind resource regions as well the higher resource regions, an AIEH presents a viable, new, and sustainable option for wind energy harvesting. To better understand and optimize this ability, an AIEH is developed.

5.1 HORNET DESIGN

This AIEH, dubbed the "Hornet" harvests the energy of aeroelastic flutter phenomenon. Optimization in sub-Class 1 wind resource regions begins with experimentation at various belt lengths and tension configurations. The implementation of smart materials, capable of producing energy due to deflections, may further increase the plateau of power output and is therefore worthy of inspection.

5.1.1 INITIAL CONSTRUCTION

In order to allow for a wide range of test configurations, the prototype needs to be adjustable in length, allow for a wide range of belt widths, and also have the ability to incrementally change the belt's tension. The design enables isolation of the belt's excitation from any bluff body/boundary conditions caused by the structure of the prototype itself. In other words, the structure of the prototype is designed to limit the potential effect it will have on the wind flow crossing the belt, helping to isolate the dynamics of the belt's excitation alone.

A similar base structure for the device is modified from a previous senior design team's design, shown in Figure 30, which is a design capable of being built for a unit price of less than $50. In their design they wrapped the belt around a polyvinyl chloride (PVC) base structure. Though only the top belt is exploited to harvest energy, the wrapped configuration helps to equalize the moment forces produced by the tension of the belt on the side supports of the device. The belt is tensioned by a direction varying ratcheting wrench. The belt

is wrapped around a cast acrylic rod whose rotation along its center axis is controlled by the ratcheting wrench. The direction varying feature of the wrench allows for incremental tightening and loosening of the belt. The wire coil solenoids are mounted on a stationary cast acrylic structure, which attempts to allow for free travel of the magnets in and out of the coils. As shown below, the total length of the 1"(2.54 cm) wide belt is set at 34"(0.864 m).

Figure 30: Senior design team AIEH

Since the new design needs to have the ability to adjust in length a different base material (instead of PVC) is used. For this purpose 80/20 Industrial Erector Set provides the best center core structure of the device. The material is strong, stiff, and provides easy assembly which saves time and allows for easy disassembly if necessary. A linear motion bearing allows the center support of the prototype to adjust in length. The final prototype permits the length to vary from 14" (35.56 cm) to 7' (2.13 m). The sides of the device are made from two 18" (45.7 cm) tall by 12" (30.5 cm) wide sheets of 3/4" (1.91 cm) thick cast acrylic. The increased size of the sides of the device, from the previous senior design team's device, helps to eliminate the affect the center rod of the device has on the wind flow field, as well as giving space for the testing of multiple belt widths and numbers. Initially two belts are chosen to be used since they may be spread evenly along the width of the device's sides, helping to keep the moments created at the connections with the 80/20 core structure to a minimum. However, the subsequent experiments are only performed on the belt initially exposed to the flow. The tensioning device for the belts utilizes the same idea as the previous senior design team's tensioning device; a ratcheting wrench mounted with a cast acrylic cylinder. Again the wrench can directionally vary, allowing for easy incremental tightening and loosening of the belt.

The wire coil solenoids are mounted on 3/8" (0.953 cm) thick cast acrylic sheet structures that align the solenoids over and under the magnets on the belt. Unlike the previous design however, the structures supporting the top and bottom solenoids are not stationary, can be adjusted, and are independent from one another. Similar to the adjustable hinges of the MiniHornet, the adjustable ability of the support structures allows the coils to be best aligned for the travel of the magnets. The solenoids are fabricated in an identical fashion to the MiniHornet (utilizing the stereolithography (SLA) machine), however the bobbins, or solenoid housings, are made with a different geometry, which can be seen in Figure 31 and consequently have a different number of turns and nominal resistance values. Again, to check their approximate likeness, the nominal resistance value of each solenoid is measured; 65 Ω, 75 Ω, 60 Ω, and 70 Ω.

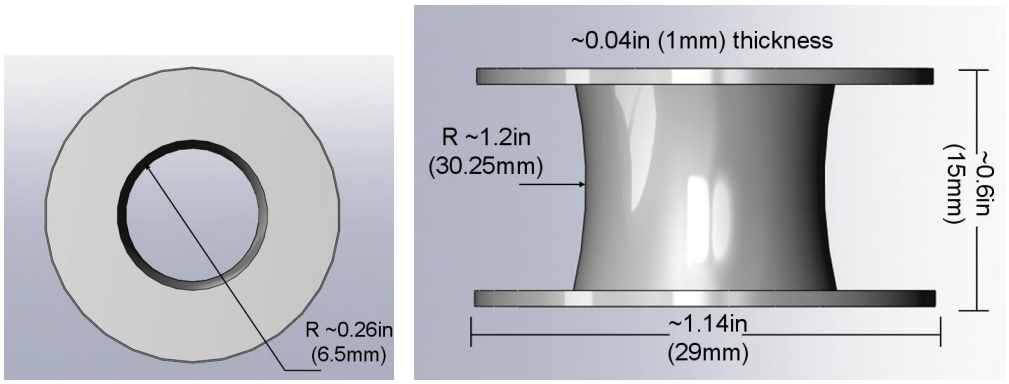

(a) top view (b) side view

Figure 31: Hornet prototype solenoids; for EMI Harvesting

5.2 HORNET CHANGE OF LENGTH EXPERIMENTS

It is believed experiments at various lengths and tensions may zero in on a "best" configuration for power generation of this AIEH, at a chosen air speed; considering alterations in belt length and tension change the belt's dynamics. In our case a wind flow velocity of ≈5 mph (2.24 m/s) is chosen.

5.2.1 INITIAL EXPERIMENTS WITH A BLUFF BODY

To examine the belief that AIEHs respond favorably in turbulent flow conditions caused by bluff bodies inherent to civil structures, experiments are performed to determine the average power output of our AIEH, the Hornet, in a constant velocity wind flow, with and without a bluff body present in the flow prior to the belt of the Hornet. The bluff body, as if looking at it with the Hornet directly behind, is 5.5" (12.7 cm) in depth, 9" (22.9 cm) in height (leaving 9" vertical differential between the top of the bluff and the belt of the Hornet), and is placed so that the front leading edge of the bluff body is 12"(30.5 cm) in front of the front leading edge of the Hornet's belt, as is seen in Figure 32. A box fan, placed so that a vertical and horizontal plane would pass through the direct center (horizontal and vertical) of both the Hornet's belts and the blades of the box fan, is turned on to the lowest speed and moved closer and farther from the belt of the Hornet until the average wind speed across the span of the Hornet is approximately 5 mph (2.24 m/s). To assess the average wind speed across the span of the belt an anemometer is utilized. Three measurements of the wind speed are taken (at one end, in the middle, and at the other end of the belt), and averaged. If the average is not approximately equal to 5 mph (2.24 m/s) then the fan is moved and the process is repeated until the approximate average wind speed crossing the belt is 5 mph (2.24 m/s). The experiment is performed as follows:

Table 1: Hornet initial bluff body experiment equipment

Name	model #	serial #
Tektronic Digital Oscilloscope	TDS 2014B	CO32007
Dwyer Anemometer	VT-200	08120089
Attaché 1G USB flash drive	E1GB	511-061020032
Matlab software	R2009b	N/A

The procedure for the experiment are as follows:

1. Adjust the length of the Hornet to the desired test length.
2. Place/move fan to position in front of the Hornet.

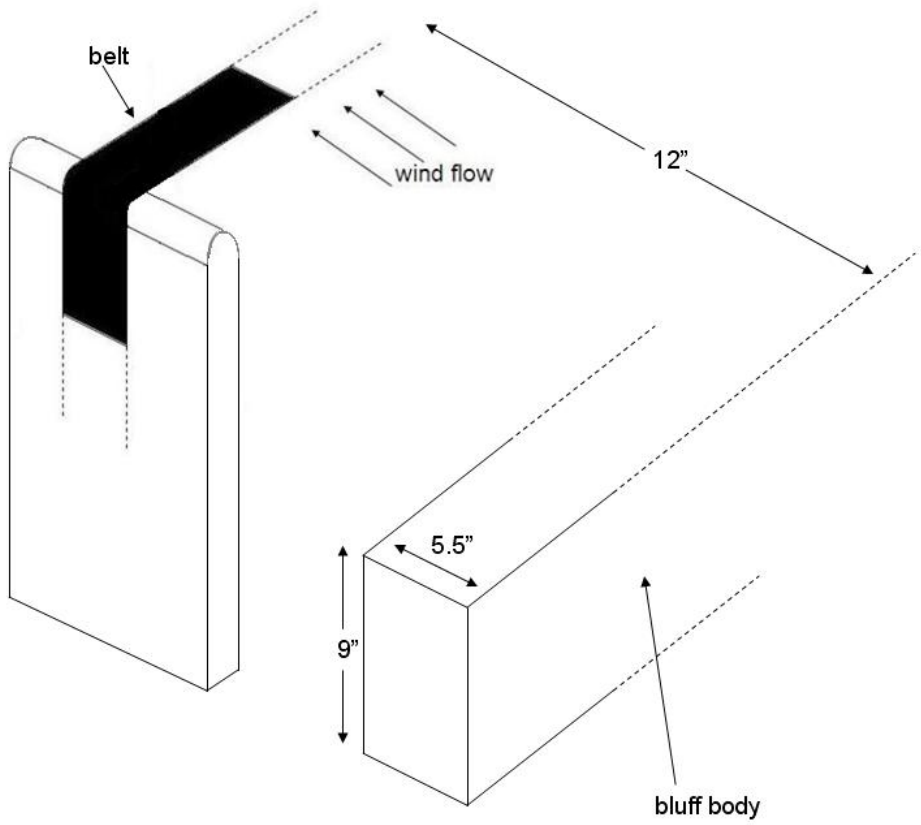

Figure 32: Hornet initial bluff body experiment setup

3. Test the wind velocity with the anemometer in the middle of the belt and on both ends (three measurements) and then average the data. If the average is not approximately 5 mph repeat steps 2 & 3.
4. Adjust tension in belt until the qualitatively best tension is discovered; best being that which allows for large amplitude and frequency of oscillation.
5. Connect the four leads from the digital oscilloscope to each of the Hornet's four solenoids.
6. Plug flash drive into the digital oscilloscope.
7. Press the “Print” button on the digital oscilloscope and wait as the oscilloscope acquires the data.
8. Place bluff body in front of the Hornet at desired location.
9. Repeat step 7.

10. Remove bluff body and repeat all procedures until all desired lengths have been tested: 14", 20", 26" and 32" (35.6 cm, 50.8 cm, 66.0 cm, and 81.3 cm, respectively).

Results: The voltage data, acquired by the digital oscilloscope and saved to the flash drive as a Microsoft Excel file, is loaded and manipulated in Matlab. The code loads and saves the voltage data, manipulates it as in Equation 5.1, then saves the new power data; V is measured voltage, Δt is the time step between each voltage measurement, R is the load resistance value, and T is the total measurement time. A plot is then made of the average power versus the belt length; with and without the presence of the bluff body.

$$P = \frac{1}{T}\sum_{i}^{n}\frac{V_i^2}{R}\Delta t \tag{5.1}$$

As is seen in Figure 33 it appears as though the most power in 5 mph wind flow is produced around a belt length of 26" (66.0 cm). The figure also shows the Hornet results favorably, at each length, with a bluff body present in front of it. This may lead one to believe the Hornet is indeed suitable for application in and around civil structures. More testing is necessary to validate these results. An unfavorable result, however, is the magnitude of power generation; nearly 3.5 mW (measurement uncertainty of 1.6×10^{-5}), which is more than an order of magnitude less than that which had been previously reported by the prior senior design team. A series of tests on the senior design team's prototype confirmed their results and also established the need for careful attention to the EMI generator design, as discussed in the following sections.

5.2.2 EMI GENERATOR REDESIGN

An investigation into the vast difference in power production between the Hornet and the previous senior design team's prototype led to the acquisition of a masters thesis by Agutu, "Characterization of Electromagnetic Induction Damper"[23], which discusses in depth how the relative dimensions between the magnetic translator and the coil affects the damping force and thus the power output. The largest realization is that the largest maximum damping force (a.k.a. power generation) possibly induced in a coil of set height occurs when the middle (of the height) of a magnetic translator of equal height to the coil is passing directly

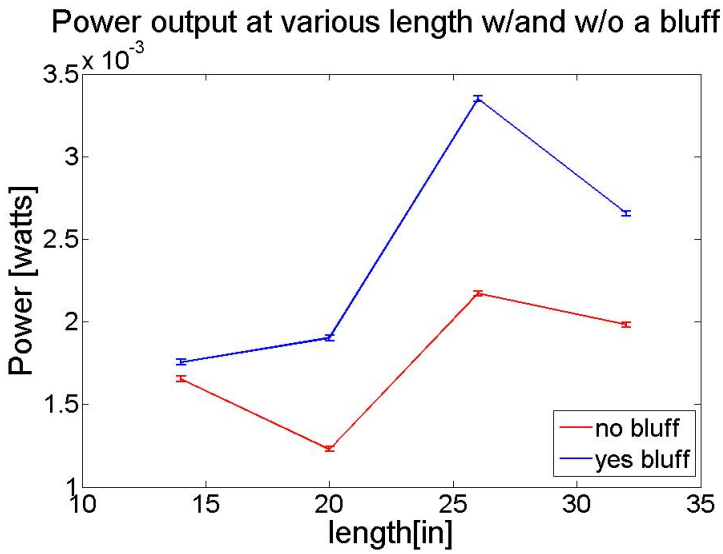

Figure 33: Hornet Initial Bluff Body Experiment Results; as also relates to power versus belt length

through the middle of the coil's height. Therefore, with a linear EMI damper/generator the height of the magnetic element and the wire coil/solenoid should be made the same. This leads to a geometric redesign of the bobbins used to make the solenoids, as seen in Figure 34.

Again, to check their approximate likeness, the nominal resistance value (open circuit/no applied load resistance) of each solenoid is measured; 330 Ω, 305 Ω, 330 Ω, and 305 Ω. To make the excitation symmetric the 330 Ω and 305 Ω pairs of solenoids are utilized as the top and bottom solenoid pairs, respectively.

5.2.3 EMI REDESIGN & SMART MATERIAL IMPLEMENTATION EXPERIMENTS (BLUFF BODY)

To reexamine how a change in belt length affects power production at a low wind speed, examine how the introduction of an active ("smart") belt material may enhance power generation, and assess the effects of redesigning the EMI solenoids, change of length experiments are again performed. The introduction of an active smart belt material may have

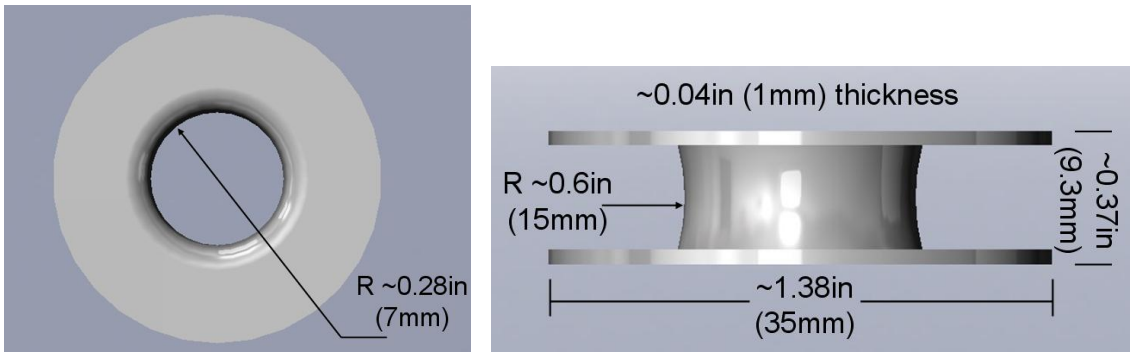

(a) top view

(b) side view

Figure 34: Hornet EMI Generator Solenoid Redesign

the potential to dramatically increase the power generation of an AIEH. Similar to the vibration energy harvester described in section 4.2.1, which utilize the oscillation of structures to provide cycle strain energy that can then be converted into electrical energy, the LCO of the Hornet provides a potential resource for an active smart material to enhance power generation. To test this hypothesis strips of a piezoelectric polymer, polyvinylidene fluoride (PVDF), are attached to the top face of the Hornet's belt.

The ferroelectric polymer PVDF is chosen as the active smart material because its highly non-reactive nature is ideal for environments and conditions an AIEH, such as the Hornet, may face in future applications. PVDF is also an ideal piezoelectric polymer for power generation in a bending mode oscillation, similar to the vibration harvester in [42] (seen in Figure 26).

Inspection into implementing PVDF includes measurements of the open circuit voltage produced via the newly redesigned EMI generators and 5" x 1" (12.7 cm x 2.54 cm) PVDF strips 1.58×10^{-5}" thick (0.4 μm). Each of the experiments is broken down into two trials (with/without a bluff body) at five different belt lengths, 14", 21", 28", 35", and 42" (35.6 cm, 53.3 cm, 71.1 cm, 88.9 cm, and 1.07 m, respectively). For a belt length of 14" one PVDF strip is chemically bonded to the center of the belt's length by M-coat adhesive (typically utilized for strain gages). One additional strip of PVDF is then adhered to the

belt for each step increase of the belt's length. Therefore, at a belt length of 21" there are two PVDF strips, at 28" three PVDF strips, and so on. The center of the strips length are placed 7" away from each other so that at each belt length the PVDF strips are spread evenly and symmetrical across the belt. Multiple belt lengths are taken to further understand what range of belt lengths may be best for the Hornet to harvest energy in sub-Class 1 (at ≈5 mph) wind conditions. The experiment is performed as follows:

Table 2: Hornet Smart Material Implementation Experiment Equipment

Name	model #	serial #
Tektronic Digital Oscilloscope	TDS 2014B	CO32007
Tektronic Digital Oscilloscope	TDS 2014B	CO31095
Tektronic Digital Oscilloscope	TDS 2014B	CO33644
Dwyer Anemometer	VT-200	08120089
Attaché 1G USB flash drive	E1GB	511-061020032
Corsair Flash Voyager 8G USB flash drive	G08G	09426007-0
Attaché PNY 8G USB flash drive	CEFG	N/A
Matlab software	R2009b	N/A

The procedure for the experiment are as follows:

1. Ensure box fan is turned off.
2. Adjust the length of the Hornet to the desired test length, starting with 14".
3. Chemically mount the PVDF strip (added at each incremental increase in belt length) with M-coat adhesive as specified above.
4. Wait one full day for the adhesive to dry.
5. Place/move fan to position in front of the Hornet and turn on.
6. Test the wind velocity with the anemometer in the middle of the belt and on both ends (three measurements) and then average the data. If the average is not approximately 5 mph, repeat steps 5 & 6.
7. Adjust tension in belt until the qualitatively best tension is discovered; "best" being that which allows for large amplitude and frequency of oscillation.

8. Connect the four leads from one digital oscilloscope to each of the Hornet's solenoids.
9. Connect the lead(s) from the other digital oscilloscope(s) to each of the PVDF strips. Of course for each increase in length there will be an addition PVDF strip, therefore at the fifth length change a third digital oscilloscope will be necessary since the oscilloscopes contain only four channels
10. Plug flash drives into the digital oscilloscopes.
11. Press "Print" button on digital oscilloscopes and wait as the oscilloscopes acquire the data.
12. Place bluff body in front of the Hornet at desired location.
13. Repeat step 11.
14. Remove bluff body and repeat all procedures until all desired lengths have been tested: 14", 21", 28", 35" and 42" (35.6 cm, 53.3 cm, 71.1 cm, 88.9 cm, and 1.07 m, respectively).

Results: Similar to the previous experiments, the voltage data acquired by the digital oscilloscope and saved to the flash drives as Microsoft Excel files are loaded and manipulated in Matlab. The code saves the voltage data and manipulates it for power generation. Again for the EMI data Equation 5.1 is used, however for the PVDF data Equation 5.2 is used; where w, l, and τ are the PVDF strips' width, length, and thickness, respectively, and d_{31} and g_{31} are the strain $[\frac{C/m^2}{N/m^2}]$ and voltage constants $[\frac{V/m}{N/m^2}]$, respectively. F is the frequency of oscillation of the PVDF strips, which directly corresponds to the belt oscillation frequency.

$$P = \frac{wld_{31}\sum(\mathrm{V}^2)\Delta t F}{\tau g_{31} T} \tag{5.2}$$

Plots (Figure 35) are then produced of the power output by the EMI generators (left) and PVDF strips (right) for changes in belt length. Once again for every belt length the bluff body case produces more power than the non-bluff body case. These, combined with the previous results, may lead one to conclude that an AIEH, like the Hornet, is indeed suited and in fact shows an enhancement in performance for application in erratic wind conditions surrounding civil structures.

The plots also show that the EMI generators produce the most power with a bluff body at a belt length of 35" (88.9 cm); nearly 30 mW (measurement uncertainty of 2.3×10^{-6}) of power. This order of magnitude increase in power output is on the same order of magnitude

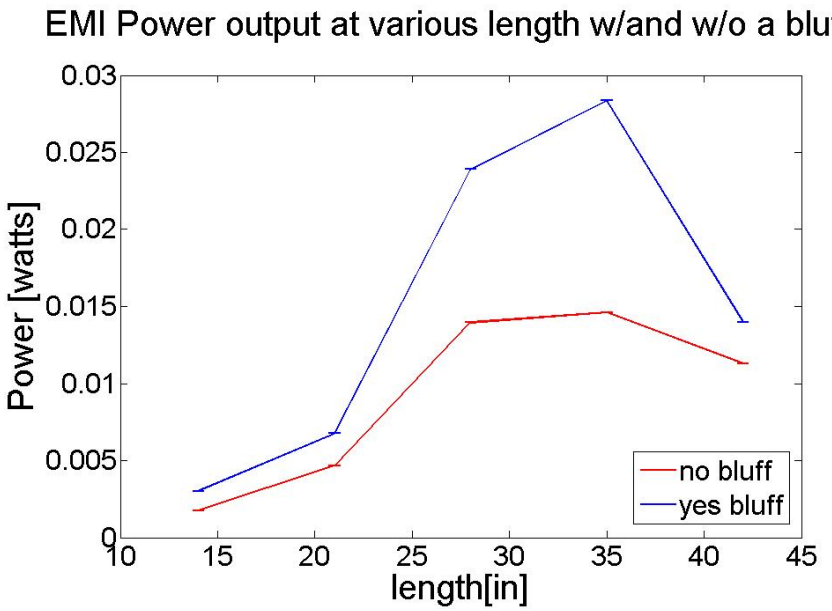

(a) EMI power output

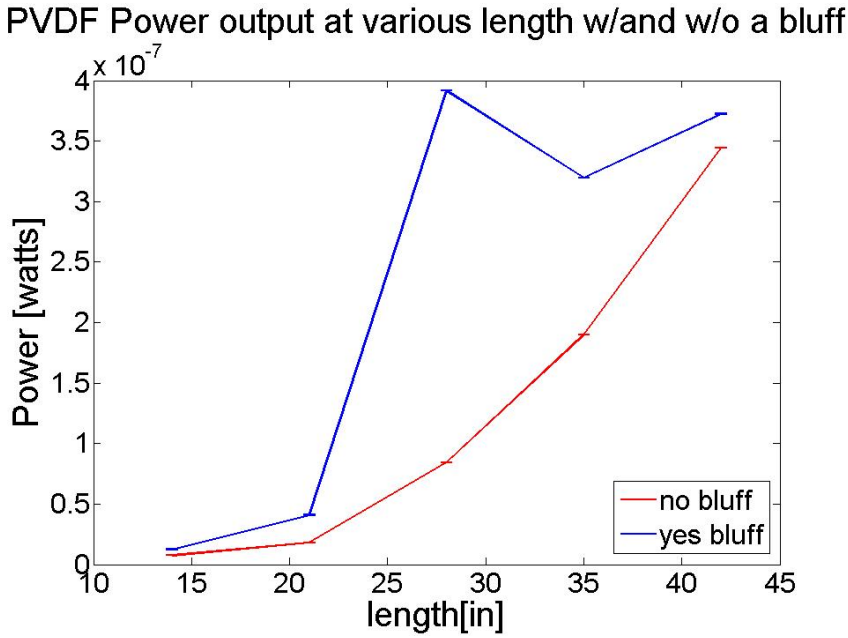

(b) PVDF power output

Figure 35: Hornet Smart Material Implementation Results

as the previous senior design team's results. It proves the EMI generator redesign is a success and the previous generator design is the reason for the lack of power output compared to the senior design team's previously reported results. It is the belief that further redesign of the mechanical to electrical energy conversion medium could lead to higher average output power. The plots also show that the PVDF strips produce the most power at a belt length of 28" (71.1 cm), with four measured PVDF strips; around 0.4 μW (measurement uncertainty of 4.9×10^{-10}) of power, which is far less than 1% of the total power. It appears as though the PVDF strips do not have a high enough power density for this type of energy harvesting and considering the associated additional cost to implement PVDF into the belt, the use of active smart materials is not desireable for this type of energy generation. Both of these results and the results from the first set of length change experiments seem to show that the best Hornet belt length for power generation in ≈5 mph (2.24 m/s) flow is in the range of 26" to 35"(66.0 cm to 88.9 cm).

5.3 TENSIONING DISCOVERY

During preliminary testing it was observed a slight force applied to front leading edge of the belt dramatically increases the belt's excitation, as depicted in Figure 36. Therefore, the belt seems to respond favorably when the tension of the leading edge of the belt is slightly more taunt than the trailing edge. It is the belief that this phenomenon may be moving the elastic axis of the lifting surface forward, allowing for the plunge and twist modes of the multimode flutter to coalesce easier/faster, which may be harnessed to increase the Hornet's potential power output.

5.3.1 TENSIONER IMPLEMENTATION

To test the viability of increasing the Hornet's power output, tension distribution alternators are designed and installed on the Hornet to apply a tension gradient from the front leading edge of the belt to the back edge. Four devices are installed, one for each side of both belts

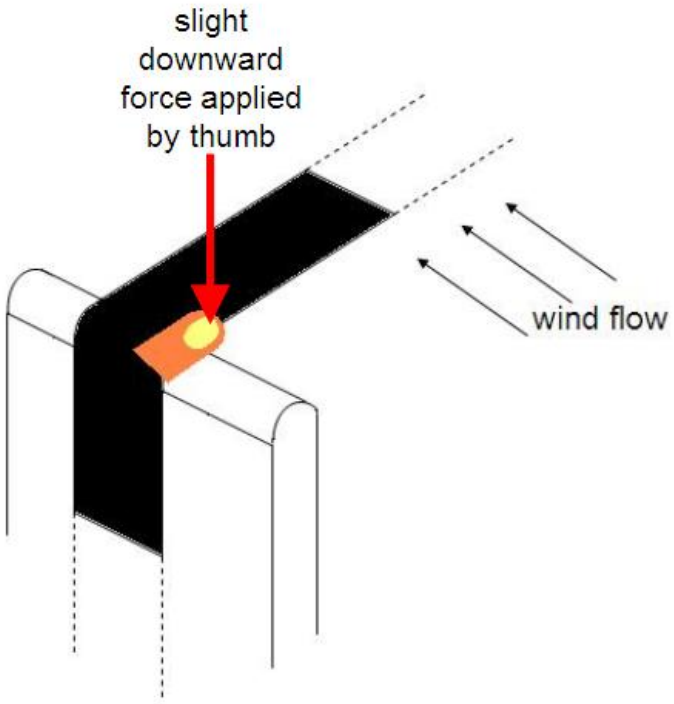

Figure 36: Accidental Belt Tension Discovery

of the Hornet. The four devices are all constructed similarly; half pipes of 1.5" (3.81 cm) diameter PVC piping, sitting on cast acrylic shelves, which pivot at their back sides (farthest from the leading edge of the belt). Therefore, when forced to swing open by a bolt a greater tension is applied to the front edge of the belt than the back; a second directionally opposed bolt locks the PVC half pipe in the desired position. A cross-sectional view of one device is seen in Figure 37.

As one may notice the diagram does not include the bolts used to lock the PVC half pipe in position or the pin that allows the PVC pipe to swing open. The pin goes vertically through the arch of the PVC pipe and are held in place by the cast acrylic shelf and an additional "shelf" of cast acrylic located in the center of the PVC pipe's arc; forming a hinge. The bolts are positioned next to each other 3/4" (1.91 cm apart, on the front side of each PVC pipe (prior to belt), in the center of the pipe's arch. While one bolt may be

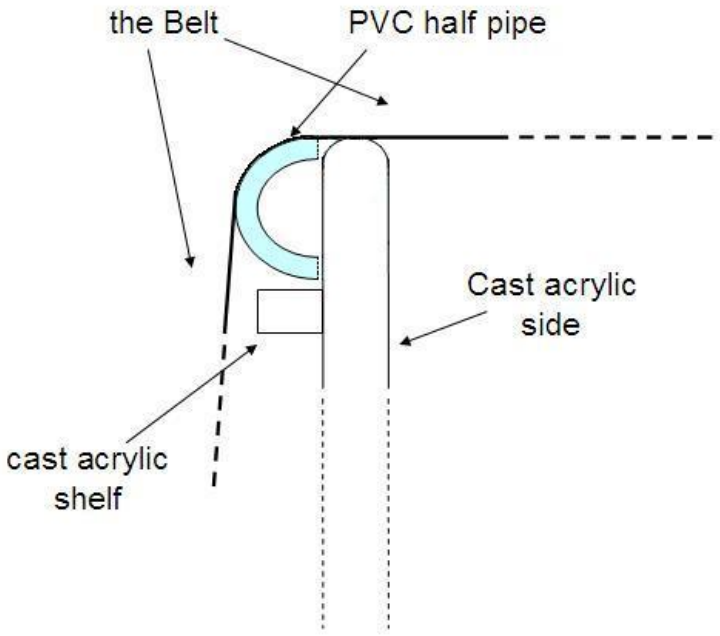

Figure 37: Belt Tension Gradient Device

tightened to pivot open the PVC pipe the other directionally opposed bolt is loosened to allow for the pivoting, and is tightened to lock down the PVC pipe in it's desired position. This allows for the tension gradient to be applied as desired.

An experiment is performed to test the belief that a tension gradient may increase average power output; without a bluff body, at a belt length that is believed to be "ideal" for harvesting energy in 5 mph wind flow. A length of 34" (86.4 cm is settled upon as the ideal length after numerous qualitative trials are performed in the belt length range of 26" to 35". This belt length also happens to be the same length as the previous senior design team's prototype, therefore a similar comparison may be made. The five PVDF strips remain on the belt to further test whether active smart materials possess the power density to be utilized in AIEH or not. The experiment is performed as follows:

Table 3: Tension Gradient Validity Experiment Equipment

Name	model #	serial #
Tektronic Digital Oscilloscope	TDS 2014B	CO32007
Dwyer Anemometer	VT-200	08120089
Attaché 1G USB flash drive	E1GB	511-061020032
Corsair Flash Voyager 8G USB flash drive	G08G	09426007-0
Attaché PNY 8G USB flash drive	CEFG	N/A
Matlab software	R2009b	N/A

The procedure for the experiment are as follows:

1. Adjust the length of the Hornet to 34".
2. Place/move fan to position in front of the Hornet.
3. Test the wind velocity with the anemometer in the middle of the belt and on both ends (three measurements) and then average the data. If the average is not approximately 5 mph repeat steps 2 & 3.
4. Adjust tension in belt and the tension distribution alternators until the qualitatively best tension is discovered; best again being that which allows for the largest amplitude and frequency of oscillation.
5. Connect the four leads from the digital oscilloscope to each of the Hornet's four solenoids.
6. Connect the leads from the two other digital oscilloscopes to each of the five PVDF strips.
7. Plug flash drives into the digital oscilloscopes.
8. Press the 'Print" buttons on the digital oscilloscopes and wait as the oscilloscopes acquire the data.

Results: As with the two previous experiments, the a Matlab script is used to load and manipulate the acquired voltage data. In this case no plot is produced but the power production is output to the command window. In this trial, 48.3 mW and 0.15 μW average power is produced by the EMI generators and PVDF strips, respectively. This is more than

a 200% power increase for the EMI generators from the previous *non-bluff body* experiments (only about 15 mW was produced previously), which proves that a tension gradient applied to the belt is capable of producing a higher power output than an even distributed belt. It is the belief that a tension gradient helps to increase the coupling between the plunge and twist modes of the aeroelastic flutter phenomenon experienced by the Hornet's belt, which increases both the amplitude and frequency of oscillation. The PVDF results, being of the same order of magnitude, also reinforces the belief that active smart materials are not suitable for implementation on an AIEH of this type.

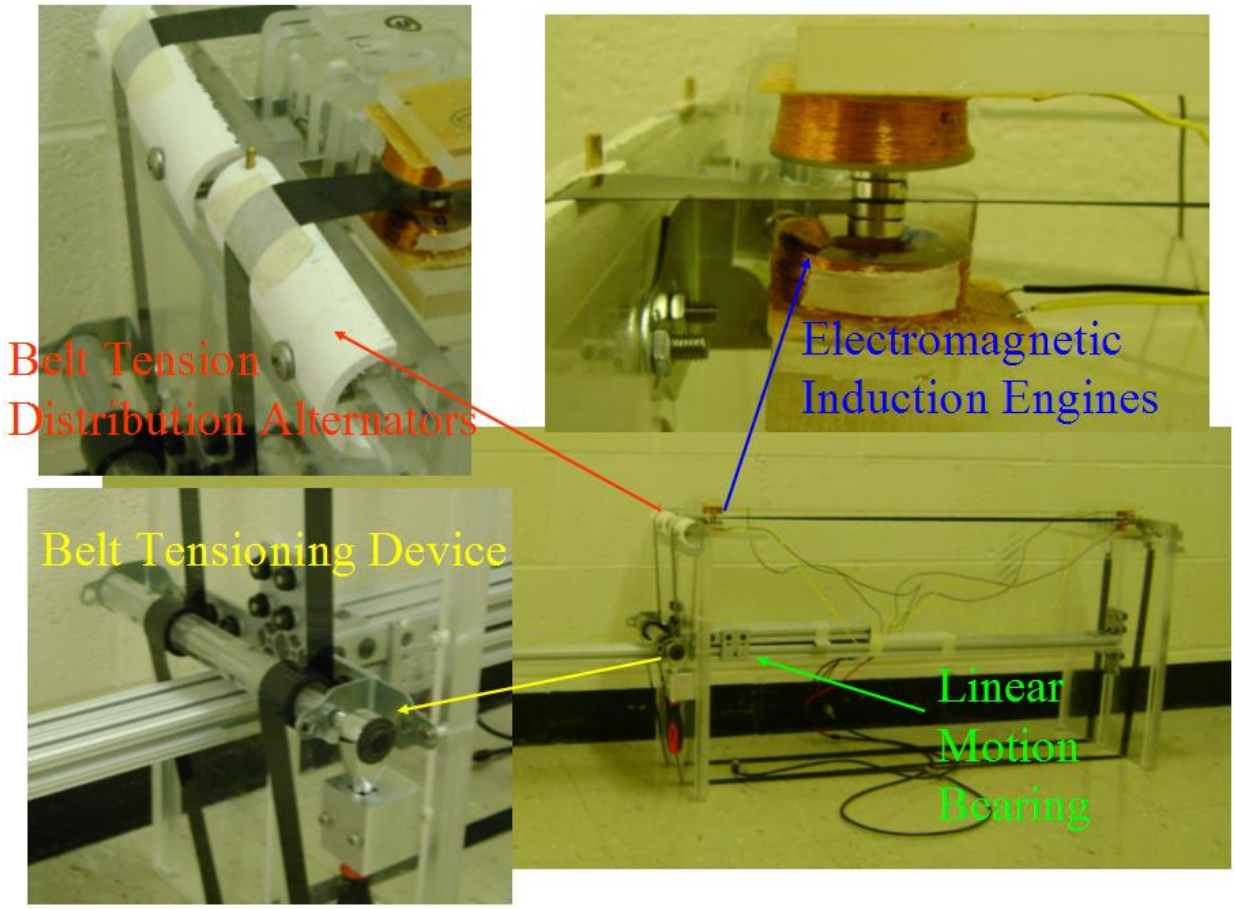

Figure 38: The Hornet

6.0 MINI DEVICE DESIGN & EXPERIMENTS

In an effort to characterize the limit-cycle oscillation (LCO) experienced by an aeroelastic instability energy harvester (AIEH) in a controlled experimental environment, a mini AIEH is designed and constructed for testing in a wind tunnel.

6.1 MINIHORNET CONSTRUCTION

Again paralleling the Windbelt, the design, dubbed the "MiniHornet" (seen in Figure 39), also uses a fixed/fixed mylar coated taffeta belt/beam with N50 grade Neodymium super disc magnets attached to the bottom and top of the belt, however, again they are attached symmetrically near each of the fixed ends of the belt, not just at one end. Four solenoids are aligned to each set of disc magnets so as to allow the magnets to plunge in and out of the solenoids while the belt is excited. Considerations for the limited experimental space, 6" x 6" (15.2 cm) cross-section wind tunnel, takes high priority in the design. Also taking high priority is the ability to adjust the positioning of the four electromagnetic induction (EMI) solenoids so as to allow the magnets to plunge as deeply into the solenoids as possible without obstructing the belts/magnets motion.

The solenoids are made with copper magnet wire. The bobbins, or solenoid housings, are rapid prototyped on the University of Pittsburgh's stereolithography (SLA) rapid prototyping machine from 3D Systems, Inc., the geometry is seen in Figure 40. To construct the four solenoids a lathe is used to wrap each bobbin with 36 gauge (AWG) magnet wire. The goal is to have solenoids capable of producing equal power, and consequently approximately equivalent damping forces, which are produced during power generation. This is attempted

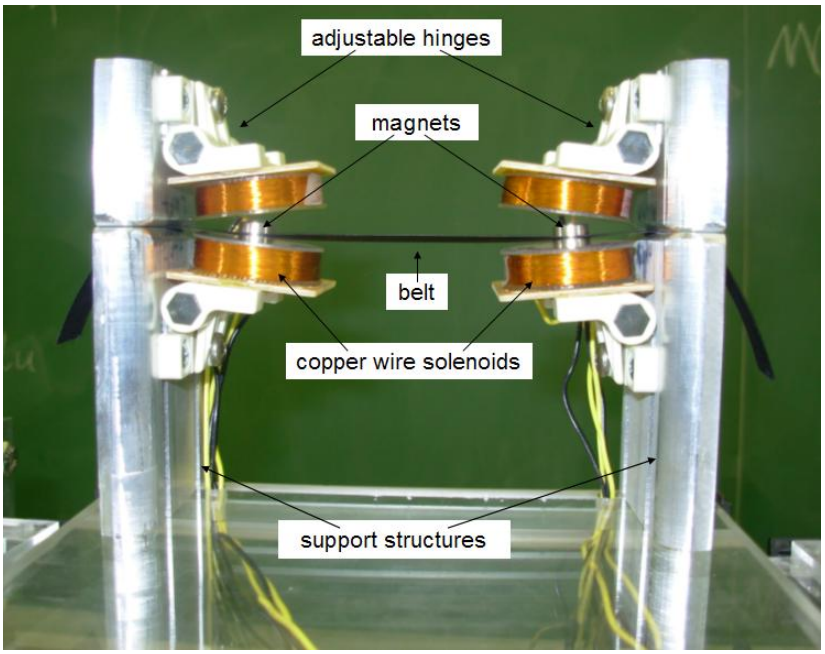

(a) diagram

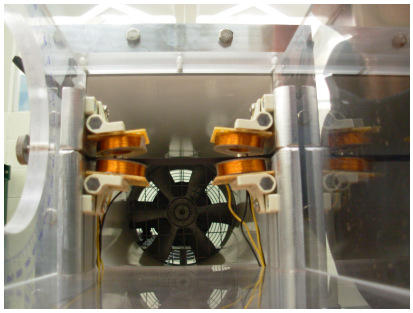

(b) inside wind tunnel

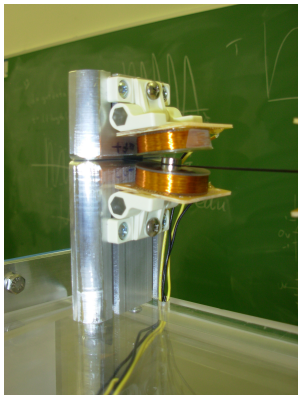

(c) support structure

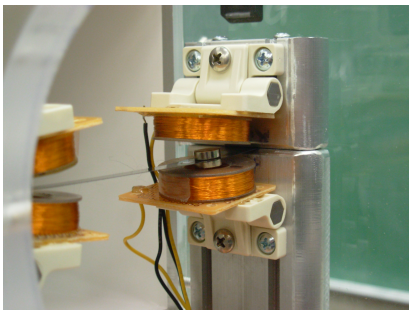

(d) EMI generator

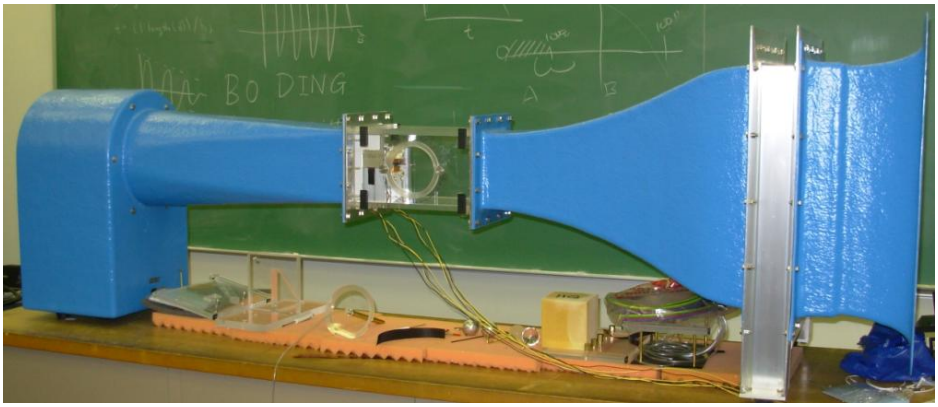

(e) wind tunnel

Figure 39: The MiniHornet

to allow for symmetric damping of the system from one end of the belt to the other. Since the production of electrical energy in a solenoid is dependent on the number of turns in the solenoid (magnetic flux remaining constant), as was shown in Equation 4.1, each solenoid is wound by the magnet wire at 125 RPM for 12 minutes resulting in ≈1500 turns. To check their approximate likeness, the nominal resistance value (open circuit/no applied load resistance) of each solenoid is measured; 265 Ω, 270 Ω, 275 Ω, and 280 Ω. To make the excitation as symmetric as possible the 265 Ω and 270 Ω pair of solenoids are used as the bottom solenoid pair, whereas the 275 Ω and 280 Ω pair of solenoids are used as the top solenoid pair. One should notice that this is the same design seen on the Hornet after the EMI generator redesign. Though made from the same housing design, the magnetic wire is wound around the bobbins for a slightly shorter time, therefore containing a smaller number of turns then the solenoids of the Hornet.

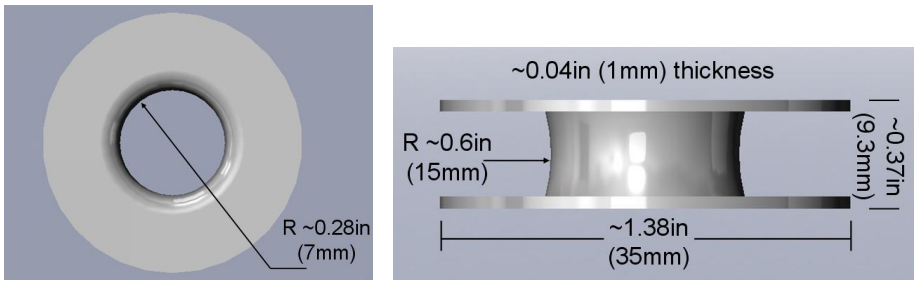

(a) top view (b) side view

Figure 40: MiniHornet prototype solenoids

In an effort to make the belt support structure small and unobtrusive to the wind flow in the wind tunnel, which in effect maximizes the possible belt span length, the material chosen is 6061 aluminum because it provides the strength to allow the two fixed end points of the belt to be rigid. However, it should be emphasized that material selection parameters in prototype development may vary substantially from those of mass production. The ability of the solenoids to be adjustable is accomplished by utilizing adjustable friction hinges as the interface structure between the aluminum support structure and the wound copper wire solenoids. T-slots in the support structures allow the hinges to be attached simply via nuts and bolts and permits them to traverse vertically. The vertical movement provided by the

t-slots and the inherent adjustable nature of the friction hinges allows the solenoids to be properly aligned to the plunge motion of the fluttering magnets.

Each of the two structures are 1/2" (1.27 cm) in thickness and 2.25" (5.72 cm) in depth, as if looking at the front leading edge of the belt (like was seen in Figure 39). The 1/2" thickness provides the proper amount of material for machining the hinges' t-slots, the required holes to connect the upper and lower parts of the support structures, and the holes required to connect the support structures themselves to the wind tunnel, while still providing enough strength for the structures to remain rigid. The top and bottom support structures sandwich together to pinch the belt into its suspended state. The bottom support structure is made to be 3" (7.62 cm) tall in order to place the belt directly in the center of the wind tunnel's cross-section. The top support height was made large enough in order for the T-slots to be long enough to allow the hinges to be properly manually adjusted to the belt/magnet's excitation. A Solidworks image of the left aluminum support structures is given in Figure 41.

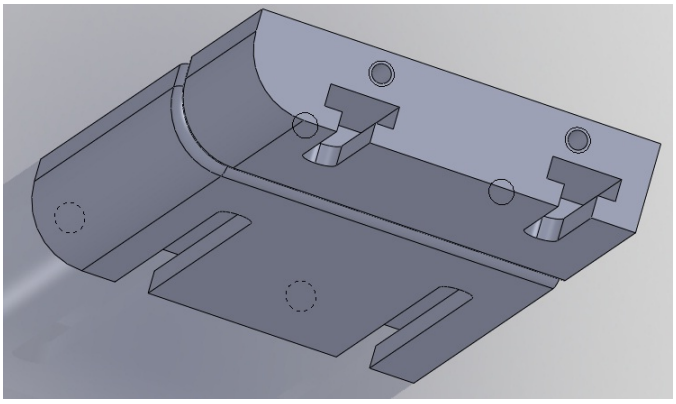

Figure 41: MiniHornet left support structures

After the MiniHornet parts are machined and the prototype is assembled, qualitative preliminary experiments are performed to settle upon a wanted belt configuration. For each configuration attempts the MiniHornet is placed into the wind tunnel and its response is visually observed. The goal is to find the best configuration that provide characteristics to allow for the largest excitation frequency and amplitude. The different configurations are achieved by altering the tension in the belt, as well as testing with EMI generators that utilize either one or two disc magnets per solenoid. After the preliminary experiments a set

tensioning of the belt is settled upon and the support structures are tightened down to hold the belt in this configuration for the entirety of all following MiniHornet experiments.

The belt configuration is set so as to have the front leading edge of the belt slightly more taunt then the trailing edge. This allows for an enhancement in performance, as was seen in section 5.3.1.1, and configures the back edge of the belt to droop slightly more than the front edge. At the middle of the belt's length, the front leading edge droops a 1/16" (1.59 mm) from the height of the fixed ends of the belt, whereas the back edge droops 1/8" (3.18 mm). EMI generators that use one disc magnet are chosen as the EMI generator setup and are placed in the center of the belt's width, with their center vertical axis 3/4" (1.91 cm) from each of the fixed ends of the belt. If one is attempting replicate the configuration, the results from the to be discussed section 6.3.2.1 should be replicated.

6.2 WIND TUNNEL SPECIFICATIONS

In an effort to maximize experimental control a wind tunnel from Engineering Laboratory Design, Inc. (Model #400) is used to provide the wind flow. The wind tunnel system is an Eiffel type, therefore air is drawn into the elliptical inlet through a honeycomb and screen pack and is accelerated through the contraction into the test section. The system air regains static pressure passing through the diffuser. Flow continues through the fan and is discharged to the atmosphere.

The test section sidewalls, floor, and ceiling are fabricated from 0.5" (12.7 mm) thickness, clear, GM grade, acrylic. The interior dimensions of the test section are: length, 12" (30.8 cm); height and width, 6"(15.2 cm). The cover and floor of the test section are removable and fitted with quick release fasteners. The support structures of the MiniHornet are mounted to this removable floor. The test section speed is controlled by varying the fan motor RPM. The speed within the test section is continuously variable from less than 5 fps (1.52 m/s) to greater than 50 fps (15.2 m/s). A surface plot, provided by the manufacturer, of this velocity profile is presented in Figure 42. As one can see, the velocity in the test section is slightly faster on the right side compared to the left.

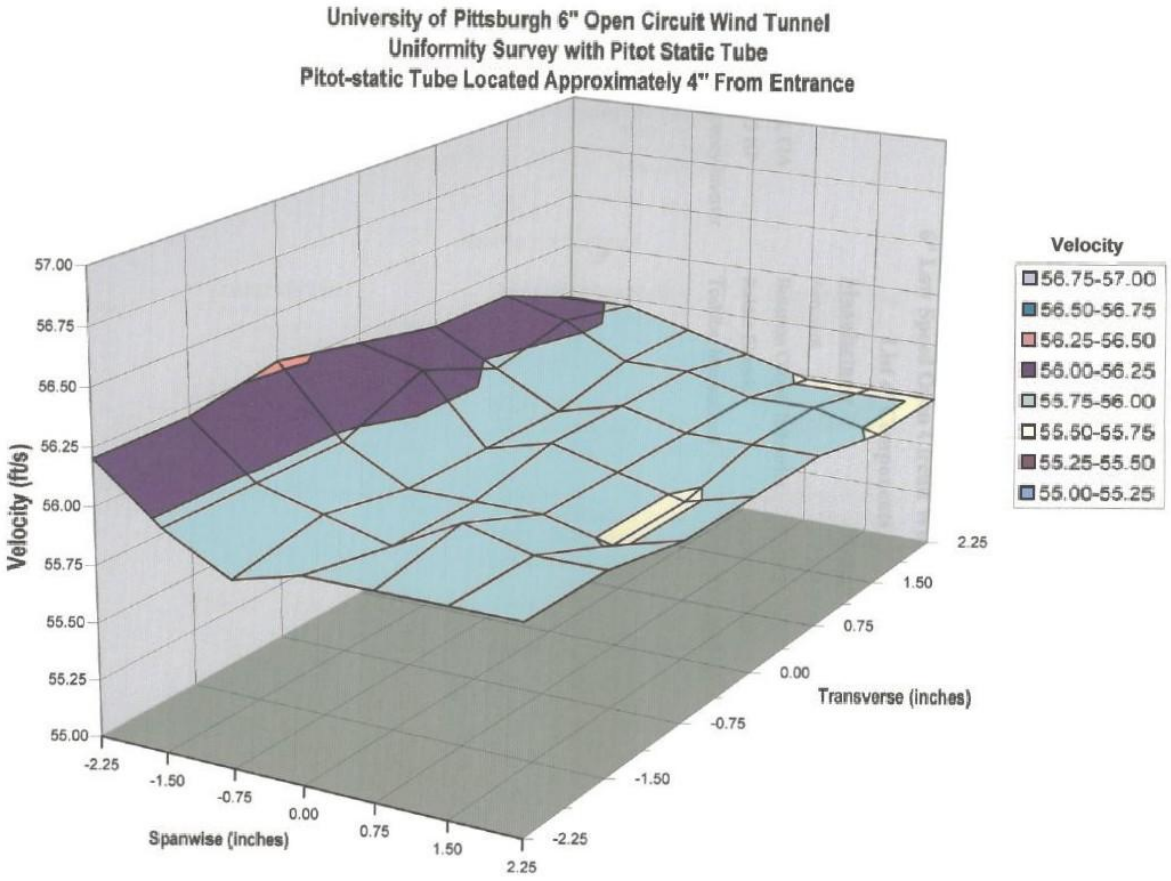

Figure 42: Wind tunnel test section velocity uniformity; as provided by the manufacturing company [9]. The velocity profile on the right side (facing the front of the MiniHornet) of the test section's velocity profile.

Table 4 gives the relation between the fan RPM and the wind velocity through the test section, as provided by [9]. In order to have an approximate value of the velocity at each frequency of the fan, from 20 Hz to 60 Hz (the tested flow velocity range), linear trend lines and their equations are found (as seen in Figure 43). These equations are then used to gain an approximate value for the velocity at each RPM value from $20 - 60$ Hz as seen in Table 5, with an average relative percent error of 0.56%.

Table 4: Wind tunnel velocity conversion; as provided by the manufacturing company [9]

Hz	10	15	20	25	30	35	40	45	50	55	60
fps	7.22	12.21	17.27	22.25	27.18	31.99	36.86	41.69	46.11	50.93	55.81
m/s	2.20	3.72	5.26	6.78	8.28	9.75	11.24	12.71	14.06	15.52	17.01

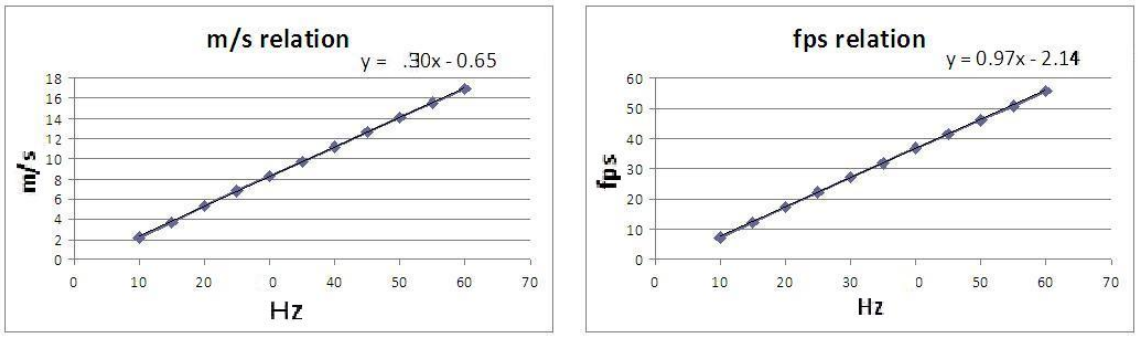

(a) metric

(b) english

Figure 43: Wind tunnel RPM vs wind velocity trendlines

6.3 DYNAMIC CHARACTERISTICS

With the aim to better understand the system, certain dynamic characteristics of the system need to be found. These characteristics can help in the optimization of power production as well as give a better understanding of the system's response for future modeling.

6.3.1 POWER vs. LOAD & VELOCITY EXPERIMENTS

In order to extract the maximum average power from a two terminal circuit one is faced with the problem of finding the optimal load impedance. The power delivered to the load

Table 5: Estimated wind tunnel RPM to wind velocity conversion

Hz	mph	fps	m/s	Hz	mph	fps	m/s	Hz	mph	fps	m/s
20	11.77	17.24	5.25	34	21.03	30.80	9.39	48	30.30	44.37	13.52
21	12.43	18.21	5.55	35	21.69	31.77	9.68	49	30.96	45.34	13.82
22	13.09	19.18	5.84	36	22.35	32.74	9.98	50	31.62	46.31	14.12
23	13.75	20.15	6.14	37	23.02	33.71	10.28	51	32.28	47.28	14.41
24	14.41	21.12	6.44	38	23.67	34.68	10.57	52	32.94	48.24	14.71
25	15.08	22.08	6.73	39	24.24	35.65	10.87	53	33.60	49.21	15.00
26	15.74	23.05	7.03	40	25.00	36.62	11.16	54	34.27	50.18	15.30
27	16.40	24.02	7.32	41	25.66	37.59	11.46	55	34.93	51.15	15.60
28	17.06	25.00	7.62	42	26.33	38.56	11.75	56	35.59	52.12	15.89
29	17.72	25.96	7.91	43	26.99	39.52	12.05	57	36.25	53.09	16.18
30	18.38	26.93	8.21	44	27.65	40.49	12.34	58	36.91	54.06	16.48
31	19.05	27.90	8.50	45	28.31	41.46	12.64	59	37.57	55.03	16.77
32	19.71	28.87	8.80	46	28.97	42.43	12.93	60	38.24	56.00	17.07
33	20.37	29.84	9.09	47	29.63	43.40	13.23				

depends on the load impedance: a short-circuit load receives no power because the voltage across it is zero; an open-circuit load receives no power because the current through it is zero [38]. Therefore, a power versus load curve will resemble a half sine wave, with the location of the peak representing the best load resistance for maximum average power extraction. However, it should be noted this is not necessarily the load resistance that will provide the most efficient power extraction. To gain an understanding of the power versus load curve for the MiniHornet, experiments at varied wind velocities are performed as follows:

Table 6: MiniHornet power vs load & velocity experiment equipment

Name	model #	serial #
Engineering Laboratory Design, Inc. wind tunnel	400	64709
Hewlett Packard multimeter	34401A	US36018431
A-Tek protoboard	B-124	N/A
National Instruments Ni-daq card	NI-USB 6008	1261417
Matlab software	R2009b	N/A

A Matlab m-file (provided in the appendix, as with all subsequent Matlab m-files) is written to acquire, save, and manipulate the voltage data provided by the four EMI generators. The code allows the user to take data, at a set load resistance, for varied flow velocities, of the four voltage channels, which correspond to the four solenoids/EMI generators of the MiniHornet as shown in Figure 44. The code saves the voltage data, manipulates it as was seen in Equation 5.1, and saves the new power data. The user may then change the resistance value and repeat. To change the load resistance value for each of the four solenoids, four decade boxes are made from potentiometers with increasing resistance ranges; 100, 1000, 5000, and $50,000\ \Omega$ potentiometers are connected in series on the A-Tek protoboard, as in Figure 45. The code finally plots the data both as a surface plot for each solenoid and as 2D line plots of power versus $1/R$, at each flow velocity.

The procedure for the experiment are as follows:

1. Place the MiniHornet in the wind tunnel in the wanted configuration.
2. Connect decade boxes to Ni-daq card and connect daq card to computer USB port.
3. Run Matlab m-file.
4. Attach multimeter and adjust each decade box's resistance to desired value. Disconnect multimeter.
5. Connect each of the four solenoids to their respective decade boxes.
6. Input resistance value into Matlab.
7. Adjust wind tunnel to desired flow velocity.
8. Connect each of the four solenoids to their respective decade boxes.

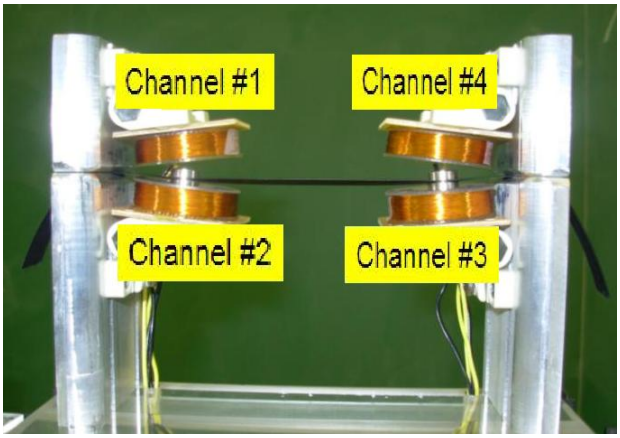

Figure 44: MiniHornet power vs. load resistance & velocity measured solenoids; relating the MiniHornet's solenoids to the voltage channels measured by Matlab (looking at the front of the MiniHornet)

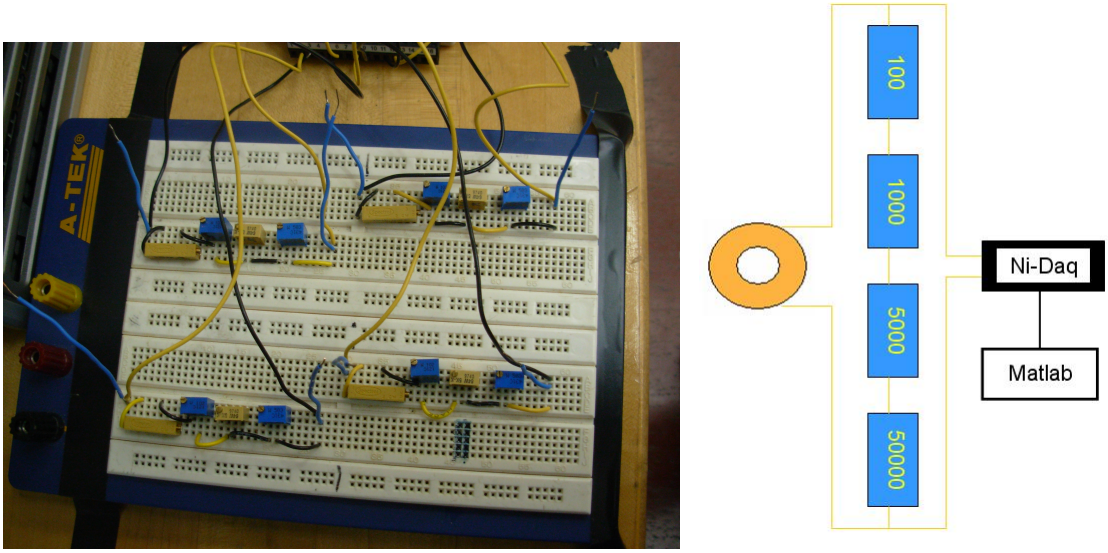

(a) picture (b) diagram

Figure 45: Decade boxes for MiniHornet power vs. load & wind velocity experiments

9. Input the RPM value into Matlab.
10. Wait as Matlab acquires the data.
11. Repeat steps 7-10 for all desired flow velocities: 22.34, 25.00, 27.05, 30.30, 32.94, 35.59, and 38.24 mph.
12. Repeat steps 4-11 for all desired resistance values: 1, 1.5, 2, 4, 7, 10, 15, 20, 40, 70, 100, 150, 200, 400, 700, 1000, 1500, 2000, 4000, 7000, 10000 Ω.

Results: Surface plots and 2D-plots of the results are seen in Figures 46 and 47, respectively. As expected the curves resemble a half sine wave. From the figures it can be seen that the maximum power output occurs at a load resistance near 400 Ω for all four solenoids. Obvious from the figures is how power output increases with increasing flow velocity. This makes intuitive sense since the wind flow contains more energy at a higher velocity. These results show that an optimum load resistance range may be found for future optimization and different device configurations.

6.3.2 FREQUENCY RESPONSE FUNCTION EXPERIMENTS

A transfer function is the mathematical representation of the relationship of a linear time-invariant system's output over its input. The frequency response function (FRF) is the transfer function evaluated in the frequency domain (s evaluated at $j\omega$) and it expresses the structural response of the system to an applied force. Typically the purpose of such vibration analysis is to identify the natural frequencies, damping ratios, and mode shapes of a structure [44].

To better understand the vibration analysis of the MiniHornet, most specifically its natural frequencies, experiments are performed to solve for its FRF. Matlab's vibration toolbox is utilized in conjunction with a SigLab interface to output a random signal/force (white noise) into the MiniHornet's EMI generators (motors in this case), input the response of the system at the center of MiniHornet's belt (measured by a laser Doppler vibrometer (LDV)), and analyze for the FRF and phase angle as a function of frequency. The experiment is performed three times to measure the excitation of the belt at three total locations.

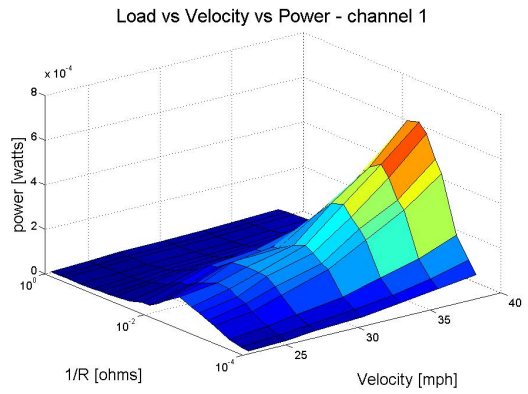

(a) Channel #1

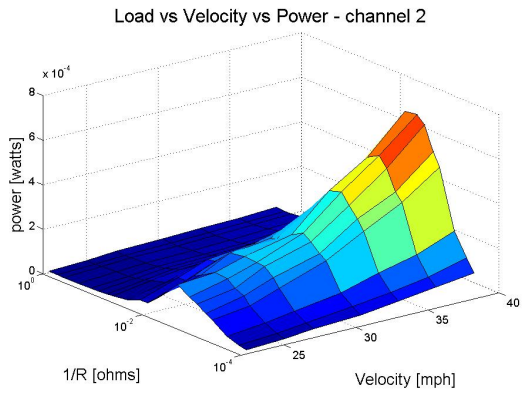

(b) Channel #2

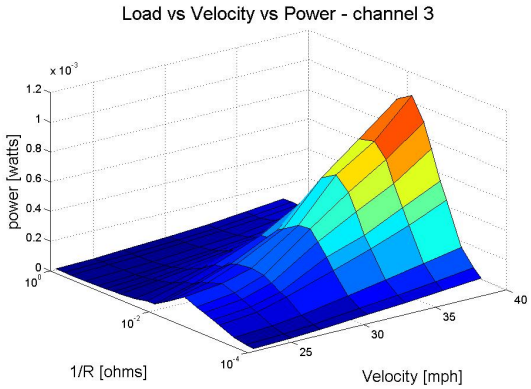

(c) Channel #3

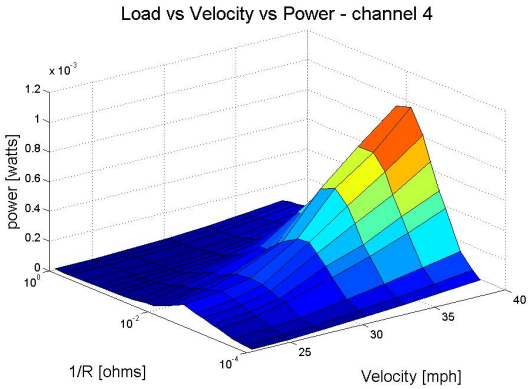

(d) Channel #4

Figure 46: MiniHornet power vs. load resistance & flow velocity experiment results; surface plots

The procedure for the experiment is as follows:

1. Wire the four EMI generators/motors of the MiniHornet together in parallel and connect to the SigLab interface's output. The EMI generators (motors in this case) are wired to insure they excite the belt in unison symmetrically. Therefore for each side pair of solenoids (1 & 2 and 3 & 4, as in previous experiment) when the bottom solenoid pushes on the magnets the top solenoid simultaneously pulls on them.
2. Set LDV's low pass (LP) filter output module to 5K and its decoder module to 5mm/s/V.

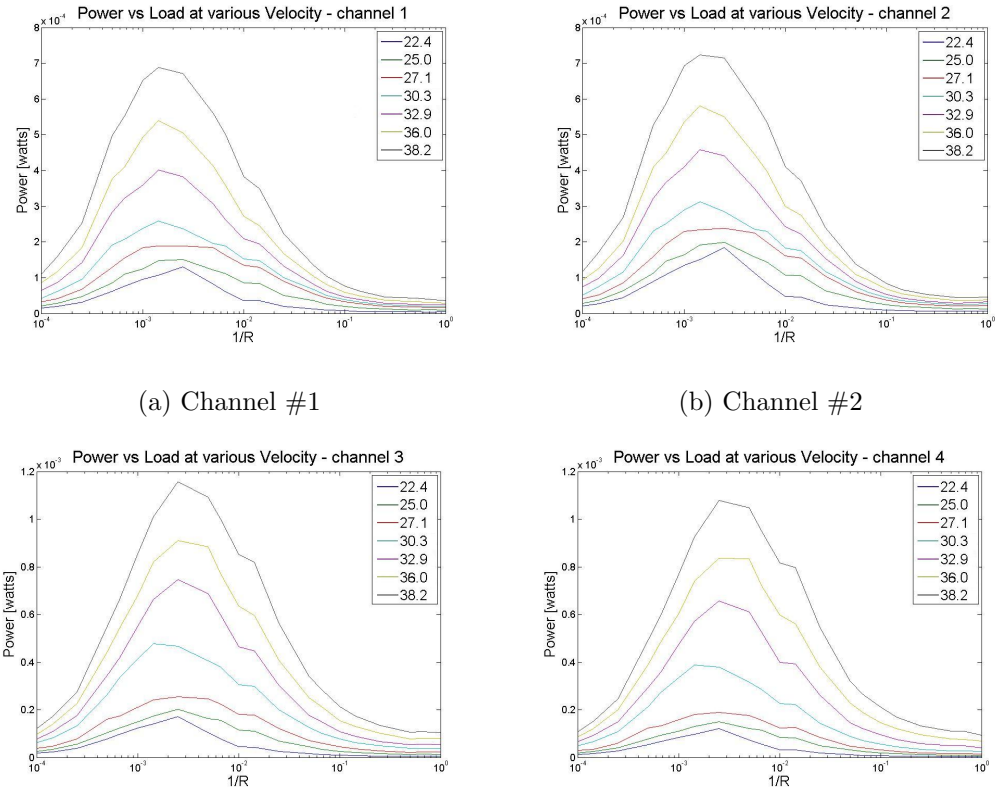

(a) Channel #1

(b) Channel #2

(c) Channel #3

(d) Channel #4

Figure 47: MiniHornet power vs. load resistance & flow velocity experiment results; 2D-plots

Table 7: MiniHornet frequency response function experiments equipment

Name	model #	serial #
Polytec laser Doppler vibrometer	CLV 1000	5040211
DSP Technology, Inc. SigLab Interface	20-42	11305
a protoboard	N/A	N/A

3. Run Matlab m-file.
4. Connect the LDV's output to SigLab's input.
5. Place the MiniHornet into an enclosure (eliminate ambient air movement).

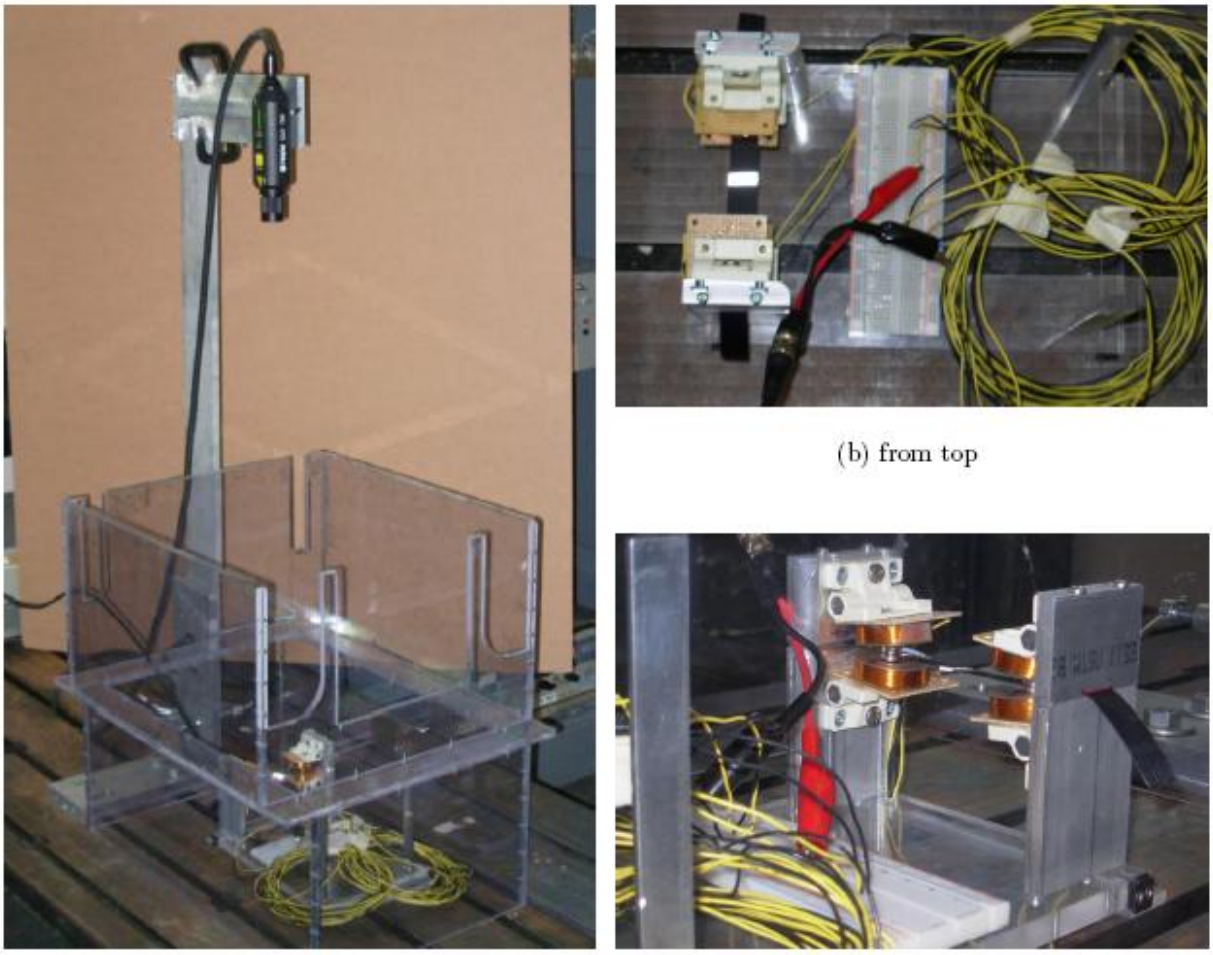

(a) total setup

(b) from top

(c) from side

Figure 48: MiniHornet frequency response function experimental setup

6. Set Matlab's vibration toolbox to input a random signal at a 0.2 V root mean squared value for a 100 Hz bandwidth with a sampling rate of 256 Hz, for a record length of 4096 data points; setting the sampling to average over 10 samples without overlap.
7. Mount the LDV 36" (0.914 m) above the belt and aim directly down onto the reflective tape at the front leading edge of the belt (Location 1); mounted with a rigid metal structure that is mounted to the lab table.
8. Run the set toolbox program.

9. Repeat steps 7 & 8 for the addition locations: Location 2, being the center of the belt directly in the middle between the front leading edge and the back trailing edge; Location 3, being the center of the belt on the back trailing edge, as viewable in Figure 49

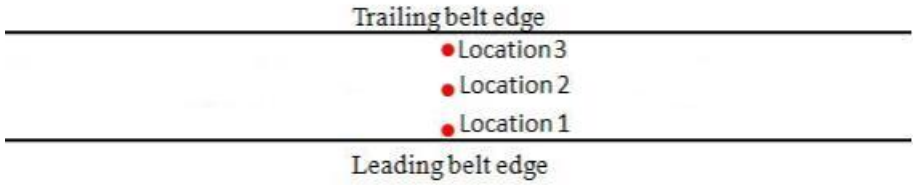

Figure 49: MiniHornet laser Doppler vibrometer measurement locations

Results: The frequency response functions and phase diagrams of the response are seen in Figure 50. Noticeable is how nearly identical the plots are at each location. However, the magnitude increases from the front edge of the belt (Location 1) to the trailing edge (Location 3). The MiniHornet's configuration itself may provide reasoning for this increase in magnitude. As explained at the end of the MiniHornet Construction section (5.1) the MiniHornet's belt is configured to hold the belt in a state with the front leading edge of the belt slightly more taunt than the back trailing edge. Therefore, the lower tension seems to provide an increase in the belt's possible excitation amplitude, however it is an intuitive belief there is a limit to this relation before the belt's tension becomes too loose for optimal energy harvesting.

These figures also give insight into the dynamics of this static system (not excited by fluid flow). Looking at the FRF plots, there are peaks in the response at approximately 47 Hz and 66 Hz. These peaks correspond to the natural frequencies of the system and accordingly poles in the phase angle plots. Since natural frequencies relate to the mass and spring constants of a system (modeled with a mass connected to a linear and torsional spring similar to the typical section airfoil model, as was seen in Figure 16), as was in Equation 4.2, knowing the mass of the system one may solve for its spring constants. This further shows dynamic characteristics of an AIEH may be found to populate a simulation model of a LCO. Since altering the belt's configuration (length, tension, mass distribution, ETC.) changes

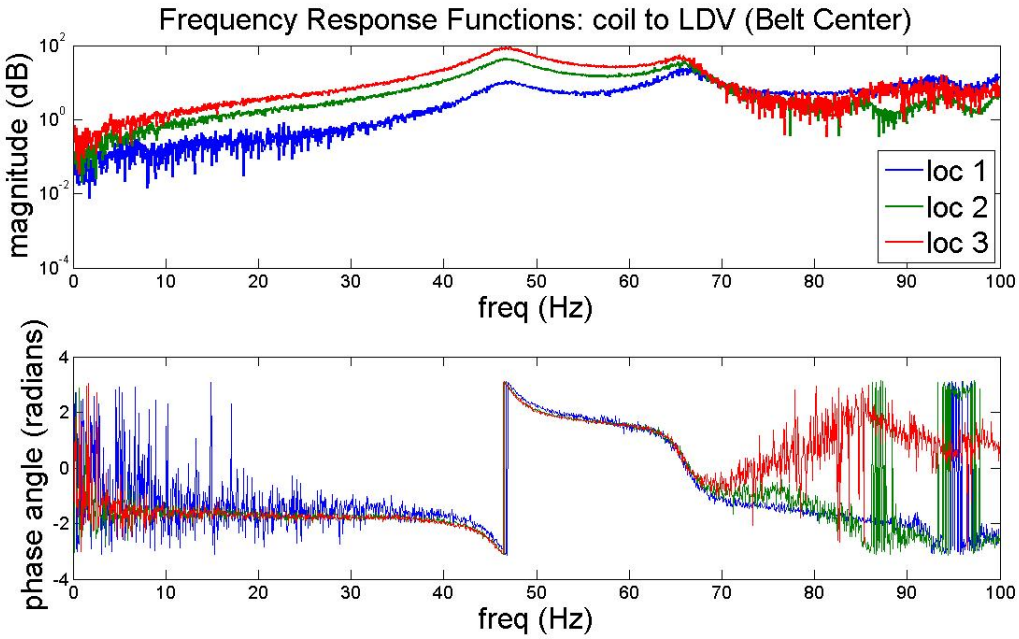

Figure 50: MiniHornet frequency response function experiment results; loc 1, loc 2 , and loc 3 correspond to location 1, location2, and location 3, respectively

its dynamic characteristics, if one wishes to accurately simulate the LCO experienced by AIEHs one must be capable of acquiring experimental data to populate as well as validate the model.

6.4 BLUFF BODY WIND TUNNEL EXPERIMENTS

Described in section (3.2), bluff bodies shed alternating vortices off their trailing edge in laminar uniform flow. Again, for circular cross-sectional bluff bodies, the diameter of the bluff body, the velocity of the fluid flow, and the frequency of vortex shedding are related via the Strouhal number (Equation 3.4). Understanding this relation proposes the potentiality of utilizing a bluff body to increase the amplitude of excitation of an AIEH.

6.4.1 POWER SPECTRAL DENSITY OF SYSTEM

To accomplish an increase in excitation amplitude for the MiniHornet we must first understand its response at varied flow velocities. One achieves this by taking the power spectral density (PSD) of the MiniHornet's excitation without the presence of a bluff body. An application of the fast Fourier transform (FFT), a PSD analysis derives a power spectrum of the power output of an electrical system and is a function of frequency. The power spectrum being the associated magnitude of power for each frequency component. Therefore, a display of a PSD is a plot of power versus frequency [30].

At one of the known velocities, with PSD plots for the MiniHornet, in theory, we can choose a vibration frequency at which a peak in the power spectrum occurs and use the Strouhal number relation to solve for the necessary bluff body circular diameter to shed vortices at the same chosen vibration frequency. Therefore, it is the belief that an increase in the magnitude of power of the MiniHornet at the chosen frequency can be accomplished by placing a circular bluff body, with the computed required diameter, in front of the MiniHornet and driving the wind tunnel at the specified flow velocity. In order to accomplish this goal we must first understand the response of the MiniHornet without a bluff body present. The equipment utilized for this experiment are as follows:

Table 8: Equipment for MiniHornet power spectral density experiments

Name	model #	serial #
Engineering Laboratory Design, Inc. wind tunnel	400	64709
National Instruments Ni-daq card	NI-USB 6008	1261417
Matlab software	R2009b	N/A

Similar to the power versus load resistance and flow velocity experiments, a Matlab code is written to acquire voltage data from the solenoids (only two channels are utilized this time, as seen in Figure 51), save the data, manipulate the data for the PSD, and plot the PSD for each channel measured.

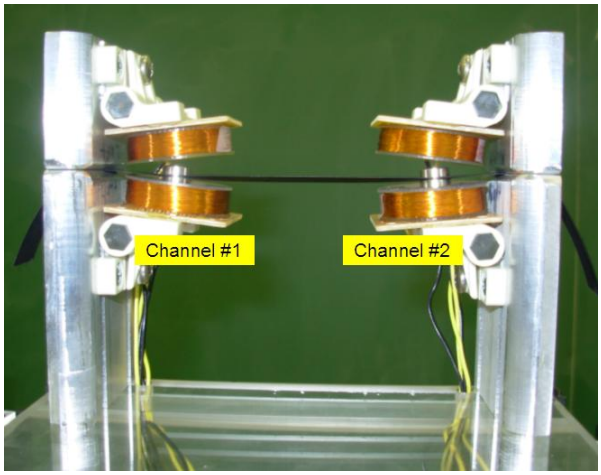

Figure 51: MiniHornet power spectral density measured solenoids; relating the MiniHornet's solenoids to the voltage channels measured by Matlab (looking at the front of the MiniHornet)

The procedure for the experiment are as follows:

1. Place the MiniHornet in the wind tunnel.
2. Connect solenoids to the Ni-daq card and connect daq card to computer USB port.
3. Run Matlab m-file.
4. Adjust wind tunnel to desired fan RPM (remember the fan RPM relates to the wind velocity as in Table 5).
5. Input the RPM's corresponding velocity value into Matlab.
6. Wait as Matlab acquires the data.
7. Repeat steps 4-6 for all desired RPM values; from $20 - 60$ Hz in increments of 1.

Results: Figure 52 gives the PSD results as a waterfall plot. The plot relates the PSD to flow velocity and frequency via color (increased power magnitude represented with a deepening of color). One may notice the deepening of color that gradually coalesces into a deep red streak, in the upper left section of the plot. It is the belief the streak may correspond to an attained stable LCO. Hence, the MiniHornet may be reaching resonance in a flow velocity around 30 mph. Though 30 mph is unrealistic as an operating speed, it should be remembered that with a set Reynolds number, if you decrease the flow region by half, you must double the

flow velocity. Therefore, other AIEH configurations may be produced to reach resonance at a much lower wind velocity.

Plots of the PSDs are seen in Figure 53 and Figure 54 for flow velocity ranges from 11.77 - 24.24 mph and 25.00 - 38.24 mph, respectively. One may notice that for each subfigure, the top and bottom plots, which respectively correspond to the left and right measured solenoids on the MiniHornet, are nearly identical. This suggests that the belt is excited symmetrically. One may also notice by the third subfigure, at a wind tunnel fan speed of 32 Hz (8.80 m/s or 19.71 mph), saturation seems to be possibly occurring. However, subfigures (a), (b), and (c) of Figure 53 contain "nice" peaks that may be targeted in an attempt to increase their magnitude with forced excitation due to a bluff body.

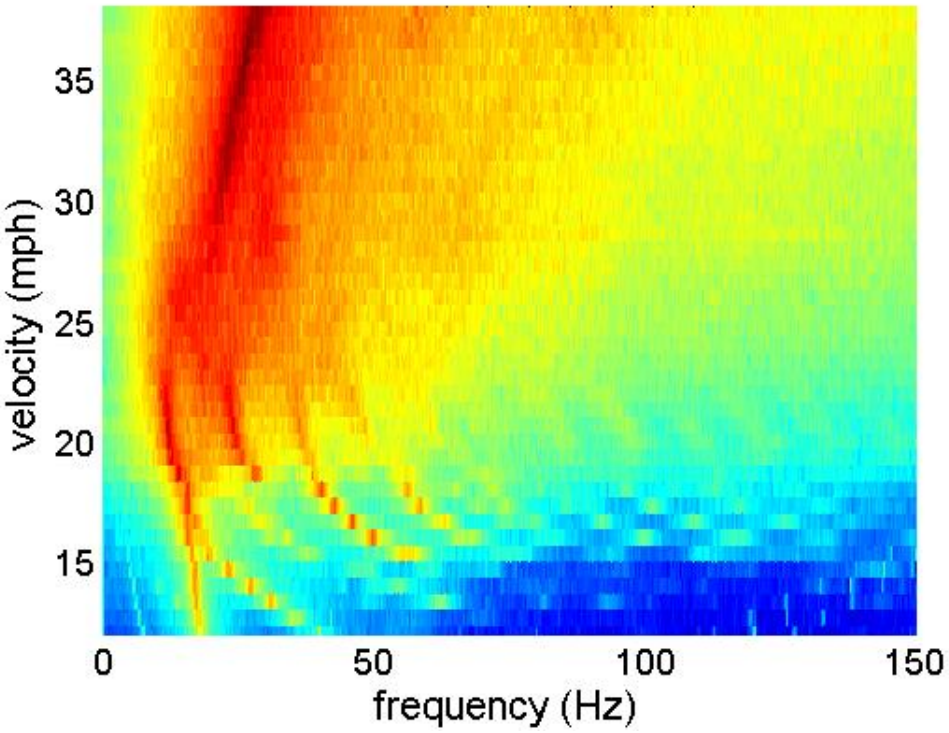

Figure 52: MiniHornet PSD waterfall plot; natural response without the presence of a bluff body

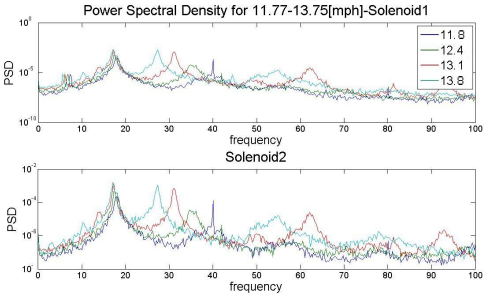

(a) 20-23Hz

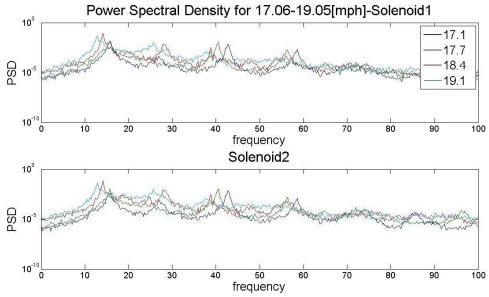

(b) 28-31Hz

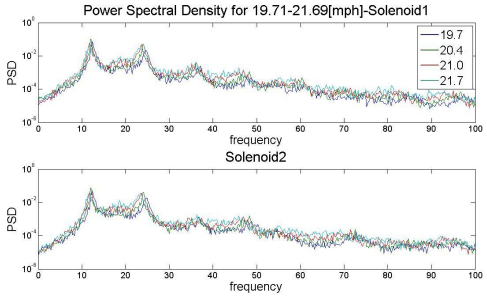

(c) 32-35Hz

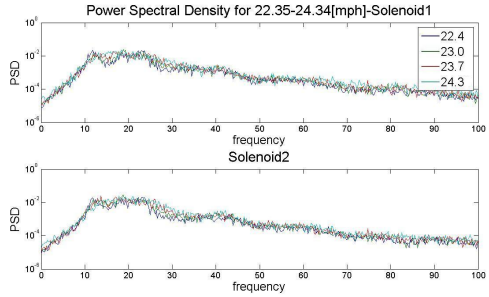

(d) 36-39Hz

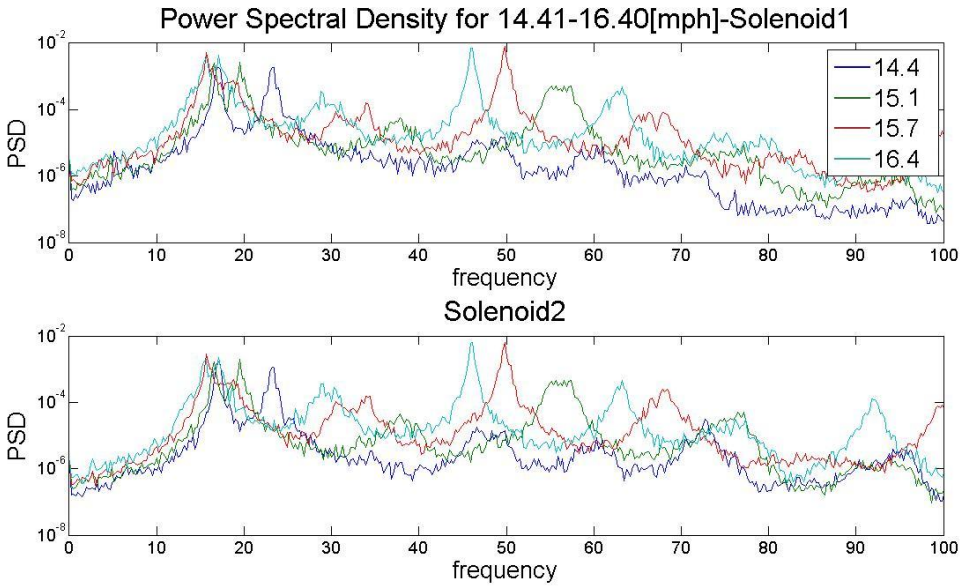

(e) 24-27Hz

Figure 53: MiniHornet no bluff body PSDs; 11.77 - 24.24 mph (as specified by the corresponding wind tunnel fan RPM

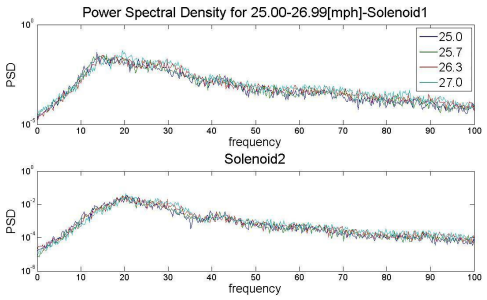

(a) 40-43Hz

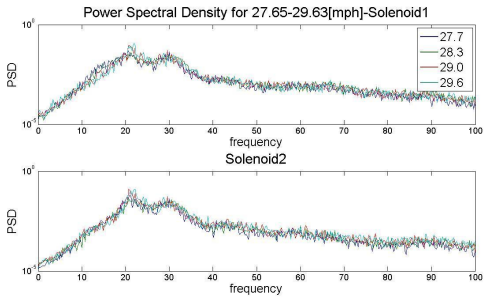

(b) 44-47Hz

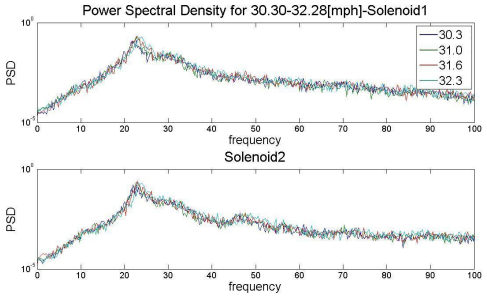

(c) 48-51Hz

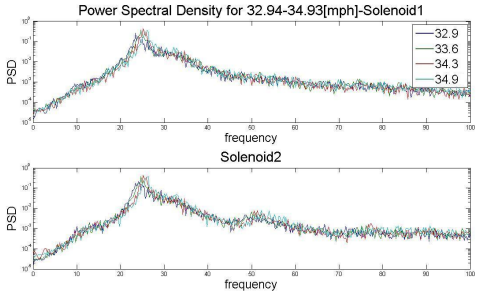

(d) 52-55Hz

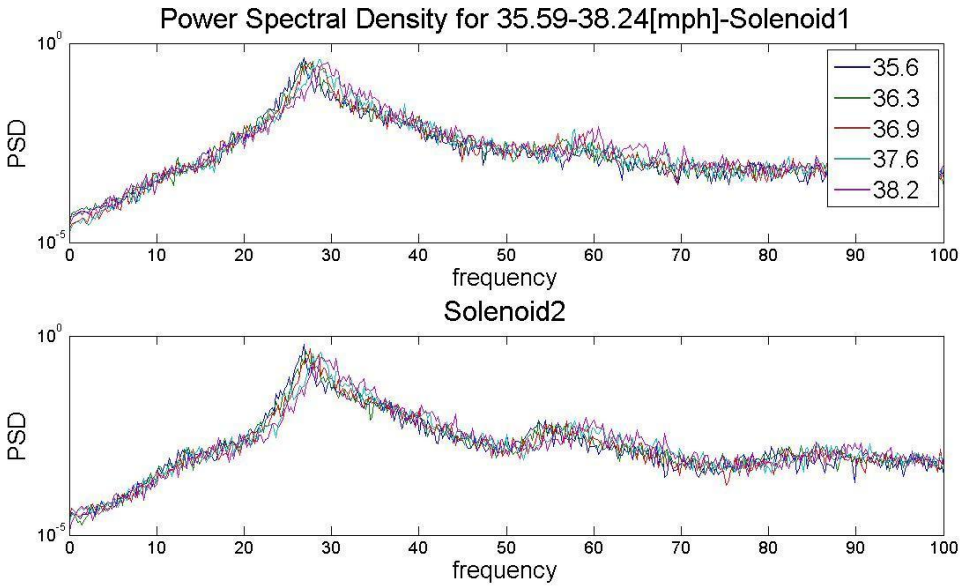

(e) 56-60Hz

Figure 54: MiniHornet no bluff body PSDs; 25.00 - 38.24 mph (as specified by the corresponding wind tunnel fan RPM

6.4.2 STROUHAL NUMBER FREQUENCY MATCHING

Now that nice peaks of the PSD without a bluff body have been acquired one must determine which peaks may be targeted within the realm of the experimental setup. Considering the limited experimental work space, 6" x 6" (15.2 cm) wind tunnel, there is a maximum usable diameter size of a circular bluff body before adverse effects, due to the bluff body, may occur to the flow. To determine which peaks may be targeted a waterfall plot of the previously taken PSD, with no bluff body present, is produced with a line that corresponds to a bluff body diameter of 2" (5.08 cm), which is intuitively believed to be the maximum. The line is produced in Matlab by finding the corresponding range of vortex shedding frequencies for the measured velocity range (11.77 – 38.24 mph; 5.26 – 17.09 m/s), at a specified diameter: first the range of Reynolds numbers is found using Equation 3.6; next a range of Strouhal numbers is found using Equation 3.7; lastly the corresponding vortex shedding frequency range is found using Equation 3.4 for a set diameter. Accordingly, any peak of the PSD the line passes over, in Figure 55, may potentially be targeted with a 2" (5.08 cm) diameter bluff body. Regretfully, everything to the left of the line requires a bluff body diameter larger than 2" (5.08 cm). Since only peaks seen on the right side of the line may be targeted, the circle on the figure denotes the chosen section of the PSD that contains the only peaks to possibly target.

Figure 56 shows the chosen peaks (shown by arrows that point at the peak) that are within the circular region of the previous figure. The peaks' wind tunnel fan rotational frequencies (equivalent flow velocity) and corresponding frequencies are as follows in Table 9.

Table 9: Corresponding bluff body diameters of chosen MiniHornet PSD peaks; these bluff bodies may increase the magnitude of power of the AIEH at these chosen peaks of the PSD.

fan RPM frequency	equivalent flow velocity	frequency	bluff body diameter
26 Hz	15.74 mph (7.03 m/s/23.1 fps)	46 Hz	1.4633" (3.7169 cm)
27 Hz	16.40 mph (7.32 m/s/24.0 fps)	47 Hz	1.6580" (4.2112 cm)
29 Hz	17.72 mph (7.91 m/s/26.0 fps)	56 Hz	1.4726" (3.7400 cm)

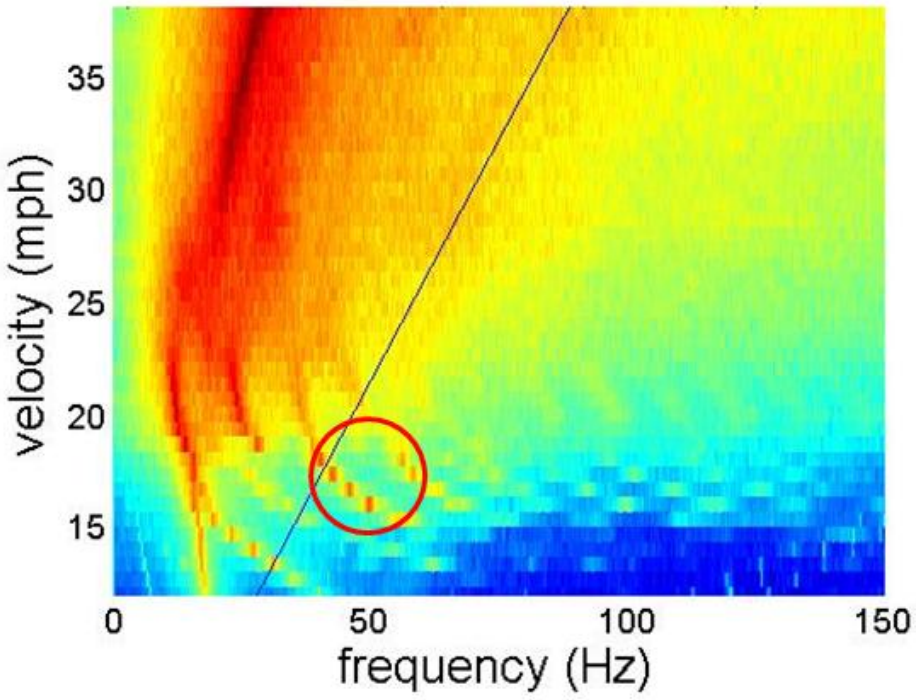

Figure 55: MiniHornet Strouhal matching target region; previous PSD without a bluff body, with relations of possible regions to target with a bluff body (represented by the diagonal line) and the actual chosen target region (represented by the circle)

The corresponding bluff body diameter, D, is solved for, as in Equation 6.1, by manipulating Equation 3.7, Equation 3.6, and Equation 3.4, where $\upsilon_{air} = 15.11 \times 10^{-6}$ m^2/s at 70°F.

$$D = \frac{\left(0.2684 - 1.0356\sqrt{\frac{\upsilon_{air}}{U\delta}}\right) U}{F_s} \simeq \frac{0.2684U}{F_s} \tag{6.1}$$

The circular bluff bodies are made out of aluminum rods that are machined on a lathe. After the bluff bodies are machined their actual diameters are measured to be 1.461" (3.711 cm), 1.657" (4.209 cm), and 1.472" (3.739 cm), as they relate to bluff bodies #1, #2, and #3, respectively. Support structures are made out of 3/4" diameter 6061 aluminum rods. These rods are planed down to perfect half circles so the flat part of the rod my face outwards when in the wind tunnel, therefore the flow is subjected to a round object, which is slightly less

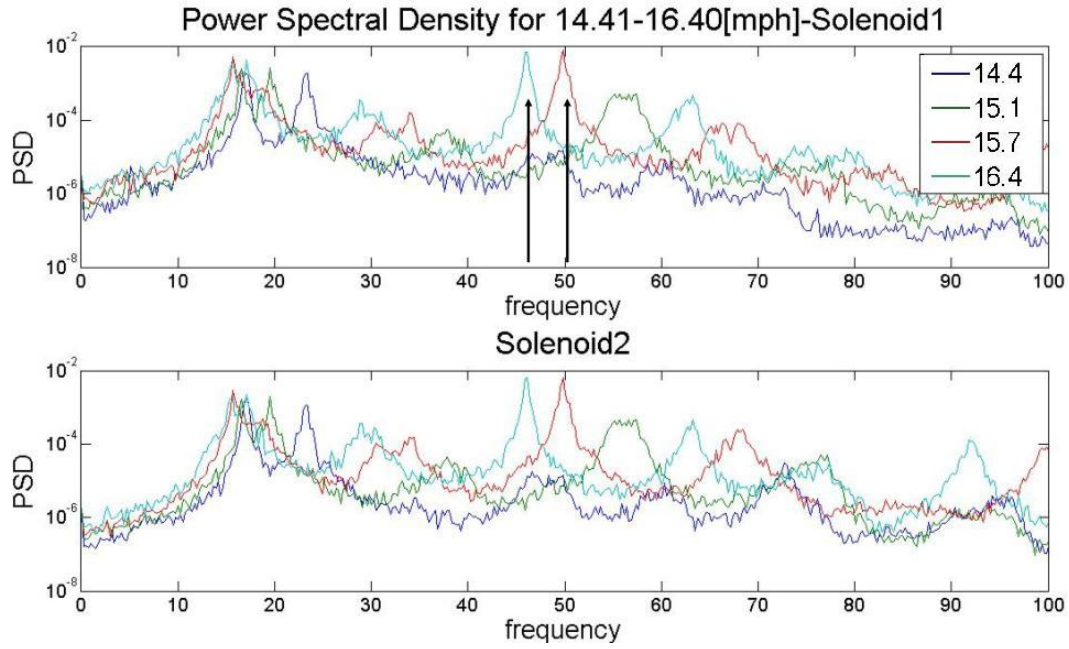

(a) for first two bluffs

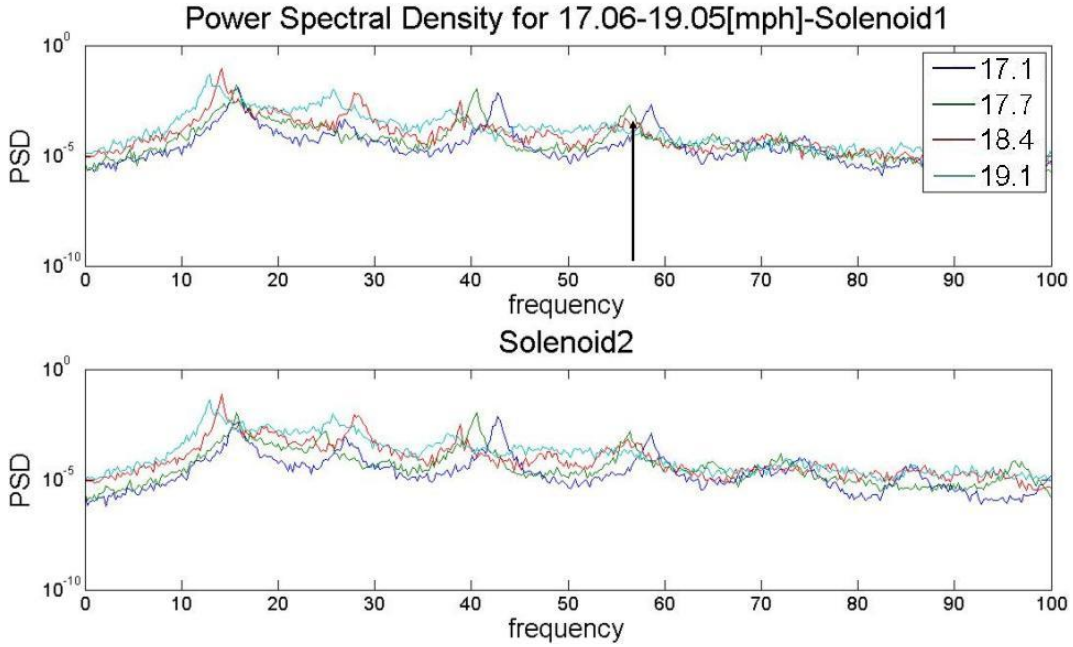

(b) for third bluff

Figure 56: MiniHornet targeted PSD peaks; for bluff body excitation experiments

intrusive. The round faces of the structure are also slightly planed to provide a nice platform to machine out a L-slot in each structure. These slots allow the ends of the bluff body rods to be machined down to pegs that can slide into the L-slots locking it in place directly in front of the path of the MiniHornet's belt. Two 6-32 screw holes are tapped in the bottom of the support structure to allow them to be mounted to the same cast acrylic floor panel the MiniHornet's support structures are mounted. A depiction of the entire setup can be seen in Figure 57.

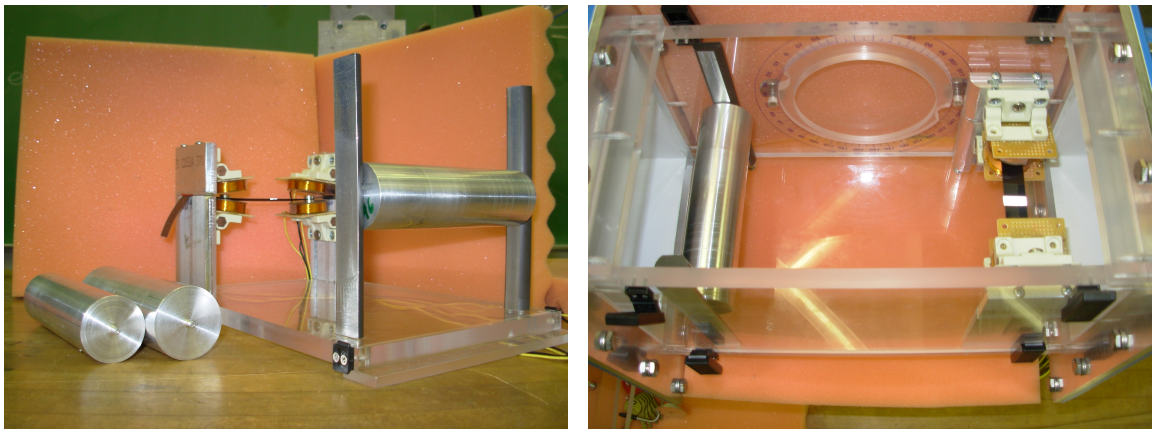

(a) outside wind tunnel

(b) inside wind tunnel

Figure 57: MiniHornet bluff body experiment setup.

A similar Matlab code to the previous PSD experiment without a bluff body is utilized for these experiments; measuring the same solenoids. The equipment utilized for this set of experiments is again noted in Table 8. The procedure for the experiments are as follows:

1. Place the MiniHornet in the wind tunnel with a bluff body present.
2. Connect solenoids to the Ni-daq card and connect daq card to computer USB port.
3. Run Matlab m-file.
4. Adjust wind tunnel to desired fan RPM (remember the fan RPM relates to the wind velocity as in Table 5.
5. Input the RPM's corresponding velocity value into Matlab.
6. Wait as Matlab acquires the data.
7. Repeat steps 4-6 for all desired RPM values: from $20 - 60$ Hz in increments of 1.

8. Remove MiniHornet setup and replace bluff body with next bluff body.
9. Repeat steps 1-8 until all bluff bodies have been tested.

Results: Figure 58 shows the targeted peaks (represented by a black arrow) of the previous experiment with no bluff body versus the PSD results with the corresponding required bluff body; with machined diameter, at chosen wind velocity. One can see that the effort to target a specific peak to enhance the power output at that specific frequency is unsuccessful. However when comparing the no bluff body waterfall plots to the waterfall plots with the three bluff bodies, as in Figure 59, one can notice the addition of a distinct linear region. This linear region, therefore, must correspond to the forced excitation caused by the vortices shedding from the bluff body and is linear since the Strouhal number remains constant; with a constant diameter, if the Strouhal number remains constant, with an increase in wind velocity, the frequency of vortex shedding must appropriately increase. Consequently this proves that an AIEH will have an enhancement in performance due to forced excitation of a circular bluff body and since the Strouhal relation has been shown to hold true for non-circular bluff bodies [51], it is conceivable that rod-type bluff bodies of all shapes and sizes may enhance the performance of an AIEH.

An imposing question that arises with these results, however, is how far the linear forced excitation region is from both the line corresponding to a Strouhal number for a 2" (5.08 cm) diameter bluff body and from the MiniHornet's natural region of excitation, particularly the region of resonance. It is a belief that the bluff body constrained the flow through the test section, making the actual flow velocity less than what was input into Matlab. This potentially skewed the region of forced excitation vertically away from the line corresponding to the 2" (5.08 cm) diameter bluff body. To harvest the most power an AIEH would want the forced excitation region to coalesce with the excitation region of resonance. In a case where the bluff body would not change in size, therefore having a constant Strouhal relation, the dynamic characteristic of the AIEH would need to be altered so its natural region of resonance would lie on the line of forced excitation. Assuming the system acts similarly to a vibrating string increasing the tension of the belt would increase its natural frequency; in the MiniHornet's case, pushing the region of natural excitation to the right. It should be realized however, that increasing the tension on the belt would decrease the LCO's ampli-

tude, potentially decreasing power output, and may increase the AIEH's cut in speed; an optimization is necessary. Conversely increasing the belt length/mass would decrease the natural frequency, pushing the natural region of excitation to the left. Therefore in the MiniHornet's case, its region of natural resonance, may potential be moved to lie on the region of forced excitation if its tension was increased, maintaining the belt length, and the mass of the belt was decreased.

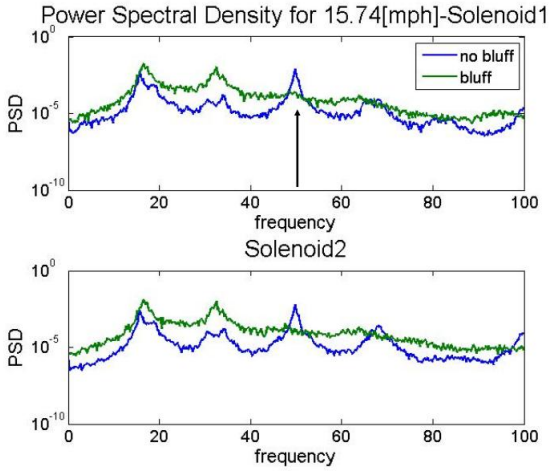

(a) bluff #1 $D = 1.461$" (3.711 cm)

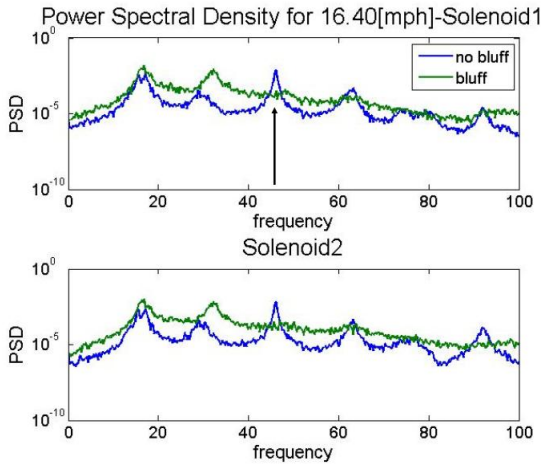

(b) bluff #2 $D = 1.657$" (4.209 cm)

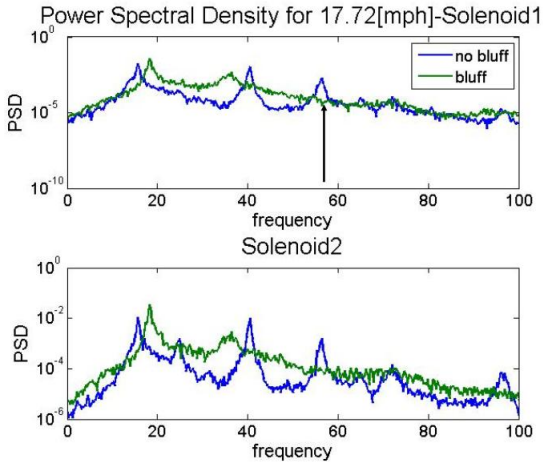

(c) bluff #3 $D = 1.472$" (3.739 cm)

Figure 58: MiniHornet bluff body vs. no bluff body PSD plots

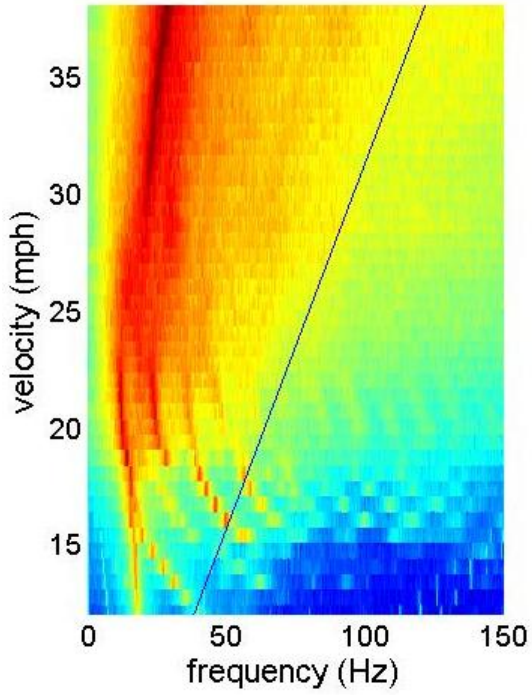

(a) no bluff body

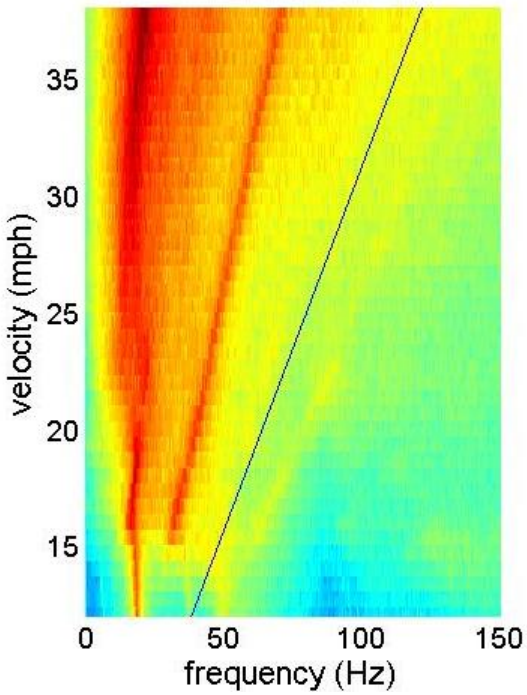

(b) bluff #1 $D = 1.461$" (3.711 cm)

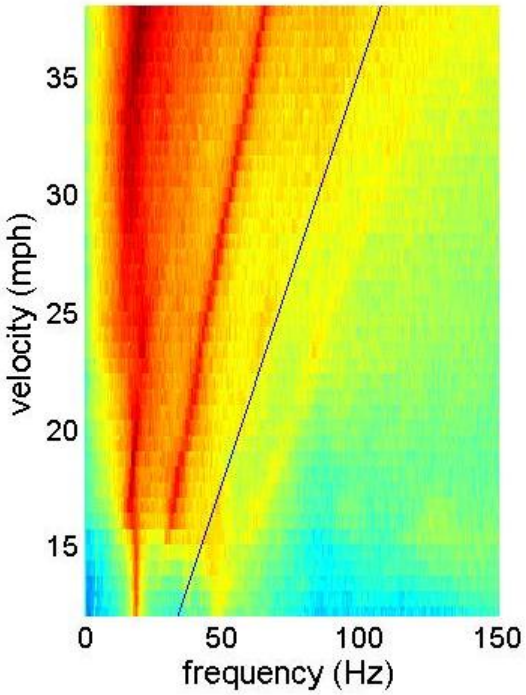

(c) bluff #2 $D = 1.657$" (4.209 cm)

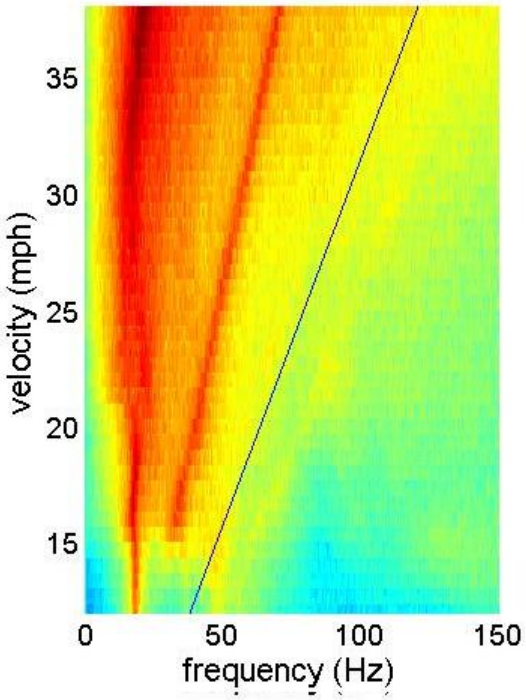

(d) bluff #3 $D = 1.472$" (3.739 cm)

Figure 59: MiniHornet bluff body vs. no bluff body waterfall plots

7.0 CONCLUSIONS AND FUTURE RECOMMENDATIONS

7.1 SUMMARY

It was the intent of this thesis work to gain a better understanding of aeroelastic instability energy harvesters (AIEHs) in a number of different ways:

1. Efforts to characterize the limit-cycle oscillation (LCO) experienced by an AIEH are conducted.

2. A previous senior design team's results showed AIEHs to be a a compact, modular, cost-effective wind energy harvesting technology capable of producing a "meaningful" amount of power (70 mW) in sub-Class 1 (at ≈5 mph) wind resource regions. Validation of these results is wished to be ascertained.

3. AIEHs have shown to have a potential enhancement in power production due to erratic flow conditions caused by the presence of bluff bodies, resulting in a forced excitation of an aeroelastic instability. Validation and characterization of this phenomenon is wished to be attained.

The results of the experiments for both the AIEHs designed and developed for this thesis is seen in Table 10

Table 10: Summary of experimental results for both developed AIEHs; the Hornet and the MiniHornet

The Hornet	
Experiment	Results
initial change of length	nearly 3.5 mW power
EMI generator redesign	nearly 30 mW power
tensioner implementation	48.3 mW power; validating senior design team
The MiniHornet	
Experiment	Results
power vs. load & velocity	optimum load of 400 Ω; characterization possible
frequency response function (FRF)	ω_n at ≈47 Hz & 66 Hz; characterization possible
power spectral density (PSD)	resonance reached at 30 mph
Strouhal frequency matching	forced excitation due to circular bluff body possible

7.2 CONCLUSIONS & FUTURE RECOMMENDATIONS

7.2.1 AIEH LCO CHARACTERIZATION

The future development of AIEHs will be dependent on the ability to populate simulations and characterize specific configurations. It was shown that in a controlled environment (i.e. a wind tunnel) good experimental results of the system's dynamic characteristics, such as those attained in the Power Versus Load & Velocity (5.3.1) and FRF (5.3.2) sections, may be acquired. In the future, results such as these may be utilized to populate computer simulations attempting to model the behavior of a specific AIEH, which is dependent on that specific AIEH's physical and power generation characteristics. Under similar controlled conditions other AIEH configurations could also be used to populate and help develop the simulation model.

Future Recommendations: Innovation of an AIEH LCO model is a must to achieve its full potential and provide an avenue for AIEHs to be designed for specific applications. The design and dynamical characteristics of any AIEH device directly affect its response and performance. The development of new techniques is necessary to properly analyze and predict the LCO behavior and how load resistance affects the power generation.

Analyzing the motion of an AIEH is difficult due to the non-linear fluid-dynamics and its feedback interaction with the AIEH structure. It may be accomplished by using numerical simulations to estimate the amplitude of the LCO and the method of describing functions, which have met with particular success for multimode flutter instability studies [58, 37].

Such an analysis could give the characteristics of the LCO, including amplitude and frequency, the characteristics of power, and how electrical load affects the device's performance. Since the typical flow conditions of any future AIEH installations will be easily obtained, it may provide the computational tools to design the optimal AIEH for a specific application.

7.2.2 POWER DENSITY VALIDATION

The results of this study demonstrates the potential of the an AIEH to be capable of generating meaningful power output in sub-Class 1 wind flow. A couple key elements were required, however, to attain this power density:

1. The height of the solenoids used in the electromagnetic induction (EMI) generators needed to made to the same height as the magnets that plunge into the generators. An order of magnitude in power production was attained after the Hornet's EMI generators' were redesigned and fabricated to have the same height as the rare earth magnets.
2. A tension gradient from the front leading edge of the belt to the trailing edge of the belt (slightly more taut on the front edge) has proven to provide a huge boost in the AIEHs excitation, and appropriately the power generation. More than a 200% increase in power production was attained after the belt tension distribution alternators were designed and installed on the Hornet; in the non-bluff body case. It is believed this tension gradient may allow the plunge and twist modes of the AIEH's multimode flutter excitation to coalesce.

Future Recommendations: Quantification of the effects the tension distribution has on the physical characteristics of the AIEH would only enhance the accuracy of the aforementioned simulation model, which would allow this phenomenon to be utilized to increase the AIEH's potential power generation. It would also allow it to be better designed for a specific installation site.

Currently the chosen medium for the conversion of the mechanical energy to electrical energy is electromagnetic induction, which utilizes rare earth magnets. The current design only allows for these magnets to partial plunge in the EMI generators' solenoids, however, it has been shown [23] that the most power is generated when the magnets of the generator fully traverse the solenoid. Therefore, this design is not using the full potential of an electromagnetic induction generator. It has been shown [53] an electrostatic induction method is preferable over an electro-magnetic induction method for small-scale applications because it is more suited to high-impedance circuits. Furthermore, it would replace the use of rare earth magnets with an electret (a stable dielectric material with a permanently-embedded static electric charge often made of a plastic or wax), effectively eliminating the mass of the magnets, which dominate the system's response. This may allow for implementation of additional generators, vastly boosting the power density. Therefore, investigation of various mediums and configurations for the mechanical to electrical energy conversion should be conducted.

7.2.3 BLUFF BODY ENHANCED PERFORMANCE VALIDATION & CHARACTERIZATION

In all tried cases, the magnitude of the average power generation increased in the presence of a bluff body. Forced excitation of the aeroelastic instability enhanced the power output, whether the forced excitation was periodic/sinusoidal, as with vortex shedding from a bluff body, or wideband, as with induced turbulence due to boundary layers. This proves that an AIEH is suitable in more installation locations than a turbine, and contrary to a turbine will have an enhancement in power generation.

The results in the final section of the MiniHornet chapter (5.4.2) are very promising. They show a linear region of enhanced excitation can be induced into an AIEH due to a circular bluff body. Though the effort was unsuccessful at targeting a specific region of the AIEH's natural excitation, with further research it is highly conceivable one would be capable of targeting the AIEH's natural region of resonance with the linear forced excitation region.

Future Recommendations: Describing the forced excitation due to a bluff body is essential to fully utilize the proven enhancement in performance bluff bodies provide to an AIEH. All structures where one would implement an AIEH have different types/sizes of bluff bodies (i.e. bridge trusses vs window cut-outs). Each different bluff body introduces its own erratic flow conditions and performance enhancing forced excitation of the AIEH that, with a proper understanding, may be used to increase power generation.

Understanding this performance enhancing forced excitation can be done by extending the describing function matrix method to the case of sinusoidally excited systems; utilizing the Van der Pol techniques to evaluate the linearized response of the system about the LCO, which will evaluate the frequency response of the system to vortex (sinusoidal) and turbulent (wideband) excitation on and off resonance. An effort to quantify this enhancing effect and develop the tools to characterize the response of a device should be conducted.

The addition of this model to the aforementioned LCO simulation will provide the ability to design an AIEH for placement near a specific bluff body, in locations not ideal for a turbine.

APPENDIX

A.1 HORNET EXPERMIENT MATLAB CODE

A.1.1 INITIAL CHANGE OF LENGTH EXPERIMENTS

```
%%%%%%%%%%%%%%%%%%%%%%%%%%%%%%%%%%%%%%%%%%%%%%%%%%%%%%%%%%%%%%%%%%%%%%%%%%%%

%Timothy Bagatti
%Hornet Experiments
%Data was originally taken with a digital oscilloscope that places
%the data into Microsoft Excel
%This code loads that data and manipulates it for open circuit power

clear all
close all

date = [num2str(05132010) '_trial1']; %saving date plus day run number
N = 2247; %Total number of samples

%LENGTH CHANGE EXPERIMENTS
Lfs = 500;%[hz] Sample Rate
Ldelta_t = 1/Lfs; %setting delta t
Ltime_T = N/Lfs; %computing total run time

%allocating space
Llengthnum = 4; %setting number of lengths measured
Lchannelnum = 4; %setting number of channels measured
Lbluffnum = 2; %setting number of measured bluff configurations
Llengthval = [14 20 26 32]; %input measured lengths
Lresval = [63.876 76.14 58.879 69.455]; %respective solenoid resistance
%value [ohm]

Lvolts.no = zeros(N,Lchannelnum,Llengthnum); %voltage without a bluff body
Lvolts.yes = zeros(N,Lchannelnum,Llengthnum); %voltage with a bluff body
Lpower = zeros(Llengthnum,2);
partialPnoL = zeros(N,Lchannelnum,Llengthnum);
partialPyesL = zeros(N,Lchannelnum,Llengthnum);

%reading in data and calculating standard deviation
%no bluff
Lvolts.no(:,:,1) = xlsread('HorizontalFirstRoundVoltageData','Sheet1'...
    ,'A4:D2250');
Lvolts.no(:,:,2) = xlsread('HorizontalFirstRoundVoltageData','Sheet1'...
    ,'I4:L2250');
Lvolts.no(:,:,3) = xlsread('HorizontalFirstRoundVoltageData','Sheet1'...
    ,'Q4:T2250');
Lvolts.no(:,:,4) = xlsread('HorizontalFirstRoundVoltageData','Sheet1'...
    ,'Y4:AB2250');
%bluff body
Lvolts.yes(:,:,1) = xlsread('HorizontalFirstRoundVoltageData','Sheet1'...
    ,'E4:H2250');
Lvolts.yes(:,:,2) = xlsread('HorizontalFirstRoundVoltageData','Sheet1'...
    ,'M4:P2250');
Lvolts.yes(:,:,3) = xlsread('HorizontalFirstRoundVoltageData','Sheet1'...
    ,'U4:X2250');
Lvolts.yes(:,:,4) = xlsread('HorizontalFirstRoundVoltageData','Sheet1'...
    ,'AC4:AF2250');


%saving voltage data
eval(['save LengthChangeVoltage' '_' date ' Lvolts']);
%loading voltage data if need shall arise
```

```
eval(['load LengthChangeVoltage' '_' date ' Lvolts']);

%manipulating data for average power output
for j = 1:Llengthnum %altering lengths
    for i = 1:2 %altering bluff bodies
        if i == 1
            for R = 1:4 %for each measure solenoid
                Lpower(j,i) = Lpower(j,i) + sum(Lvolts.no(:,R,j).^2).*...
                    Ldelta_t./(Lresval(R)*Ltime_T);
            end
        else
            for R = 1:4 %for each measure solenoid
                Lpower(j,i) = Lpower(j,i) + sum(Lvolts.yes(:,R,j).^2).*...
                    Ldelta_t./(Lresval(R)*Ltime_T);
            end
        end
    end
end

%calculating uncertainty
for R = 1:4
    partialPnoL(:,R,:) = 2/(N*Lresval(R))*Lvolts.no(:,R,:);
end
for R = 1:4
    partialPyesL(:,R,:) = 2/(N*Lresval(R))*Lvolts.yes(:,R,:);
end
UnoL = zeros(Llengthnum,1);
UyesL = zeros(Llengthnum,1);
for i = 1:Llengthnum
    for R = 1:4
    UnoL(i,1) = UnoL(i,1) + sqrt(sum(partialPnoL(:,R,i)*0.005)^2);
    UyesL(i,1) = UyesL(i,1) + sqrt(sum(partialPyesL(:,R,i)*0.005)^2);
    end
end
U_L = zeros(Llengthnum,2);
for i = 1:Llengthnum
   U_L(i,1) = UnoL(i,1);
   U_L(i,2) = UyesL(i,1);
end

%saving power data
eval(['save LengthChangePower' '_' date ' Lpower']);
%loading power data if need shall arise
eval(['load LengthChangePower' '_' date ' Lpower']);

%plotting the average power at varied lengths with and without bluffs
figure(1)
errorbar(Llengthval,Lpower(:,1),U_L(:,1))
hold on
errorbar(Llengthval,Lpower(:,2),U_L(:,2))
xlabel('length[in]')
ylabel('Power [watts]')
title('Power output at various length w/and w/o a bluff')
legend('no bluff','yes bluff')

%%%%%%%%%%%%%%%%%%%%%%%%%%%%%%%%%%%%%%%%%%%%%%%%%%%%%%%%%%%%%%%%%%%%%%%%%%%%%%%
```

A.1.2 EMI ENGINE REDESIGN EXPERIMENTS

```
%%%%%%%%%%%%%%%%%%%%%%%%%%%%%%%%%%%%%%%%%%%%%%%%%%%%%%%%%%%%%%%%%%%%%%%%%%%%%%%
%EMI ENGINE REDESIGN EXPERIMENTS

%Timothy Bagatti
%Hornet Experiments

Efs = [250 250 1000 1000 1000];%[hz] Sample Rate
```

```
Edelta_t = 1./Efs; %setting delta t
Etime_T = N./Efs; %computing total run time
Elengthnum = 5; %setting number of lengths measured
Ebluffnum = 2; %setting number of tested bluff configurations
EchannelnumEMI = 4; %setting number of EMI channels measured
EchannelnumPVDF = 5; %setting number of EMI channels measured
Elengthval = [14 21 28 35 42]; %input measured lengths
Eresval = [330 305 330 305];%respective solenoid resistance values [ohm]
Efreqval = [13 13;10 14;15 30;20 14;30 30]; %average frequency of
%excitation

%allocating space
EvoltsEMI.no = zeros(N,EchannelnumEMI,Elengthnum); %voltage without a
%bluff body EMI
EvoltsEMI.yes = zeros(N,EchannelnumEMI,Elengthnum); %voltage with a
%bluff body EMI
EvoltsPVDF.no = zeros(N,EchannelnumPVDF,Elengthnum); %voltage without a
%bluff body PVDF
EvoltsPVDF.yes = zeros(N,EchannelnumPVDF,Elengthnum); %voltage with a
%bluff body PVDF

Epower = zeros(Elengthnum,Ebluffnum,2); %average power for change in
%length, bluff config, and EMI and PVDF

%reading in data
EvoltsEMI.no(:,:,1) = xlsread('EMIEngineRedesign','Sheet1'...
    ,'A5:D2251');
EvoltsEMI.no(:,:,2) = xlsread('EMIEngineRedesign','Sheet1'...
    ,'K5:N2251');
EvoltsEMI.no(:,:,3) = xlsread('EMIEngineRedesign','Sheet1'...
    ,'W5:Z2251');
EvoltsEMI.no(:,:,4) = xlsread('EMIEngineRedesign','Sheet1'...
    ,'AK5:AN2251');
EvoltsEMI.no(:,:,5) = xlsread('EMIEngineRedesign','Sheet1'...
    ,'BA5:BD2251');

EvoltsEMI.yes(:,:,1) = xlsread('EMIEngineRedesign','Sheet1'...
    ,'F5:I2251');
EvoltsEMI.yes(:,:,2) = xlsread('EMIEngineRedesign','Sheet1'...
    ,'Q5:T2251');
EvoltsEMI.yes(:,:,3) = xlsread('EMIEngineRedesign','Sheet1'...
    ,'AD5:AG2251');
EvoltsEMI.yes(:,:,4) = xlsread('EMIEngineRedesign','Sheet1'...
    ,'AS5:AV2251');
EvoltsEMI.yes(:,:,5) = xlsread('EMIEngineRedesign','Sheet1'...
    ,'BJ5:BM2251');

EvoltsPVDF.no(:,1,1) = xlsread('EMIEngineRedesign','Sheet1'...
    ,'E5:E2251');
EvoltsPVDF.no(:,1:2,2) = xlsread('EMIEngineRedesign','Sheet1'...
    ,'O5:P2251');
EvoltsPVDF.no(:,1:3,3) = xlsread('EMIEngineRedesign','Sheet1'...
    ,'AA5:AC2251');
EvoltsPVDF.no(:,1:4,4) = xlsread('EMIEngineRedesign','Sheet1'...
    ,'AO5:AR2251');
EvoltsPVDF.no(:,1:5,5) = xlsread('EMIEngineRedesign','Sheet1'...
    ,'BE5:BI2251');

EvoltsPVDF.yes(:,1,1) = xlsread('EMIEngineRedesign','Sheet1'...
    ,'J5:J2251');
EvoltsPVDF.yes(:,1:2,2) = xlsread('EMIEngineRedesign','Sheet1'...
    ,'U5:V2251');
EvoltsPVDF.yes(:,1:3,3) = xlsread('EMIEngineRedesign','Sheet1'...
    ,'AH5:AJ2251');
EvoltsPVDF.yes(:,1:4,4) = xlsread('EMIEngineRedesign','Sheet1'...
    ,'AW5:AZ2251');
EvoltsPVDF.yes(:,1:5,5) = xlsread('EMIEngineRedesign','Sheet1'...
    ,'BN5:BR2251');
```

```
%saving voltage data
eval(['save EMIRedesignEMIVoltage' '_' date ' EvoltsEMI']);
eval(['save EMIRedesignPVDFVoltage' '_' date ' EvoltsPVDF']);
%loading voltage data if need shall arise
eval(['load EMIRedesignEMIVoltage' '_' date ' EvoltsEMI']);
eval(['load EMIRedesignPVDFVoltage' '_' date ' EvoltsPVDF']);


%manipulating data for average power output
%EMI engines
for j = 1:Elengthnum %altering lengths
    for i = 1:Ebluffnum %altering bluff bodies
        if i == 1
            for R = 1:EchannelnumEMI %for each measure solenoid
                Epower(j,i,1) = Epower(j,i,1) + ...
                    sum(EvoltsEMI.no(:,R,j)...
                    .^2).*Edelta_t(j)./(Eresval(R)*Etime_T(j));
            end
        else
            for R = 1:4 %for each measure solenoid
                Epower(j,i,1) = Epower(j,i,1) + ...
                    sum(EvoltsEMI.yes(:,R,j)...
                    .^2).*Edelta_t(j)./(Eresval(R)*Etime_T(j));
            end
        end
    end
end

partialPnoEMI = zeros(N,EchannelnumEMI,Elengthnum);
partialPyesEMI = zeros(N,EchannelnumEMI,Elengthnum);

%calculating uncertainty
for R = 1:EchannelnumEMI
    partialPnoEMI(:,R,:) = 2/(N*Eresval(R))*EvoltsEMI.no(:,R,:);
end
for R = 1:EchannelnumEMI
    partialPyesEMI(:,R,:) = 2/(N*Eresval(R))*EvoltsEMI.yes(:,R,:);
end
UnoEMI = zeros(Elengthnum,1);
UyesEMI = zeros(Elengthnum,1);
for i = 1:Elengthnum
    for R = 1:EchannelnumEMI
    UnoEMI(i,1) = UnoEMI(i,1) + sqrt(sum(partialPnoEMI(:,R,i)*0.005)^2);
    UyesEMI(i,1) = UyesEMI(i,1) + sqrt(sum(partialPyesEMI(:,R,i)*0.005)^2);
    end
end
U_EMI = zeros(Llengthnum,2);
for i = 1:Elengthnum
   U_EMI(i,1) = UnoEMI(i,1);
   U_EMI(i,2) = UyesEMI(i,1);
end

%PVDF strips
for j = 1:Elengthnum %altering lengths
    for i = 1:Ebluffnum %altering bluff bodies
        if i == 1
            for k = 1:EchannelnumPVDF %for each measure PDVF strip
                Epower(j,i,2) = Epower(j,i,2) + ...
                    sum(EvoltsPVDF.no(:,k,j).^2).*8.587*10^(-9)...
                    .*Edelta_t(j).*Efreqval(j,i)./Etime_T(j);
            end
        else
            for k = 1:5 %for each measure PVDF strip
                Epower(j,i,2) = Epower(j,i,2) + ...
                    sum(EvoltsPVDF.yes(:,k,j).^2).*8.587*10^(-9)...
                    .*Edelta_t(j).*Efreqval(j,i)./Etime_T(j);
```

```
            end
        end
    end
end

partialPnoPVDF = zeros(N,EchannelnumPVDF,Elengthnum);
partialPyesPVDF = zeros(N,EchannelnumPVDF,Elengthnum);

%calculating uncertainty
for R = 1:Elengthnum
    partialPnoPVDF(:,:,R) = 2*8.587*10^(-9).*Edelta_t(R)...
        .*Efreqval(R,1).*EvoltsPVDF.no(:,R,:)./Etime_T(R);
end
for R = 1:Elengthnum
    partialPyesPVDF(:,:,R) = 2*8.587*10^(-9).*Edelta_t(R)...
        .*Efreqval(R,2).*EvoltsPVDF.no(:,R,:)./Etime_T(R);
end
UnoPVDF = zeros(Elengthnum,1);
UyesPVDF = zeros(Elengthnum,1);
for i = 1:Elengthnum
    for R = 1:EchannelnumPVDF
    UnoPVDF(i,1) = UnoPVDF(i,1) + sqrt(sum(partialPnoPVDF(:,R,i)*0.005)^2);
    UyesPVDF(i,1) = UyesPVDF(i,1) + sqrt(sum(partialPyesPVDF(:,R,i)*0.005)^2);
    end
end
U_PVDF = zeros(Llengthnum,2);
for i = 1:Elengthnum
   U_PVDF(i,1) = UnoPVDF(i,1);
   U_PVDF(i,2) = UyesPVDF(i,1);
end


%saving power data
eval(['save EMIRedesignPower' '_' date ' Epower']);
%loading power data if need shall arise
eval(['load EMIRedesignPower' '_' date ' Epower']);

%plotting the average power at varied lengths with and without bluffs
figure(2)
errorbar(Elengthval,Epower(:,1,1),U_EMI(:,1))
hold on
errorbar(Elengthval,Epower(:,2,1),U_EMI(:,2))
xlabel('length[in]')
ylabel('Power [watts]')
title('EMI Power output at various length w/and w/o a bluff')
legend('no bluff','yes bluff')


figure(3)
errorbar(Elengthval,Epower(:,1,2),U_PVDF(:,1))
hold on
errorbar(Elengthval,Epower(:,2,2),U_PVDF(:,2))
xlabel('length[in]')
ylabel('Power [watts]')
title('PVDF Power output at various length w/and w/o a bluff')
legend('no bluff','yes bluff')
%%%%%%%%%%%%%%%%%%%%%%%%%%%%%%%%%%%%%%%%%%%%%%%%%%%%%%%%%%%%%%%%%%%%%%%%%%%%%%%
```

A.1.3 TENSIONER IMPLEMENTATION EXPERIMENTS

```
%%%%%%%%%%%%%%%%%%%%%%%%%%%%%%%%%%%%%%%%%%%%%%%%%%%%%%%%%%%%%%%%%%%%%%%%%%%%%%%
%TENSIONER IMPLEMENTATION

%Timothy Bagatti
%Hornet Experiments
```

```
Tfs = 1000;%[hz] Sample Rate
Tdelta_t = 1/Tfs; %setting delta t
Ttime_T = N/Tfs; %computing total run time
TchannelnumEMI = 4; %setting number of EMI channels measured
TchannelnumPVDF = 5; %setting number of EMI channels measured
Tresval = [330 305 330 305 1]; %respective solenoid resistance values
%[ohm] the 1 it just a place holder
Tfreqval = [13 14 30 20 30]; %average frequency of excitation

%allocating space
Tvolts = zeros(N,TchannelnumPVDF,2); %voltage without a bluff body EMI
Tpower = zeros(1,2); %average power for change in length, bluff config,
%and EMI and PVDF

%reading in data
Tvolts(:,1:4,1) = xlsread('TensionerImplementation','Sheet1','A3:D2249');
Tvolts(:,:,2) = xlsread('TensionerImplementation','Sheet1','E3:I2249');

%saving voltage data
eval(['save TensionerImplementationVoltage' '_' date ' Tvolts']);
%loading voltage data if need shall arise
eval(['load TensionerImplementationVoltage' '_' date ' Tvolts']);

%manipulating data for average power output
for k = 1:TchannelnumPVDF%for various channels
    %EMI engines
    Tpower(1) = Tpower(1) + sum(Tvolts(:,k,1).^2).*Tdelta_t./...
        (Tresval(k)*Ttime_T);
    %PVDF strips
    Tpower(2) = Tpower(2) + sum(Tvolts(:,k,2).^2).*8.587*10^(-9)...
        .*Tdelta_t.*Tfreqval(k)./Ttime_T;
end


%saving power data
eval(['save TensionerImplementationPower' '_' date ' Tpower']);
%loading power data if need shall arise
eval(['load TensionerImplementationPower' '_' date ' Tpower']);

format long
Tpower

%%%%%%%%%%%%%%%%%%%%%%%%%%%%%%%%%%%%%%%%%%%%%%%%%%%%%%%%%%%%%%%%%%%%%%%%%%%%
```

A.2 MINHORNET EXPERIMENTS MATLAB CODE

A.2.1 POWER VERSUS LOAD AND VELOCITY

```
%%%%%%%%%%%%%%%%%%%%%%%%%%%%%%%%%%%%%%%%%%%%%%%%%%%%%%%%%%%%%%%%%%%%%%%%%%%%

%Timothy Bagatti
%MiniHornet Experiments
%Data Acquisition for Power vs Load and Velocity

%MUST use following command to figure out how daq ID is declared before
%starting: daqhwinfo('nidaq')


%PREAMBLE - setting sample size and rate
date = [num2str(04072010) '_real1']; %saving date plus day run number
time_T = 30; %setting total run time to 30 sec
fs = 1000;%[hz] Sample Rate
fN = fs/2; % Setting Nyquist frequency
```

```
N = fs*time_T; %Total number of samples... setting to save 30sec worth
delta_t = 1/fs; %setting delta t
velnum = 7; %setting number of velocities
resnum = 21; %setting number of resistances

%PRELIM - opening and setting data acquisiton card and channels
ai = analoginput('nidaq','dev3'); %setting up to acquire data in variable
%"ai"
ch = addchannel(ai,(0:3)); %setting to acquire data in channels 0-3 to
%variable "Volts"

%PRETRIGGER - setting sample resolution and triggering
set(ai,'SampleRate',fs);   %setting sample rate to 1000Hz
set(ai,'SamplesPerTrigger',N);   %setting sample length to 30s
%set(ai,'InputRange',[-5 5]); %setting input range to 5 volt spread
ai.Channel(1).InputRange = [-5 5];
ai.Channel(2).InputRange = [-5 5];
ai.Channel(3).InputRange = [-5 5];
ai.Channel(4).InputRange = [-5 5];
set(ai,'triggerChannel',ch(1)); %setting trigger to channel 1
set(ai,'TriggerType','Software'); %required when specify following
%conditions
set(ai,'TriggerCondition','Rising'); %setting rising trigger slope type
set(ai,'TriggerConditionValue',0); %setting trigger voltage level

%Allocating space
resval = zeros(resnum,1);
velval = zeros(velnum,1);
power = zeros(resnum,velnum,4);

%Start loop of data acquisition
for R = 1:resnum; %outer resistance loop

%Input resistance
resval(R) = input('Please input resistance value[ohms]: ');

for V = 1:velnum; %inner velocity loop

%Input velocity
velval(V) = input('Please input velocity value[Hz]: ');

%BEGIN TRIGGER - acquiring data
start(ai);
Volts = getdata(ai); %saving to matrix "Volts"

%Saving the run data
eval(['save Vel' num2str(velval(V)) '_Res' num2str(resval(R)) '_' date ...
    ' Volts']); %save to run_ , saving Volts

%Manipulate data
power(R,V,:) = sum(Volts.^2)*delta_t/(resval(R)*time_T);%calculating
%average power

end
end

%calculating coefficient of performance
velnew = velval*0.3048; %converting velocity to m/s
for i = 1:velnum
    for j = 1:resnum
        for k = 1:4
            CP(j,i,k) = power(j,i,k)/(0.5*1.204*0.00191*velnew(i)^3);
        end
    end
end

%Saving power matrix
eval(['save power_' date ' power resval velval']);
```

```
%surface plots
figure(1)
surf(velval,1./resval,power(:,:,1))
set(gca,'yscale','log')
ylabel('1/R [ohms]')
xlabel('Velocity [fps]')
zlabel('power [watts]')
title('Load vs Velocity vs Power - channel 1')

figure(2)
surf(velval,1./resval,power(:,:,2))
set(gca,'yscale','log')
ylabel('1/R [ohms]')
xlabel('Velocity [fps]')
zlabel('power [watts]')
title('Load vs Velocity vs Power - channel 2')

figure(3)
surf(velval,1./resval,power(:,:,3))
set(gca,'yscale','log')
ylabel('1/R [ohms]')
xlabel('Velocity [fps]')
zlabel('power [watts]')
title('Load vs Velocity vs Power - channel 3')

figure(4)
surf(velval,1./resval,power(:,:,4))
set(gca,'yscale','log')
ylabel('1/R [ohms]')
xlabel('Velocity [fps]')
zlabel('power [watts]')
title('Load vs Velocity vs Power - channel 4')

%2D load vs power plots at multiple velocities
figure(5)
semilogx(1./resval,power(:,:,1))
xlabel('1/R')
ylabel('Power [watts]')
title('Power vs Load at various Velocity - channel 1')
legend('36','40','44','48','52','56','60')

figure(6)
semilogx(1./resval,power(:,:,2))
xlabel('1/R')
ylabel('Power [watts]')
title('Power vs Load at various Velocity - channel 2')
legend('36','40','44','48','52','56','60')

figure(7)
semilogx(1./resval,power(:,:,3))
xlabel('1/R')
ylabel('Power [watts]')
title('Power vs Load at various Velocity - channel 3')
legend('36','40','44','48','52','56','60')

figure(8)
semilogx(1./resval,power(:,:,4))
xlabel('1/R')
ylabel('Power [watts]')
title('Power vs Load at various Velocity - channel 4')
legend('36','40','44','48','52','56','60')

%mesh plots
figure(9)
mesh(velval,1./resval,power(:,:,1))
set(gca,'yscale','log')
ylabel('1/R [ohms]')
```

```
xlabel('Velocity [fps]')
zlabel('power [watts]')
title('Load vs Velocity vs Power')

figure(10)
mesh(velval,1./resval,power(:,:,2))
set(gca,'yscale','log')
ylabel('1/R [ohms]')
xlabel('Velocity [fps]')
zlabel('power [watts]')
title('Load vs Velocity vs Power')

figure(11)
mesh(velval,1./resval,power(:,:,3))
set(gca,'yscale','log')
ylabel('1/R [ohms]')
xlabel('Velocity [fps]')
zlabel('power [watts]')
title('Load vs Velocity vs Power')

figure(12)
mesh(velval,1./resval,power(:,:,4))
set(gca,'yscale','log')
ylabel('1/R [ohms]')
xlabel('Velocity [fps]')
zlabel('power [watts]')
title('Load vs Velocity vs Power')

%coeficient of performance plots
figure(13)
semilogx(1./resval,CP(:,:,1))
xlabel('1/R')
ylabel('Cp')
title('Coeffiecient of Perfomance vs Load at various Velocity - channel 1')
legend('36','40','44','48','52','56','60')

figure(14)
semilogx(1./resval,CP(:,:,2))
xlabel('1/R')
ylabel('Cp')
title('Coeffiecient of Perfomance vs Load at various Velocity - channel 2')
legend('36','40','44','48','52','56','60')

figure(15)
semilogx(1./resval,CP(:,:,3))
xlabel('1/R')
ylabel('Cp')
title('Coeffiecient of Perfomance vs Load at various Velocity - channel 3')
legend('36','40','44','48','52','56','60')

figure(16)
semilogx(1./resval,CP(:,:,4))
xlabel('1/R')
ylabel('Cp')
title('Coeffiecient of Perfomance vs Load at various Velocity - channel 4')
legend('36','40','44','48','52','56','60')

%CLEAN UP - clean up
delete(ai);
clear ai;

%%%%%%%%%%%%%%%%%%%%%%%%%%%%%%%%%%%%%%%%%%%%%%%%%%%%%%%%%%%%%%%%%%%%%%%%%%%%%%%
```

A.2.2 POWER VERSUS LOAD AND VELOCITY REDO

```
%%%%%%%%%%%%%%%%%%%%%%%%%%%%%%%%%%%%%%%%%%%%%%%%%%%%%%%%%%%%%%%%%%%%%%%%%%%%%%%
```

```
%Timothy Bagatti
%MiniHornet Experiments
%Data Acquisition for Power vs Load and Velocity Redo

date = [num2str(04072010) '_real1'];

eval(['load power_' date ' power resval velval']);

velval = [22.35; 25.00; 27.05; 30.30; 32.94; 35.59; 38.24]

%surface plots
figure(1)
surf(velval,1./resval,power(:,:,1))
set(gca,'yscale','log')
ylabel('1/R [ohms]')
xlabel('Velocity [mph]')
zlabel('power [watts]')
title('Load vs Velocity vs Power - channel 1')

figure(2)
surf(velval,1./resval,power(:,:,2))
set(gca,'yscale','log')
ylabel('1/R [ohms]')
xlabel('Velocity [mph]')
zlabel('power [watts]')
title('Load vs Velocity vs Power - channel 2')

figure(3)
surf(velval,1./resval,power(:,:,3))
set(gca,'yscale','log')
ylabel('1/R [ohms]')
xlabel('Velocity [mph]')
zlabel('power [watts]')
title('Load vs Velocity vs Power - channel 3')

figure(4)
surf(velval,1./resval,power(:,:,4))
set(gca,'yscale','log')
ylabel('1/R [ohms]')
xlabel('Velocity [mph]')
zlabel('power [watts]')
title('Load vs Velocity vs Power - channel 4')

%2D load vs power plots at multiple velocities
figure(5)
semilogx(1./resval,power(:,:,1))
xlabel('1/R')
ylabel('Power [watts]')
title('Power vs Load at various Velocity - channel 1')
legend('22.35','25.00','27.05','30.30','32.94','35.59','38.24')%in mph
%legend('36','40','44','48','52','56','60')%equivalent in Hz

figure(6)
semilogx(1./resval,power(:,:,2))
xlabel('1/R')
ylabel('Power [watts]')
title('Power vs Load at various Velocity - channel 2')
legend('22.35','25.00','27.05','30.30','32.94','35.59','38.24')%in mph
%legend('36','40','44','48','52','56','60')%equivalent in Hz

figure(7)
semilogx(1./resval,power(:,:,3))
xlabel('1/R')
ylabel('Power [watts]')
title('Power vs Load at various Velocity - channel 3')
legend('22.35','25.00','27.05','30.30','32.94','35.59','38.24')%in mph
%legend('36','40','44','48','52','56','60')%equivalent in Hz
```

```
figure(8)
semilogx(1./resval,power(:,:,4))
xlabel('1/R')
ylabel('Power [watts]')
title('Power vs Load at various Velocity - channel 4')
legend('22.35','25.00','27.05','30.30','32.94','35.59','38.24')%in mph
%legend('36','40','44','48','52','56','60')%equivalent in Hz

%mesh plots
figure(9)
mesh(velval,1./resval,power(:,:,1))
set(gca,'yscale','log')
ylabel('1/R [ohms]')
xlabel('Velocity [Hz]')
zlabel('power [watts]')
title('Power vs Load & Velocity - Channel 1')

figure(10)
mesh(velval,1./resval,power(:,:,2))
set(gca,'yscale','log')
ylabel('1/R [ohms]')
xlabel('Velocity [Hz]')
zlabel('power [watts]')
title('Power vs Load & Velocity - Channel 2')

figure(11)
mesh(velval,1./resval,power(:,:,3))
set(gca,'yscale','log')
ylabel('1/R [ohms]')
xlabel('Velocity [Hz]')
zlabel('power [watts]')
title('Power vs Load & Velocity - Channel 3')

figure(12)
mesh(velval,1./resval,power(:,:,4))
set(gca,'yscale','log')
ylabel('1/R [ohms]')
xlabel('Velocity [Hz]')
zlabel('power [watts]')
title('Power vs Load & Velocity - Channel 4')

%coeficient of performance plots
figure(13)
semilogx(1./resval,CP(:,:,1))
xlabel('1/R')
ylabel('Cp')
title('Coeffiecient of Perfomance vs Load at various Velocity - channel 1')
legend('36','40','44','48','52','56','60')

figure(14)
semilogx(1./resval,CP(:,:,2))
xlabel('1/R')
ylabel('Cp')
title('Coeffiecient of Perfomance vs Load at various Velocity - channel 2')
legend('36','40','44','48','52','56','60')

figure(15)
semilogx(1./resval,CP(:,:,3))
xlabel('1/R')
ylabel('Cp')
title('Coeffiecient of Perfomance vs Load at various Velocity - channel 3')
legend('36','40','44','48','52','56','60')

figure(16)
semilogx(1./resval,CP(:,:,4))
xlabel('1/R')
ylabel('Cp')
```

```
title('Coeffiecient of Perfomance vs Load at various Velocity - channel 4')
legend('36','40','44','48','52','56','60')

%%%%%%%%%%%%%%%%%%%%%%%%%%%%%%%%%%%%%%%%%%%%%%%%%%%%%%%%%%%%%%%%%%%%%%%%%%%%
```

A.2.3 FREQUENCY RESPONSE FUNCTION EXPERIMENTS

```
%%%%%%%%%%%%%%%%%%%%%%%%%%%%%%%%%%%%%%%%%%%%%%%%%%%%%%%%%%%%%%%%%%%%%%%%%%%%

%Timothy Bagatti
%MiniHornet Frequency Function Plotting Code
%04/23/2010

clear all
format short e
format compact

%Location 1 through 3

data1 = load('-mat','Loc1_Trial1_100HzBW_5Gain_10V_04222010.vna');
xfer1 = data1.SLm.xcmeas(1,2).xfer;
freq1 = data1.SLm.fdxvec;

data2 = load('-mat','Loc2_Trial1_100HzBW_5Gain_10V_04222010.vna');
xfer2 = data2.SLm.xcmeas(1,2).xfer;
freq2 = data2.SLm.fdxvec;

data3 = load('-mat','Loc3_Trial1_100HzBW_5Gain_10V_04222010.vna');
xfer3 = data3.SLm.xcmeas(1,2).xfer;
freq3 = data3.SLm.fdxvec;

figure(1),
subplot(211),
semilogy(freq1,abs(xfer1))
xlabel('freq (Hz)')
ylabel('magnitude (dB)')
title('Frequency Response Function: coil to LDV'...
    '(Belt Center/Front Edge - Loc 1)')
xlim([ 0 100 ])

subplot(212),
plot(freq1,angle(xfer1))
xlabel('freq (Hz)')
ylabel('phase angle (radians)')
xlim([ 0 100 ])

figure(2),
subplot(211),
semilogy(freq2,abs(xfer2))
xlabel('freq (Hz)')
ylabel('magnitude (dB)')
title('Frequency Response Function: coil to LDV'...
    '(Belt Center/Middle - Loc 2)')
xlim([ 0 100 ])

subplot(212),
plot(freq2,angle(xfer2))
xlabel('freq (Hz)')
ylabel('phase angle (radians)')
xlim([ 0 100 ])

figure(3),
subplot(211),
semilogy(freq3,abs(xfer3))
xlabel('freq (Hz)')
ylabel('magnitude (dB)')
```

```
title('Frequency Response Function: coil to LDV'...
    '(Belt Center/Back Edge - Loc 3)')
xlim([ 0 100 ])

subplot(212),
plot(freq3,angle(xfer3))
xlabel('freq (Hz)')
ylabel('phase angle (radians)')
xlim([ 0 100 ])


figure(4),
subplot(211),
semilogy(...
    freq1,abs(xfer1),...
    freq2,abs(xfer2),...
    freq3,abs(xfer3))
xlabel('freq (Hz)')
ylabel('magnitude (dB)')
title('Frequency Response Functions: coil to LDV (Belt Center)')
legend('loc 1','loc 2','loc 3',4)
xlim([ 0 100 ])

subplot(212),
plot(...
    freq1,angle(xfer1),...
    freq2,angle(xfer2),...
    freq3,angle(xfer3))
xlabel('freq (Hz)')
ylabel('phase angle (radians)')
xlim([ 0 100 ])

%%%%%%%%%%%%%%%%%%%%%%%%%%%%%%%%%%%%%%%%%%%%%%%%%%%%%%%%%%%%%%%%%%%%%%%%%%%%%%%
```

A.2.4 PSD EXPERIMENTS

```
%%%%%%%%%%%%%%%%%%%%%%%%%%%%%%%%%%%%%%%%%%%%%%%%%%%%%%%%%%%%%%%%%%%%%%%%%%%%%%%

%Timothy Bagatti
%MiniHornet Experiments
%Data Acquisition for PowerSpectralDensity

%MUST use following command to figure out how daq ID is declared before
%starting: daqhwinfo('nidaq')


%PREAMBLE - setting sample size and rate
date = [num2str(04282010) '_Solenoid_trial1']; %saving date plus day run
%number
time_T = 30; %setting total run time to 30 sec
fs = 1000;%[hz] Sample Rate
fN = fs/2; % Setting Nyquist frequency
N = fs*time_T; %Total number of samples... setting to save 30sec worth
delta_t = 1/fs; %setting delta t
velnum = 41; %setting number of velocities

%PRELIM - opening and setting data acquisiton card and channels
ai = analoginput('nidaq','dev4'); %setting up to acquire data in variable
%"ai"
ch = addchannel(ai,(0:1)); %setting to acquire data in channels 0 to
%variable "Volts"

%PRETRIGGER - setting sample resolution and triggering
set(ai,'SampleRate',fs);   %setting sample rate to 1000Hz
set(ai,'SamplesPerTrigger',N);   %setting sample length to 30s
%set(ai,'InputRange',[-5 5]); %setting input range to 5 volt spread
```

```
ai.Channel(1).InputRange = [-10 10];
set(ai,'triggerChannel',ch(1)); %setting trigger to channel 1
set(ai,'TriggerType','Software'); %required when specify following
%conditions
set(ai,'TriggerCondition','Rising'); %setting rising trigger slope type
set(ai,'TriggerConditionValue',0); %setting trigger voltage level

%Allocating space
velval = zeros(velnum,1);
PSD = zeros(2049,velnum,2);
Pxx1 = zeros(velnum);
Pxx2 = zeros(velnum);

%Start loop of data acquisition
for V = 1:velnum; %inner velocity loop

%Input velocity
velval(V) = input('Please input velocity value[Hz]: ');

%BEGIN TRIGGER - acquiring data
start(ai);
Volts = getdata(ai); %saving to matrix "Volts"

%Saving the run data
eval(['save Vel' num2str(velval(V)) '_' date ' Volts']); %saving Volts

%Manipulate data
%Channel1_BottomLeftSolenoid
[Pxx1,W] = pwelch(Volts(:,1),boxcar(3750),[],[],fs);
PSD(:,V,1) = Pxx1;
%Channel2_BottomRightSolenoid
[Pxx2,W] = pwelch(Volts(:,2),boxcar(3750),[],[],fs);
PSD(:,V,2) = Pxx2;
end

%Saving power matrix
eval(['save pwelch_' date ' PSD velval']);

%plotting
figure(1)
subplot(2,1,1); semilogy(W,PSD(:,[1 2 3 4],1))
xlabel('frequency')
ylabel('PSD')
title('Power Spectral Density for 20-23[Hz] - Solenoid1')
legend('20','21','22','23')
subplot(2,1,2); semilogy(W,PSD(:,[1 2 3 4],2))
xlabel('frequency')
ylabel('PSD')
title('Solenoid2')

figure(2)
subplot(2,1,1); semilogy(W,PSD(:,[5 6 7 8],1))
xlabel('frequency')
ylabel('PSD')
title('Power Spectral Density for 24-27[Hz] - Solenoid1')
legend('24','25','26','27')
subplot(2,1,2); semilogy(W,PSD(:,[5 6 7 8],2))
xlabel('frequency')
ylabel('PSD')
title('Solenoid2')

figure(3)
subplot(2,1,1); semilogy(W,PSD(:,[9 10 11 12],1))
xlabel('frequency')
ylabel('PSD')
title('Power Spectral Density for 28-31[Hz] - Solenoid1')
legend('28','29','30','31')
subplot(2,1,2); semilogy(W,PSD(:,[9 10 11 12],2))
```

```
xlabel('frequency')
ylabel('PSD')
title('Solenoid2')

figure(4)
subplot(2,1,1); semilogy(W,PSD(:,[13 14 15 16],1))
xlabel('frequency')
ylabel('PSD')
title('Power Spectral Density for 32-35[Hz] - Solenoid1')
legend('32','33','34','35')
subplot(2,1,2); semilogy(W,PSD(:,[13 14 15 16],2))
xlabel('frequency')
ylabel('PSD')
title('Solenoid2')

figure(5)
subplot(2,1,1); semilogy(W,PSD(:,[17 18 19 20],1))
xlabel('frequency')
ylabel('PSD')
title('Power Spectral Density for 36-39[Hz] - Solenoid1')
legend('36','37','38','39')
subplot(2,1,2); semilogy(W,PSD(:,[17 18 19 20],2))
xlabel('frequency')
ylabel('PSD')
title('Solenoid2')

figure(6)
subplot(2,1,1); semilogy(W,PSD(:,[21 22 23 24],1))
xlabel('frequency')
ylabel('PSD')
title('Power Spectral Density for 40-43[Hz] - Solenoid1')
legend('40','41','42','43')
subplot(2,1,2); semilogy(W,PSD(:,[21 22 23 24],2))
xlabel('frequency')
ylabel('PSD')
title('Solenoid2')

figure(7)
subplot(2,1,1); semilogy(W,PSD(:,[25 26 27 28],1))
xlabel('frequency')
ylabel('PSD')
title('Power Spectral Density for 44-47[Hz] - Solenoid1')
legend('44','45','46','47')
subplot(2,1,2); semilogy(W,PSD(:,[25 26 27 28],2))
xlabel('frequency')
ylabel('PSD')
title('Solenoid2')

figure(8)
subplot(2,1,1); semilogy(W,PSD(:,[29 30 31 32],1))
xlabel('frequency')
ylabel('PSD')
title('Power Spectral Density for 48-51[Hz] - Solenoid1')
legend('48','49','50','51')
subplot(2,1,2); semilogy(W,PSD(:,[29 30 31 32],2))
xlabel('frequency')
ylabel('PSD')
title('Solenoid2')

figure(9)
subplot(2,1,1); semilogy(W,PSD(:,[33 34 35 36],1))
xlabel('frequency')
ylabel('PSD')
title('Power Spectral Density for 52-55[Hz] - Solenoid1')
legend('52','53','54','55')
subplot(2,1,2); semilogy(W,PSD(:,[33 34 35 36],2))
xlabel('frequency')
ylabel('PSD')
```

```
title('Solenoid2')

figure(10)
subplot(2,1,1); semilogy(W,PSD(:,[37 38 39 40 41],1))
xlabel('frequency')
ylabel('PSD')
title('Power Spectral Density for 56-60[Hz] - Solenoid1')
legend('56','57','58','59','60')
subplot(2,1,2); semilogy(W,PSD(:,[37 38 39 40 41],2))
xlabel('frequency')
ylabel('PSD')
title('Solenoid2')

%CLEAN UP - clean up
delete(ai);
clear ai;

%%%%%%%%%%%%%%%%%%%%%%%%%%%%%%%%%%%%%%%%%%%%%%%%%%%%%%%%%%%%%%%%%%%%%%%%%%%%%%%
```

A.2.5 STROUHAL FREQUENCY MATCHING EXPERIMENTS

```
%%%%%%%%%%%%%%%%%%%%%%%%%%%%%%%%%%%%%%%%%%%%%%%%%%%%%%%%%%%%%%%%%%%%%%%%%%%%%%%

%Timothy Bagatti
%MiniHornet Experiments
%Additional Plotting for PowerSpectralDensity
%Used to replot the origanal data

clear all
close all

date = [num2str(04282010) '_Solenoid_trial1']; %saving date plus day
%run number
velnum = 41;
fs = 1000;

velval = [20 21 22 23 24 25 26 27 28 29 30 31 32 33 34 35 36 37 38 39...
    40 41 42 43 44 45 46 47 48 49 50 51 52 53 54 55 56 57 58 59 60];



for V = 1:velnum; %inner velocity loop

eval(['load Vel' num2str(velval(V)) '_4282010_Solenoid_trial1' ]); %save
%to run_ , saving Volts

%Manipulate data
%Channel1_BottomLeftSolenoid
[Pxx1,W] = pwelch(Volts(:,1),boxcar(3750),[],[],fs);
PSD(:,V,1) = Pxx1;
%Channel2_BottomRightSolenoid
[Pxx2,W] = pwelch(Volts(:,2),boxcar(3750),[],[],fs);
PSD(:,V,2) = Pxx2;
end

%Saving power matrix
eval(['save pwelch_' date ' PSD velval']);

%Loading power matrix
eval(['load pwelch_' date ' PSD velval']);

%velocity in mph (can only use for ploting)
velval = [11.77 12.43 13.09 13.75 14.41 15.08 15.74 16.40 17.06 17.72...
    18.38 19.05 19.71 20.37 21.03 21.69 22.35 23.02 23.68 24.34 25.00...
    25.66 26.33 26.99 27.65 28.31 28.97 29.63 30.30 30.96 31.62 32.28...
    32.94 33.60 34.27 34.93 35.59 36.25 36.91 37.57 38.24];
```

```
%% surface and waterfall plots
[Vmx,Fmx] = meshgrid(velval,W);
PSD_dB = 10*log10(PSD(:,:,1));

figure(1),
waterfall(Fmx,Vmx,PSD_dB)
xlabel('frequency (Hz)')
ylabel('velocity (mph)')
view(2)

%my analysis for strouhal max bluff body analysis
format long
Vval = linspace(11.76784,38.23568);
fval = linspace(0,150);
mph2mps = 0.44704;
Vval_mps = mph2mps.*Vval;
L = 0.1524; %m characteristic flow length
mu = 15.11*10^(-6);
Re_mps = (Vval_mps.*L./mu);
S_Re = 0.2684-1.035./sqrt(Re_mps);
inch2mile = 1.57828283*10^(-5);
inch2meter =  0.0254;
D_in = 2; %diameter in inches
D_m = D_in*inch2meter;
VV = (D_m*fval)./S_Re;
mps2mph =  2.236936;
VVmph = VV*mps2mph;

figure(1),
hold on
plot(fval,VVmph)
hold off

%% strouhal max bluff body analysis
hz2mps = 0.2712;
St = 0.2645;
%D for equivalent velocity in Hz
%D = (hz2mps*Vmx)*St./Fmx;
%D for velocity in mph
D = (Vmx)*St./Fmx;

ff = linspace(20,60);
%vv = (ff*0.050./St)/hz2mps; % for equivalent velocity in Hz
vv = (ff*0.050./St); %velocity in mph

figure(1),
hold on
plot(ff,vv)
hold off

break

figure(2),
waterfall(Fmx,Vmx,D)
xlabel('frequency (Hz)')
ylabel('equivalent velocity (Hz)')
zlim([ 0 0.050 ])


%% 2D plots
break

%plotting
figure(1)
subplot(2,1,1); semilogy(W,PSD(:,[1 2 3 4],1))
xlabel('frequency')
```

```
ylabel('PSD')
title('Power Spectral Density for 11.77-13.75[mph]-Solenoid1')
legend('11.77','12.43','13.09','13.75')
subplot(2,1,2); semilogy(W,PSD(:,[1 2 3 4],2))
xlabel('frequency')
ylabel('PSD')
title('Solenoid2')

figure(2)
subplot(2,1,1); semilogy(W,PSD(:,[5 6 7 8],1))
xlabel('frequency')
ylabel('PSD')
title('Power Spectral Density for 14.41-16.40[mph]-Solenoid1')
legend('14.41','15.08','15.74','16.40')
subplot(2,1,2); semilogy(W,PSD(:,[5 6 7 8],2))
xlabel('frequency')
ylabel('PSD')
title('Solenoid2')

figure(3)
subplot(2,1,1); semilogy(W,PSD(:,[9 10 11 12],1))
xlabel('frequency')
ylabel('PSD')
title('Power Spectral Density for 17.06-19.05[mph]-Solenoid1')
legend('17.06','17.72','18.38','19.05')
subplot(2,1,2); semilogy(W,PSD(:,[9 10 11 12],2))
xlabel('frequency')
ylabel('PSD')
title('Solenoid2')

figure(4)
subplot(2,1,1); semilogy(W,PSD(:,[13 14 15 16],1))
xlabel('frequency')
ylabel('PSD')
title('Power Spectral Density for 19.71-21.69[mph]-Solenoid1')
legend('19.71','20.37','21.03','21.69')
subplot(2,1,2); semilogy(W,PSD(:,[13 14 15 16],2))
xlabel('frequency')
ylabel('PSD')
title('Solenoid2')

figure(5)
subplot(2,1,1); semilogy(W,PSD(:,[17 18 19 20],1))
xlabel('frequency')
ylabel('PSD')
title('Power Spectral Density for 22.35-24.34[mph]-Solenoid1')
legend('22.35','23.02','23.68','24.34')
subplot(2,1,2); semilogy(W,PSD(:,[17 18 19 20],2))
xlabel('frequency')
ylabel('PSD')
title('Solenoid2')

figure(6)
subplot(2,1,1); semilogy(W,PSD(:,[21 22 23 24],1))
xlabel('frequency')
ylabel('PSD')
title('Power Spectral Density for 25.00-26.99[mph]-Solenoid1')
legend('25.00','25.66','26.33','26.99')
subplot(2,1,2); semilogy(W,PSD(:,[21 22 23 24],2))
xlabel('frequency')
ylabel('PSD')
title('Solenoid2')

figure(7)
subplot(2,1,1); semilogy(W,PSD(:,[25 26 27 28],1))
xlabel('frequency')
ylabel('PSD')
title('Power Spectral Density for 27.65-29.63[mph]-Solenoid1')
```

```
legend('27.65','28.31','28.97','29.63')
subplot(2,1,2); semilogy(W,PSD(:,[25 26 27 28],2))
xlabel('frequency')
ylabel('PSD')
title('Solenoid2')

figure(8)
subplot(2,1,1); semilogy(W,PSD(:,[29 30 31 32],1))
xlabel('frequency')
ylabel('PSD')
title('Power Spectral Density for 30.30-32.28[mph]-Solenoid1')
legend('30.30','30.96','31.62','32.28')
subplot(2,1,2); semilogy(W,PSD(:,[29 30 31 32],2))
xlabel('frequency')
ylabel('PSD')
title('Solenoid2')

figure(9)
subplot(2,1,1); semilogy(W,PSD(:,[33 34 35 36],1))
xlabel('frequency')
ylabel('PSD')
title('Power Spectral Density for 32.94-34.93[mph]-Solenoid1')
legend('32.94','33.60','34.27','34.93')
subplot(2,1,2); semilogy(W,PSD(:,[33 34 35 36],2))
xlabel('frequency')
ylabel('PSD')
title('Solenoid2')

figure(10)
subplot(2,1,1); semilogy(W,PSD(:,[37 38 39 40 41],1))
xlabel('frequency')
ylabel('PSD')
title('Power Spectral Density for 35.59-38.24[mph]-Solenoid1')
legend('35.59','36.25','36.91','37.57','38.24')
subplot(2,1,2); semilogy(W,PSD(:,[37 38 39 40 41],2))
xlabel('frequency')
ylabel('PSD')
title('Solenoid2')

%%%%%%%%%%%%%%%%%%%%%%%%%%%%%%%%%%%%%%%%%%%%%%%%%%%%%%%%%%%%%%%%%%%%%%%%%%%%%%%
%%%%%%%%%%%%%%%%%%%%%%%%%%%%%%%%%%%%%%%%%%%%%%%%%%%%%%%%%%%%%%%%%%%%%%%%%%%%%%%

%Timothy Bagatti
%MiniHornet Experiments
%Data Acquisition for PowerSpectralDensity for Bluff Bodies

%MUST use following command to figure out how daq ID is declared before
%starting: daqhwinfo('nidaq')

clear all
close all

%PREAMBLE - setting sample size and rate
date = [num2str(05192010) '_BluffBody_trial1']; %saving date plus day
%run number
time_T = 30; %setting total run time to 30 sec
fs = 1000;%[hz] Sample Rate
fN = fs/2; % Setting Nyquist frequency
N = fs*time_T; %Total number of samples... setting to save 30sec worth
delta_t = 1/fs; %setting delta t
velnum = 41; %setting number of velocities
bluffnum = 3; %setting number of tested bluff bodies

%PRELIM - opening and setting data acquisiton card and channels
ai = analoginput('nidaq','dev4'); %setting up to acquire data in
%variable "ai"
ch = addchannel(ai,(0:1)); %setting to acquire data in channels 0
%to variable "Volts"
```

```
%PRETRIGGER - setting sample resolution and triggering
set(ai,'SampleRate',fs);   %setting sample rate to 1000Hz
set(ai,'SamplesPerTrigger',N);   %setting sample length to 30s
%set(ai,'InputRange',[-5 5]); %setting input range to 5 volt spread
ai.Channel(1).InputRange = [-10 10]; %setting input range to 10 volt
%spread
set(ai,'triggerChannel',ch(1)); %setting trigger to channel 1
set(ai,'TriggerType','Software'); %required when specify following
%conditions
set(ai,'TriggerCondition','Rising'); %setting rising trigger slope type
set(ai,'TriggerConditionValue',0); %setting trigger voltage level

%Allocating space
velval = zeros(velnum,1);
bluffdia = zeros(bluffnum,1);
PSDbluff.channel1 = zeros(2049,velnum,bluffnum);
PSDbluff.channel2 = zeros(2049,velnum,bluffnum);
Pxx1 = zeros(velnum);
Pxx2 = zeros(velnum);
Volts = zeros(N,2,bluffnum);

%Start loop of data acquisition
for B = 1:bluffnum; %outer bluff number loop

bluffdia(B) = input('Please input bluff diameter[in] without a decimal:');

    for V = 1:velnum; %inner velocity loop

    %Input velocity as related to wind tunnel fan RPM
    velval(V) = input('Please input velocity value[Hz]: ');

    %BEGIN TRIGGER - acquiring data
    start(ai);
    Volts(:,:,B) = getdata(ai); %saving to matrix "Volts"

    %Saving the run data
    eval(['save bluffdia' num2str(bluffdia(B)) 'Vel' num2str(velval(V))...
        '_' date ' Volts']); %saving Volts

    %Manipulate data
    %Channel1_BottomLeftSolenoid
    [Pxx1,W] = pwelch(Volts(:,1,B),boxcar(3750),[],[],fs);
    PSDbluff.channel1(:,V,B) = Pxx1;
    %Channel2_BottomRightSolenoid
    [Pxx2,W] = pwelch(Volts(:,2,B),boxcar(3750),[],[],fs);
    PSDbluff.channel2(:,V,B) = Pxx2;
    end
end

%Saving bluff power matrix
eval(['save pwelch_' date ' PSDbluff.channel1 velval']);
eval(['save pwelch_' date ' PSDbluff.channel2 velval']);

%loading bluff power matrix if the need arises
eval(['load pwelch_5192010_BluffBody_trial1' ' PSDbluff.channel1 velval']);
eval(['load pwelch_5192010_BluffBody_trial1' ' PSDbluff.channel2 velval']);

%Loading no bluff power matrix
eval(['load pwelch_4282010_Solenoid_trial1' ' PSD velval']);

%velocity in mph (only used for plotting)
velval = [11.77 12.43 13.09 13.75 14.41 15.08 15.74 16.40 17.06 17.72...
    18.38 19.05 19.71 20.37 21.03 21.69 22.35 23.02 23.68 24.34 25.00...
    25.66 26.33 26.99 27.65 28.31 28.97 29.63 30.30 30.96 31.62 32.28...
    32.94 33.60 34.27 34.93 35.59 36.25 36.91 37.57 38.24];

%plotting
```

```
%plots no bluff body run against each bluff runs
%%% for bluff body (channel1)
for Bp = 1:bluffnum;

%% surface and waterfall plots
[Vmx,Fmx] = meshgrid(velval,W);
PSD_dB = 10*log10(PSD(:,:,1));
PSDbluff_dB = 10*log10(PSDbluff(:,:,2));

%my analysis for strouhal max bluff body analysis
format long
Vval = linspace(11.76784,38.23568);
fval = linspace(0,150);
mph2mps = 0.44704;
Vval_mps = mph2mps.*Vval;
L = 0.1524; %m characteristic flow length
mu = 15.11*10^(-6);
Re_mps = (Vval_mps.*L./mu);
S_Re = 0.2684-1.035./sqrt(Re_mps);
inch2mile = 1.57828283*10^(-5);
inch2meter =  0.0254;
D_in = bluffdia(Bp); %diameter in inches
D_m = D_in*inch2meter;
VV = (D_m*fval)./S_Re;
mps2mph =  2.236936;
VVmph = VV*mps2mph;

figure()
%no bluff
subplot(1,2,1); waterfall(Fmx,Vmx,PSD_dB)
%hold on
%plot(fval,VVmph)
%hold off
xlabel('frequency (Hz)')
ylabel('velocity (mph)')
view(2)
%bluff
subplot(1,2,2); waterfall(Fmx,Vmx,PSDbluff_dB)
%hold on
%plot(fval,VVmph)
%hold off
xlabel('frequency (Hz)')
ylabel('velocity (mph)')
view(2)
title('Waterfall subplots of PSD without(left) versus with(right)'...
'a bluff body')
end

%%semilog plots to show peak amplitude increase
%for both measured channels
%D = 1.4633in f = 50Hz
figure(4)
subplot(2,1,1); semilogy(W,PSD(:,7,1),W,PSDbluff.channel1(:,7,1))
xlabel('frequency')
ylabel('PSD')
title('Power Spectral Density for 15.74[mph]-Solenoid1')
legend('no bluff','bluff')
subplot(2,1,2); semilogy(W,PSD(:,7,2),W,PSDbluff.channel2(:,7,1))
xlabel('frequency')
ylabel('PSD')
title('Solenoid2')

%D = 1.65795in f = 46Hz
figure(5)
subplot(2,1,1); semilogy(W,PSD(:,8,1),W,PSDbluff.channel1(:,8,2))
xlabel('frequency')
ylabel('PSD')
title('Power Spectral Density for 16.40[mph]-Solenoid1')
```

```
legend('no bluff','bluff')
subplot(2,1,2); semilogy(W,PSD(:,8,2),W,PSDbluff.channel2(:,8,2))
xlabel('frequency')
ylabel('PSD')
title('Solenoid2')

%D = 1.4633in f = 56Hz
figure(6)
subplot(2,1,1); semilogy(W,PSD(:,10,1),W,PSDbluff.channel1(:,10,3))
xlabel('frequency')
ylabel('PSD')
title('Power Spectral Density for 17.72[mph]-Solenoid1')
legend('no bluff','bluff')
subplot(2,1,2); semilogy(W,PSD(:,10,2),W,PSDbluff.channel2(:,10,3))
xlabel('frequency')
ylabel('PSD')
title('Solenoid2')

%CLEAN UP - clean up
delete(ai);
clear ai;

%%%%%%%%%%%%%%%%%%%%%%%%%%%%%%%%%%%%%%%%%%%%%%%%%%%%%%%%%%%%%%%%%%%%%%%%%%%%%%%
```

BIBLIOGRAPHY

[1] Piezoelectric effect. http://webdocs.cs.ualberta.ca/~database/MEMS/sma_mems/img/piezoeffect.jpg.

[2] Piezoelectric effect. http://wpcontent.answers.com/wikipedia/commons/c/c4/SchemaPiezo.gif.

[3] Proof of betz' law. Danish Wind Industry Association. http://www.talentfactory.dk/en/stat/betzpro.htm.

[4] von Kármán vortex street. http://www.simerics.com/animation/karman_vortex_street_experiment.gif.

[5] von Kármán vortex street. http://hmf.enseeiht.fr/travaux/CD0102/travaux/optmfn/gpfmho/01-02/grp1/images/guadal.gif.

[6] Darrieus wind turbine. How Wind Power Works: Vertical-axis Turbine, http://static.howstuffworks.com/gif/wind-power-vertical.gif 2006.

[7] 20% wind energy by 2030: Increasing wind energy's contribution to u.s. electricity supply. U.S. Department of Energy, July 2008.

[8] Top five micro wind turbines. http://cleantechnica.com/2008/03/21/the-five-best-micro-wind-turbines/, March 2008.

[9] 6" open circuit windtunnel: Installation, operation, and maintenance instructions. Engineering Laboratory Design Inc., March 2009.

[10] Annual energy outlook 2009 with projections to 2030. Energy Information Administration/U.S. Department of Energy, 2009.

[11] Annual energy outlook early release overview. Department of Energy/U.S. Energy Information Administration, 2009. www.eia.doe.gov/oiaf/aeo/overview.html.

[12] Electric power monthly. Energy Information Administration. http://www.eia.doe.gov/, April 2009.

[13] International energy outlook. Energy Information Administration/U.S. Department of Energy, 2009.

[14] Savonius wind turbine. http://www.poespoes.nl/log/savonius-wind-turbine2.jpg, 2009.

[15] Wind energy – the facts: Executive summary. European Wind Energy Association, 2009.

[16] Windpower outlook 2009. American Wind Energy Association, 2009.

[17] Humdinger windbelt family tree. Humdinger Wind Energy, LLC. http://www.humdingerwind.com, February 2010.

[18] Oregon state university conceptual wave park. http://greenpoweroregon.com/Images/wave_large.jpg, March 2010.

[19] Rotary electric generator. http://www.daviddarling.info/images/electric_motor.jpg, Febuary 2010.

[20] Rotary to linear induction device. http://www.force.co.uk/images/SDEV.jpg, Febuary 2010.

[21] Tacoma Narrows Bridge. http://www.mae.cornell.edu/images/etc/fluids/structure/tacoma.gif, March 2010.

[22] Tacoma Narrows Bridge failure. http://blogofbad.files.wordpress.com/2008/09/tacoma.jpg, March 2010.

[23] Willis Owuor Agutu. Characterization of electromagnetic induction damper. Master's thesis, Miami University, 2007.

[24] Western Governors' Association. Clean energy, a strong economy and a healthy environment. Clean and Diversified Energy Advisory Committee, 2006.

[25] S. P. Beeby, M. j. Tudor, and N. M. White. Energy harvesting vibration sources for microsystems applications. *Measurement Science and Technology*, 17:R175–R195, 2006.

[26] I. Boldea and S.A. Nasar. Linear electric actuators and generators. Technical report, University of Politehnica and University of Kentucky, 1997.

[27] Jurgen Brunahl. *Physics of Piezoelectric Shear Mode Inkjet Actuators*. PhD thesis, Royal Institute of Technology, Stockholm, 2003.

[28] Matthew Bryant and Ephrahim Garcia. Development of an aeroelastic vibration power harvester. Technical report, Sibley School of Mechanical and Aerospace Engineering, Cornell University Laboratory for Intelligent Machine Systems, 2009.

[29] Vinod R. Challa, M.G. Prasad, Yong Shi, and Frank T. Fisher. A vibration energy harvesting device with bidirectional resonance frequency tunability. *Smart Materials and Structures*, 17:1–10, 2008.

[30] Steven C. Chapra and Raymond P. Canale. *Numerical Methods for Engineers*. McGraw-Hill Companies, Inc., 2010.

[31] William W. Clark and Michael J. Ramsay. Smart Material Transducers as Power Sources for MEMS Devices. Technical report, Mechanical Engineering Department, University of Pittsburgh, 2000.

[32] D. Clubb. Domestic roof-mounted wind turbines: The current state of art. Mid Wales Energy Agency.

[33] Daniel G. Cole and Lisa M. Weiland. An analysis of micro aeroelastic energy harvesting devices. ASME 2009 Dynamic Systems and Control Conference, October 2009.

[34] Earl H. Dowell, Robert Clark, David Cox, Jr. H.C. Curtiss, John W. Edwards, Kenneth C. Hall, David A. Peters, Robert Scanlan, Emil Simiu, Fernando Sisto, and Thomas W. Strganac. *A Modern Course in Aeroelasticity*, volume 116. Kluwer Academic Publishers, fourth edition, 2004.

[35] A.G. Drachmann. Heron's windmill. *Centauras*, 7:145–151, 1961.

[36] Uwe Fey, Michael Konig, and Helmut Eckelmann. A new strouhal-reynolds-number relationship for the circular cylinder in the range $47 < re < 2 \times 10^5$. *Physics Fluids*, 10:1547–1549, 1998.

[37] A. Gelb and W.E. Vander. *Multiple-input Describing Functions And Nonlinear System Design*. McGraw-Hill, 1968.

[38] Allan R. Hambley. *Electrical Engineering: Principles and Applications*. Pearson Education, Inc., 2005.

[39] Dewey H. Hodges and G. Alvin Pierce. *Introduction to Structural Dynamics and Aeroelasticity*. Cambridge University Press, 2002.

[40] John Houghton. Global warming is now a weapon of mass destruction. Guardian News and Media Limited, 2003.

[41] John T. Houghton. *Global Warming: The Complete Briefing*. Cambridge University Press, fourth edition, 2009.

[42] Hongping Hu, Chun Zhao, Shengyuan Feng, Yuantai Hu, and Chuanyao Chen. Adjusting the resonant frequency of a pvdf bimorph power harvester through a corrugation-shaped harvesting structure. *IEEE Transactions on Ultrasonics, Ferroelectrics, and Frequency Control*, 55:668–674, 2008.

[43] Encyclopedia Britannica Inc. Rotary generator. http://www.library.yale.edu/NotaBene/nbx3/motor.htm, 1994.

[44] Tom Irvine. An introduction to frequency response functions. http://www.engineering.wright.edu/~jslater/SDTCOutreachWebsite/intro_freq_resp_functions.pdf.

[45] What is Energy and How it Works. Rotary generator power plant. http://www.bizaims.com/coffeebreak/curiositieseventsfunny/whatenergyandhowitworks, Febuary 2010.

[46] Shunong Jiang, Xianfang Li, Shaohua Gua, Yuantai Hu, Jiashi Yang, and Qing Jiang. Performance of a piezoelectric bimorph for scavenging vibration energy. *Smart Materials and Structures*, 14:769–774, 2005.

[47] Junwu Kan, Kehong Tang, Hongwei Zhao, Chenghui Shao, and Guoren Zhu. Perfomance analysis of piezoelectric bimorph generator. *Frontiers of Mechanical Engineering in China*, 3:151–157, 2008.

[48] Shuguang Li and Dr. Hod Lipson. Vertical-stalk flapping-leaf generator for wind energy harvesting. Technical report, Sibley School of Mechanical and Aerospace Engineering, Cornell University, 2009.

[49] J.F. Manwell, J.G. McGowan, and A.L. Rogers. *Wind Energy Explained: Theory, Design, and Application*. John Wiley & Sons, Ltd., second edition, 2009.

[50] F. Inst. P. Thomas Martin M.Sc. *Faraday's Discovery of Electro-magnetic Induction*. Butler & Tanner Ltd., Frome and London, 1949.

[51] Y. Nakamua. Vortex shedding from bluff bodies and a universal strouhal number. *Journal of Fluids and Structure*, 10:159–171, 1996.

[52] Oxford Dictionary of National Biography. James Blyth. Oxford University Press, 2009.

[53] Hiroshi Okamoto, Takafumi Suzuki, Kazuhiro Mori, Ziping Cao, Teppei Onuki, and Hiroki Kuwano. The advantages and potential of electret-based vibration-driven micro energy harvesters. *International Journal of Energy Research*, 33:1180–1190, 2009.

[54] Sebastian Pobering and Norbert Schwesinger. A novel hydropower harvesting device. Technical report, Munich University of Technology, 2004.

[55] S. Roundy and P. K. Wright. A piezoelectric vibration based generator for wireless electronics. *Smart Materials and Structures*, 13:1131–1142, 2004.

[56] J. W. Sohn, S B. Choi, and D Y Lee. An investigation on piezoelectric energy harvesting for mems power sources. Technical report, Department of Mechanical Engineering, Inha University, Incheon, Korea, 2005.

[57] George W. Taylor, Joseph R. Burns, Sean M. Kammann, William B. Powers, and Thomas R. Welsh. The energy harvesting eel: A small subsurface ocean/river power generator. *IEEE Journal of Oceanic Engineering*, 26:539 – 547, 2001.

[58] M. Vidyasagar. *Nonlinear Systems Analysis*. Prentice-Hall, Inc., 1978.

[59] Thomas von Buren and Gerhard Troster. Design and optimization of a linear vibration-driven electromagnetic micro-power generator. Technical report, Lectronics Lab, Department of Information Technology and Electrical Engineering, Swiss Federal Institute of Technology, Gloriastrasse 35, CH-8092 Zurich, Switzerland, August 2006.

[60] Alan Wyatt. Electric power: Challenges and choices. Book Press Ltd., Toronto, 1986. ISBN 0-920650-00-7.

[61] Q. Zhang, N. Popplewell, and A. H. Shah. Galloping of bundle condutor. *Journal of Sound and Vibration*, 234:115–134, 2000.